2013

Strongly correlated ultra-cold bosonic atoms in optical lattices

Kalani Hettiarachchilage

Louisiana State University and Agricultural and Mechanical College, khetti1@lsu.edu

STRONGLY CORRELATED ULTRA-COLD BOSONIC ATOMS
IN OPTICAL LATTICES

A Dissertation

Submitted to the Graduate Faculty of the
Louisiana State University and
Agricultural and Mechanical College
in partial fulfillment of the
requirements for the degree of
Doctor of Philosophy

in

The Department of Physics and Astronomy

by
Kalani Hettiarachchilage
B.Sc., University of Peradeniya, 2002
M.Sc., Norwegian University of Science and Technology, 2008
August 2013

To my parents for their unwavering support and encouragement.

To my husband and children who have always stood by me.

Acknowledgments

Throughout the last couple of years I have received valuable support from many. Without their support it would not have been possible to complete my program. I would like to thank the Department of Physics and Astronomy of Louisiana State University (LSU) for offering me the opportunity to pursue my PhD. I also want to thank my graduate instructors for their dedication to their classes and for widening my knowledge of physics. I am indebted to my research advisor, Dr. Juana Moreno, for her mentorship. Not only did she offer me guidance during my project, but she also constantly encouraged me to take my studies to the next level and made me understand the importance of my work. Her unwavering patience allowed me to fully understand the material that I had to learn and use. I am also grateful to Dr. Mark Jarrell for his valuable advice and assistance. It has been a pleasure to work with and learn from such an extraordinary person. I also want to thank Dr. Daniel Sheehy and Dr. Dana Browne for fruitful discussions on my research projects. I also want to thank my graduate adversary committee, Dr. Juana Moreno, Dr. Mark Jarrell, Dr. Daniel Sheehy, Dr. David Young, and Dr. Darrell Henry, for devoting some of their precious time to serve on my committee.

I am indebted to all my collaborators with whom I have worked on different projects. Among them, my special thanks to Dr. Valéry Rousseau for his valuable support and guidance on my research and for broadening my perspectives from a scientific point of view. I also want to thank Dr. Ka-Ming Tam and Dr. Dimitrios Galanakis for their valuable support and discussions. Their willingness to help me all the time and to provide me with very useful suggestions was gratefully appreciated.

I would like to thank all current members of our group for the congenial environment that we have collectively established. Special thanks to Chinedu Ekuma, Chen Kuang Shing,

Table of Contents

Abstract

A major focus in condensed matter physics is to study the origin of exotic quantum phases such as coexistent and inhomogeneous phases, quantum criticality, and secondary ordered phases close to quantum critical points. Exotic phenomena in strongly correlated systems occur due to competing complex interactions of spin, charge, lattice, and orbital degrees of freedom. Complex quantum phases in strongly correlated systems are challenging, but they might be very useful due to their possible functionality to make advance devices. In order to understand, utilize, and optimize such behaviors, we need to improve our understanding of these systems. Studies in cold atom systems are of interest since cold atom experiments provide a control on model parameters.

In this thesis, we use novel analytical and computational techniques to treat strongly interacting bosonic systems. Taking advantage of the very versatile quantum Monte Carlo Stochastic Green Function algorithm, we studied several interesting problems. First, we explore a recently developed new confining method for cold atoms on optical lattices. Atoms are confined via a hopping integral that decreases as a function of the distance from the center of the lattice. This method might lead to lower temperatures than existing diagonal confinement methods. Next, we study the ground state phase diagram of interacting bosons on a ring-shape lattice with a region of weak hopping integrals. The model, an extension of the well known Bose-Hubbard model, develops a novel local Mott phase in addition to the usual Mott and superfluid phases in the homogeneous system. This might provide a new insight to the description of atomtronics applications. Finally, we study the two species Bose Hubbard model in a two-dimensional lattice. This model presents novel phases due to the complexity associated with multiple species. Its phase diagram shows ordered and coexistence phases including a ferromagnetic phase separated phase with high entropy. This

phase might be accessible experimentally. The novel phases found from our studies are linked to experiments on ultra-cold atoms trapped by laser beams.

Chapter 1
Introduction

Strongly correlated systems are one of the most intensively studied areas of research in condensed matter physics [1–13]. This field of study has generated a lot of interest among researchers over the last few decades. In recent years a wide variety of experimental observations and theoretical predictions have found that many phase transitions in real materials show complex interesting states that are nontrivial [1–13]. Well known examples of this behavior are the colossal magneto-resistive materials, that display changes in their resistivity by orders of magnitude with the application of small magnetic fields; the heavy fermions with huge effective electronic masses; the magnetic semiconductors with the possibility of manipulating both the spin and the charge degrees of freedom; and the high temperature superconductors that conduct electricity without any resistance above the temperature of liquid nitrogen [8–13]. Competing interactions of spin, charge, lattice, and orbital character in these systems lead to the presence of many complex phases [1–7]. Collective states of these complex systems are hard to understand by using a quantum mechanical quasi-particle approximation. We need to consider strong correlations between particles to understand the properties of such materials. However understanding, controlling and predicting the competing complexity of strongly correlated systems are the most challenging fields in condensed matter physics. Since competing phases can be tuned via external parameters, the rich phase diagrams of correlated materials make them natural candidates for devices where their non-linear responses can be exploited. The fundamental parameters for controlling the behavior of correlated systems are the amplitude of particle hopping between sites, the on-site particle-particle Coulomb repulsion and the density of charge carriers or the filling factor.

Since cold atom experiments provide a control on these model parameters, studies in cold atomic systems are also extremely relevant for material physicists. Further, the possibility to perform exact computational studies by using quantum Monte Carlo (QMC) simulations encourages physicists to play on cold atomic systems theoretically, as a way to understand more complex phenomena. Since computationally exact QMC studies of fermionic systems are limited by the so-called "sign problem," [14–16], studies of bosonic systems, which can often be described by sign-problem-free Hamiltonians are of interest. Close interaction between theory and experiment has been crucial to progress in the field. A remarkable achievement is the realization of the Bose-Hubbard model using ultra cold atoms on optical lattices [17,18]. Tuning between insulating and conducting phases by controlling the external parameters provides a tantalizing opportunity of creating analogs to electronic devices [19–21]. Based on this unique property, it has been suggested that these systems may be useful in quantum computing in the near future.

This chapter provides a brief history and introduction to the field of ultra-cold atoms on optical lattices including the revision of some fundamental aspects: Bose-Einstein condensation, optical lattices, atomic applications and the details of the well-known Bose Hubbard (BH) Hamiltonian and its phase diagram. The introduction chapter will be finished by the structure of the thesis.

1.1 Historical Perspective of Cold Atoms

Atomic physics and quantum optics have a very long history. Although there was valuable progress in theoretical studies of atomic physics and experimental studies of quantum optics, revolutionary contributions occurred with the development of laser physics by 1981 Nobel prize winners A. L. Schawlow and N. Bloembergen with their "development of laser spectroscopy" [22,23]. Enormous progress on studies of single particle quantum systems was due to 'the development of the iron trap technique" by H. G. Dehmelt and W. Paul and "the invention of the separated oscillatory field method and application to atomic clocks" by N.

F. Ramsey. All of them shared the Nobel prize in 1989 [22,23]. Studies on quantum coherent theory by R. J Glauber (Noble prize winner in 2005) and the development of laser theory by M. Scully, W. E Lamb (Noble laureate in 1955) and H. Haken allow the culmination of the theoretical quantum optics [22, 24–27]. Later there were many discoveries that have developed both atomic physics and quantum optics. The Nobel prize for S. Chu [28], C. Cohen-Tannoudji [29] and W. D. Phillips [30] for "the development of laser light to cool and trap atoms" [22] in 1997 recognized their success to confine atoms at very low temperatures. Atomic cooling and trapping techniques have reached the nano-Kelvin regime of temperature with the unbelievable progress in the field of quantum engineering. Experimental studies of Bose Einstein condensation (BEC) in bosonic gases by using laser cooling combined with evaporative cooling in 1995 were recognized with the 2001 Nobel prize to E. A. Cornell, C. E. Wieman and W. Ketterle for "the achievement of Bose-Einstein condensation in alkali atoms and the early fundamental studies of the condensate" [22]. Although BEC was predicted by Einstein in 1925 [31] based on the idea of quantum statistics by Bose in 1924 [32], this was a remarkable achievement for atomic, quantum optics, nuclear, high energy and condensed matter physics.

Physics in strongly correlated ultra cold atomic systems started with the prediction of superfluid to Mott insulator transition in optical lattices by Jaksch et al. [17] in 1998. This was motivated by the realization of quantum computing with ultra cold atoms trapped in optical lattices. Experimental studies of the superfluid to Mott insulator transition entered the area of strongly correlated cold atoms with the paper by M. Greiner et al. [18] in 2002. Thereafter, the study of trapped atomic gases has dramatically increased. These include theoretical studies of disordered Bose systems [33–37], Bose-Fermi mixtures [38–41] and Bose-Bose mixtures [42–44]. Moreover, the experimental study of the $^{84}Rb-^{41}K, ^{6}Li-^{40}K$ and different alkaline earth mixtures in an optical lattice have been studied recently [45–47]. This is also an exciting time for advance device applications since model parameters can be tuned using laser and magnetic fields [48, 49].
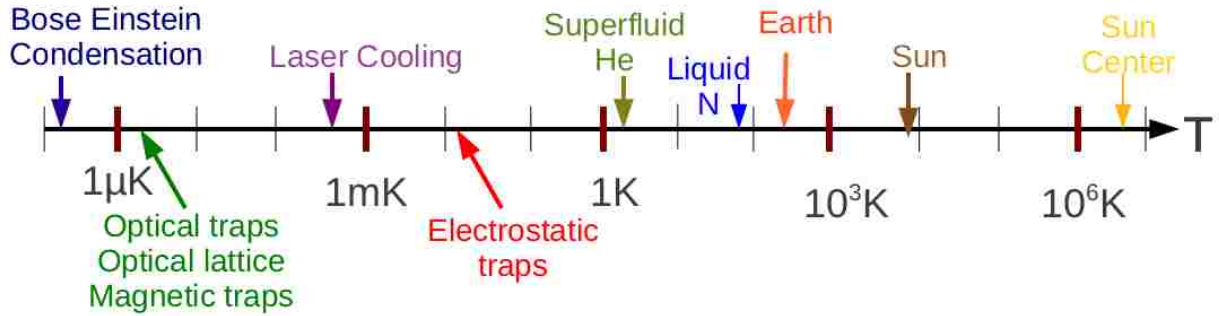
Figure 1.1: Important discoveries at low temperatures are shown in logarithmic temperature scale. The temperatures of Superfluidity of He, laser cooling and Bose Einstein Condensation (BEC) are shown.

1.2 Cold Atoms in Condensed Matter Physics

On the surface of the sun we miss many aspects of nature [50]. On the surface of the earth particles can have different states of matter such as solid, liquid and gas [50]. Can we observe other different states of matter by lowering the temperature? How do we go to such low temperatures? In the Kelvins range, superconductivity was discovered in 1911 [51] and superfluidity in liquid Helium (^4He) was discovered in 1938 [52]. With the advent of laser cooling and the evaporative cooling in the 1980s, particles can be cooled to nano-Kelvin temperatures. Important findings at low temperatures are shown in logarithmic temperature scale in Fig. 1.1 . Laser cooling and evaporative cooling in a magnetic trap developed in the 1980s open up new approaches to ultra cold physics. Those allow atoms to be cooled to ultra cold temperature in nano-Kelvin range and ultra low density (see Fig. 1.2). Many of the past century experiments try to cool particles close to absolute zero, where new physics emerges and interesting phase transitions appear due to the quantum fluctuation driven by the Heisenberg uncertainty principle [50,53]. Atoms maintained close to absolute zero are called ultra-cold atoms. Ultra-cold atoms are in the regime of quantum degeneracy where the thermal de Broglie wavelength of an atom $\lambda = \hbar/(2Mk_BT)^{1/2}$ and its inter-atomic distance become comparable. In this regime the wave packet of neighboring atoms overlap

4
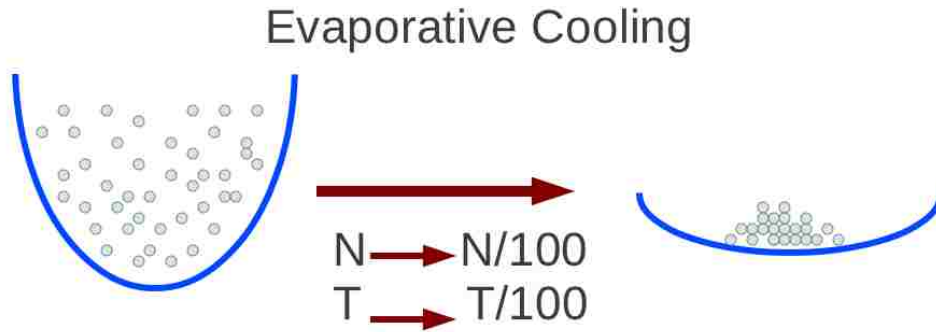
Figure 1.2: Evaporative cooling. This allows atoms to be in ultra-low temperature and ultra-low density by evaporating high energetic particles.

and form a quantum gas, a cloud of indistinguishable particles [50,53]. If those particles are fermions, half integer spin particles, they obey the Pauli exclusion principle and the lowest energy state of the system is a Fermi liquid (see Fig. 1.3). If particles are bosons, integer spin particles, they obey Bose Einstein statistics and condensate into the lowest energy wavefunction (see Fig. 1.3). This is called Bose Einstein condensation (BEC). This new state of matter was first predicted by Nath Bose and Albert Einstein in 1924 for photons or a packet of light. This phenomenon on dilute gases was first realized experimentally for Rubidium [54], Sodium [55] and Lithium [56] in 1995. Evidence for super-fluidity, the flow of a liquid without dissipation and with infinite thermal conductivity was first observed for liquid Helium in 1938 [52]. After a long controversy on the connection between Bose Einstein condensation (BEC) and superfluidity, most physicists accepted the quasi classical model of London and Tisza [52,57–59], although the relevance of these two phenomena was still unclear due to the lack of a microscopic theory of liquid ^4He.

After the experimental realization of BEC in 1995, the number of studies on trapped atomic gases has dramatically increased. Among those investigations, cold atoms in optical latices have recently been developed and used to observe many strongly correlated properties, such as superfluid to Mott insulator transition. In 1998, Anderson and Kasevich performed
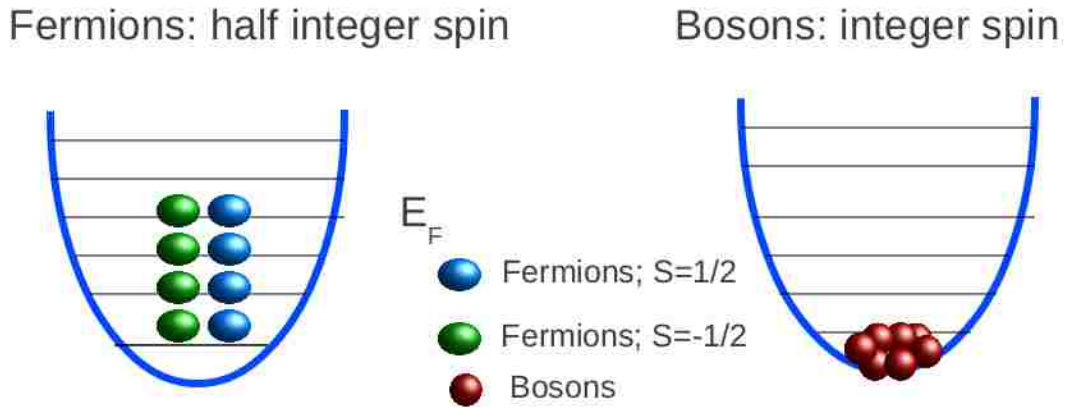
Figure 1.3: Fermi Dirac statistics and Bose Einstein statistics of indistinguishable particles. Blue solid circles are fermions with $S = 1/2$, green solid circles are fermions with $S = -1/2$ and red solid circles are bosons.

the first experiment of BEC in an optical lattice [60]. Now, systems of ultra-cold atoms in optical lattice potentials are at the frontiers of modern physics.

1.3 Bose Einstein Condensation

A Bose Einstein condensate (BEC) is an unusual state of matter (see Fig. 1.3). This behavior appears due to the quantum mechanical nature of bosons. This phenomenon only can occurs at very low temperatures, when all the bosons condensate into their lowest energy state and they act as a unique wavefunction. Although the original prediction of BEC was for non-interacting bosons, the finding of superfluidity in ^4He suggested to extend this concept beyond non-interacting systems. Friz London proposed the existence of a link between superfluidity in ^4He and the BEC despite the strong interactions in ^4He. London's approach to superfluidity is considered as the starting point of current theories. Landau explained this phenomenon as a mixture of two components, a normal fluid and a superfluid [61]; this was called the two fluid model. Landau thought that properties of the normal component were related to elementary excitations of the superfluid component, such as phonons and rotons in

^4He. In addition to superfluidity, superconductivity can be considered as a BEC of Cooper pairs: electrons combine in pairs that behave as composite bosons, and can condense in the same state.

Theoretical studies of BEC in strongly interacting systems are very difficult. But weakly interacting gases and their BEC are described by the Gross-Pitaevskii equation and the Bogoliubov theory [62–65]. An ideal gas of bosons obeys Bose-Einstein statistics. The mean occupation number of atoms in quantum state i with energy ε_i in equilibrium with a chemical potential μ, an inverse temperature $\beta = \dfrac{1}{k_B T}$ and Boltzmann's constant k_B is given by

$$n_i = \frac{1}{e^{\beta(\varepsilon_i - \mu)} - 1}. \tag{1.1}$$

The formation and stabilization of BECs entirely depend on this property of Bose statistics.

In the case of a non-interacting Bose gas at zero temperature, the cloud fully condenses and all particles can be described by a single particle wave function. Thus, the many body wave function with N number of particles can be given by the product over identical single wave functions, $\phi(r)$, as

$$\psi(r_1, r_2, ..., r_N) = \prod_{i=1}^{N} \phi(r_i). \tag{1.2}$$

The nature of the BEC state can be described by the wave function of the condensate or the order parameter $\psi\prime(r)$ [66]. This $\psi\prime(r)$ is the normalized Schrödinger wave function when the condensation occurs. The number of particles is $N = \int dr |\psi\prime(r)|^2$. In the case of non-interacting bosons the single particle state is simply the single particle ground state of the trapping potential. Well known examples are a Bloch wave and a Gaussian wave when the trapping potential is periodic and harmonic respectively.

When interactions are present, we have to determine the condensate wave function. Condensate atoms can interact via elastic binary collisions which need to be treated using scattering theory. However, real inter-particle scattering potential is very complicated and we rely on some approximations for treating them. In the case of extremely cold dilute gases, the rel-

evant collisions are only head on and thus the scattering is s-wave. Therefore, the interaction can be modeled by a zero-range potential with the strength given by the s-wave scattering length [67]. Since each atom is influenced by the extra potential due to the mean field of all the other atoms, the many body Schrödinger equation including atomic interactions can be written as the nonlinear Schrödinger equation, or the Gross Pitaevskii equation [68, 69], with the boson mass m, the external potential $V(r)$ and the inter-particle interaction U_0, as

$$i\hbar\frac{\partial\psi(r)}{\partial t} = \{-\frac{\hbar^2\nabla^2}{2m} + V(r) + U_0|\psi\prime(r)|^2\}\psi(r). \tag{1.3}$$

In order to deal with strongly correlated bosons, we need to understand the condensate in the strong interaction region. Our interaction energy has to be of the same order or larger than the kinetic energy. The best known and easiest way to reach this regime is raising the scattering length [70]. This is experimentally feasible by using a Feshbach resonance, the bound state in the close channel energetically reaches the scattering state of the open channel [71, 72].

The condensate temperature of a non-interacting three-dimensional uniform gas with particle density n, particle mass m, reduced Plank constant $\hbar$ and Boltzmann constant k_B can be estimated as [65].

$$\mathcal{T}_c = 3.31\frac{\hbar^2 n^{2/3}}{mk_B}. \tag{1.4}$$

For ^4He at saturated vapor pressure, we get $\mathcal{T}_c = 3.13K$. This is close to the so called Lambda point, the superfluid transition temperature at $\mathcal{T}_c = 2.17K$ [65].

In real cold atom experiments, there is not a uniform gas because it is trapped in a harmonic potential. The density of gas is $n \approx \frac{N}{R^3}$, where $R \approx (\frac{k_B T}{m\omega_0^2})^{1/2}$ and ω_0 is the angular frequency of particle motion in the potential, and N is the particle number. From (1.4), we can write the condensate temperature as [65]

$$\mathcal{T}_c = 0.94\hbar\omega_0 N^{1/3}. \tag{1.5}$$

Although theoretical studies on uniform gases were done very early, recently new features have been found in atomic clouds in the presence of a confining potential.

1.4 Optical Lattices

Optical lattices can be created by the interference of counter-propagating laser beams forming an artificial crystal of light. This is a periodic Stark shift potential with the lattice periodicity. Atoms can be trapped in this potential by laser and evaporative cooling techniques [50]. They can move through the lattice due to the quantum tunneling through many harmonic-like potentials. Ultra-cold atoms in optical lattices behave very much like electrons in periodic crystals. Optical lattices have several advantages over solid crystals. Atoms in optical lattices are intrinsically defect free. Furthermore, optical lattices have a high degree of control by changing the properties of the laser beams. The well depth and the lattice periodicity can be controlled by adjusting the power of the beams and the relative angle between the laser, or the wavelengths of the laser beams, respectively [53, 74]. Although the lattice constant of solid crystals are of the order of a few Angstroms, the lattice constant in optical lattices are few orders of magnitude larger [73]. Experimentalists now can smoothly turn on optical lattices in one, two and three dimensions for various lattice geometries [75, 76]. After Anderson and Kasevich performed the first experiment of BECs in optical lattices [60] in 1998, both experimental and theoretical studies of the system of ultra-cold atoms in optical lattice potentials show substantial progress. The theoretical studies of the Bose Hubbard (BH) model in atomic optical lattices by Jaksch et al. [17] and the experimental studies of Mott insulator to superfluid transition of BH model by Greiner et al. [18] are the most remarkable achievements in the field of strongly correlated systems in trapped cold atomic gases.

Three pairs of counter propagating lasers with the same wavelength and intensity on perpendicular directions provide a three dimensional potential

$$V_{OP}(x,y,z) = V_0(\sin^2 kx + \sin^2 ky + \sin^2 kz), \tag{1.6}$$

where V_0 is the strength of the lattice potential or the maximum depth of the lattice potential and $k = \dfrac{2\pi}{\lambda}$ is the wave vector of the laser light.

Consider a system of interacting bosons moving in an optical lattice with a periodic potential $V_{OP}(\vec{r})$, a trapping potential $V_{TP}(\vec{r})$ and the interacting potential $V_{INT}(|\vec{r} - \vec{r'}|)$. The Hamiltonian can be written as [17]

$$\begin{aligned}
\hat{\mathcal{H}} &= \int d\vec{r}\hat{\psi}^\dagger(\vec{r})[\frac{p^2}{2m} + V_{OP}(\vec{r}) + V_{TP}]\hat{\psi}(\vec{r}) \\
&\quad + \frac{1}{2}\int d\vec{r}\int d\vec{r'}\hat{\psi}^\dagger(\vec{r})\hat{\psi}^\dagger(\vec{r'})V_{INT}(|\vec{r}-\vec{r'}|)\hat{\psi}(\vec{r'})\hat{\psi}(\vec{r}),
\end{aligned} \tag{1.7}$$

where $\hat{\psi}(\vec{r})$, $\hat{\psi}^\dagger(\vec{r})$ are field operators which satisfy the commutation rules, $[\hat{\psi}(\vec{r}),\hat{\psi}(\vec{r'})] = [\hat{\psi}^\dagger(\vec{r}),\hat{\psi}^\dagger(\vec{r'})] = 0$ and $[\hat{\psi}(\vec{r}),\hat{\psi}^\dagger(\vec{r'})] = \delta_{\vec{r},\vec{r'}}$. We can decompose the field operator $\hat{\psi}(\vec{r})$ on a Wannier basis,

$$\hat{\psi}(\vec{r}) = \sum_{n,\vec{r}_i} w_n(\vec{r} - \vec{r}_i)\hat{a}_n(\vec{r}_i), \tag{1.8}$$

where $\hat{a}_n(\vec{r}_i)(\hat{a}_n^\dagger(\vec{r}_i))$ represents the annihilation (creation) of a boson at site i and level n and $w_n(\vec{r})$ is the Wannier function of different n^{th} bands.

For a very deep lattice at very low temperatures, only the lowest band is occupied and (1.8) can be rewritten in terms of operators at lattice site i as

$$\hat{\psi}(\vec{r}) = \sum_i w(\vec{r} - \vec{r}_i)\hat{a}_i. \tag{1.9}$$

If we rewrite the Hamiltonian in (1.7) by using one band Wannier function basis, we can map this continuous model to the simplest one band BH model with chemical potential μ in

the case of grand canonical ensemble and coupling terms as

$$t = -\int d\vec{r} \, w^*(\vec{r} - \vec{r}_i)\Big[\frac{\hbar^2 \nabla_r^2}{2m} + V_{OP}(\vec{r})\Big] w(\vec{r} - \vec{r}_j), \tag{1.10}$$

$$U = \int d\vec{r} \int d\vec{r'} \, |w(\vec{r} - \vec{r}_i)|^2 V_{INT}(|\vec{r} - \vec{r'}|) |w(\vec{r'} - \vec{r}_j)|^2, \tag{1.11}$$

$$\mu = \int d\vec{r} \, V_{TP}(\vec{r}) |w(\vec{r} - \vec{r}_i)|^2. \tag{1.12}$$

By following Bloch et al. [77] and in the deep lattice limit, the single site lattice confinement is a harmonic potential. The energy of the well is $E = \hbar\omega_0 = 2E_r(V_0/E_{rec})^{1/2}$ with trapping frequency ω_0 and recoil energy $E_{rec} = \hbar^2 k^2/2m$. If we consider single particle states in an infinite three-dimensional periodic potential without any other external potentials in the limit of $V_0 \gg E_{rec}$, each well has vibrational levels separated by an energy gap $\hbar\omega_0 \gg E_{rec}$ [77]. Single particle states at very low temperature can be considered as Bloch waves because atoms are sitting at the lowest level. Now, we can write the behavior of hopping term t and the interaction term U in the limit of $V_0 \gg E_{rec}$ as

$$t \approx \frac{4}{\sqrt{\pi}} E_{rec} \Big(\frac{V_0}{E_{rec}}\Big)^{3/4} exp\Big[-2\Big(\frac{V_0}{E_{rec}}\Big)^{1/2}\Big], \tag{1.13}$$

$$U \approx \sqrt{8/\pi} ka E_{rec} \Big(\frac{V_0}{E_{rec}}\Big)^{3/4}, \tag{1.14}$$

where a is the scattering length. Besides their simplicity and the possibility of controlling their properties, optical lattices have recently become one of the most attractive fields for device applications such as quantum computation and atomtronic devices.
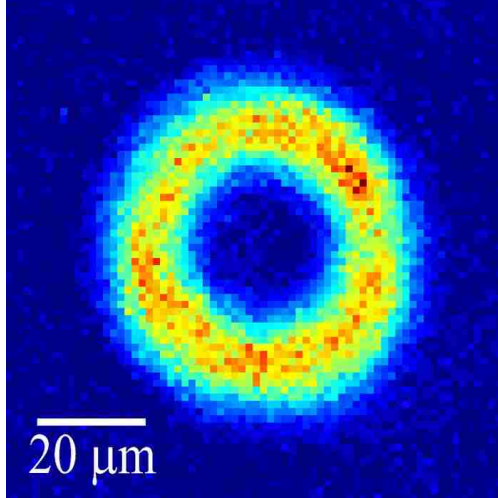
Figure 1.4: Density profile of a donut-shaped Bose Einstein Condensation (BEC). The red regions shows highest densities by creating the toroidal shape gas cloud [78]. Forty seconds persistent flow was observed.

1.5 Atomtronics

Recently developed numerical experiments suggest novel application designs for atoms trapped in optical lattices. These are the atomic analog to electronic devices, atomtronics. Experimental realization of those circuits may be an important breakthrough to future electronic applications. Similarly to the properties of superconducting electronic devices such as resistantless current and heat dissipation, atomtronic circuits can have benefits due to their coherent flow. This may be used to create circuits for quantum computing because the coherent flow of cold atoms can carry information coherently. By following References [19–21], we learn that it is possible to create circuit elements such as batteries, resistors, diodes and even transistors. According to those authors [19–21] atomic current will play the same role as electronic current. The equivalent of electric potential in an electronic circuit is chemical potential difference in atomic circuits. By changing the height of the optical lattice, atomic circuits can tune the flow of atoms through the optical waveguide. In this way it is possible to create advanced logic circuits by using ultra cold atoms. The best experimental realization of a simple atomtronic device, is the creation of a donut shape ultra-cold gas as
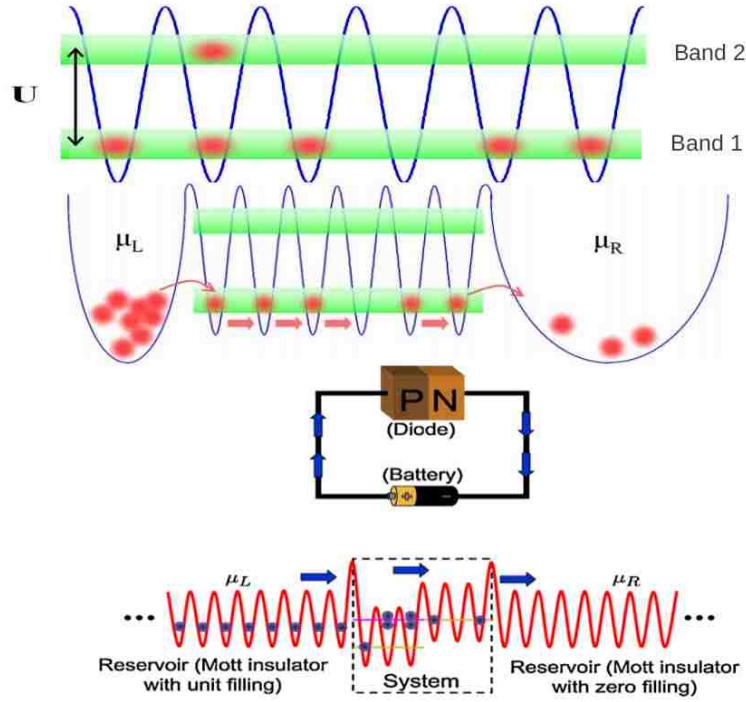
Figure 1.5: Top figure: The energy bands of strongly interacting bosons in a lattice. Band one includes all states between zero and one atomic filling per site. Band two includes all states between one and two atomic filling per site [20]. Middle figure: An atomtronic battery. A voltage is applied by connecting the system to two reservoirs with chemical potentials μ_L and μ_R. Atoms are moving from left to right due to chemical potential differences [20]. Bottom figure: Equivalent atomtronic p-n junction diode to electronic p-n junction diode with the forward bias. Atoms flow from the left to right [19].

shown in Fig. 1.4. This is the first closed loop current observed in atomic traps. The current persists up to forty seconds [78]. Numerical predictions show the behavior of atomtronic simple circuits. Those atomtronic devices can be used to build more complex circuits in the near future. Simple device applications suggested by Ref. [19–21] are shown in Fig 1.5, such as a battery and a diode. In addition to these circuit designs, Fig 1.5 also shows the band structure of strongly interacting bosons in a lattice. When the filling factor is one or two per site, the system becomes an insulator; whereas the filling factor stays in between one and two, the system is a conductor. Bands shown in green color are superfluid regions (band width) and the regions between those bands are the Mott lobes (band gaps) [19–21].

1.6 Bose Hubbard Model

In the last two decades, a considerable amount of work has been done to determine the ground state phase diagram of correlated bosons on a lattice. The simplest non-trivial model that describes interacting bosons in a periodic potential is the Bose Hubbard (BH) Hamiltonian. In this model we assume that particles occupy only the lowest Bloch band and invoke the tight-binding approximation, so that only nearest-neighbor tunneling and on-site interactions contribute to the energy. The BH model has the main physics that describes strongly interacting bosons. The Hubbard model has been used to describe many different systems in condensed matter physics, such as high temperature superconductors, Josephson junction arrays, superfluid behavior of ^4He and cold atoms in an optical lattice. Among them cold atoms in optical lattices have recently been developed and used to study new exotic phases such as Bose-glass [79], Bose liquids [80], striped solid [81], Tonks-Girardeau gas [82], super counter fluid [83] and supersolid [84]. Completing complex phases are always interesting due to their experimental realization to atomtronic applications [19–21]. The BH model has been studied analytically with many different techniques, such as mean field approximations, renormalization group theories and strong coupling expansions [37,85–89]. Numerically most studies are based on quantum Monte Carlo methods and density matrix renormalization techniques. Those theatrical studies predict a quantum phase transition from a superfluid to a Mott insulator state. This is observed experimentally in atoms confined in a three-dimensional optical lattice [18] (see Fig. 1.6) and theoretically by using mean field calculation [17].

The second quantized BH Hamiltonian takes the form

$$\hat{\mathcal{H}} = -t \sum_{\langle i,j \rangle} \left(a_i^\dagger a_j + H.c. \right) + \frac{U}{2} \sum_{i=1}^{L} \hat{n}_i (\hat{n}_i - 1), \qquad (1.15)$$
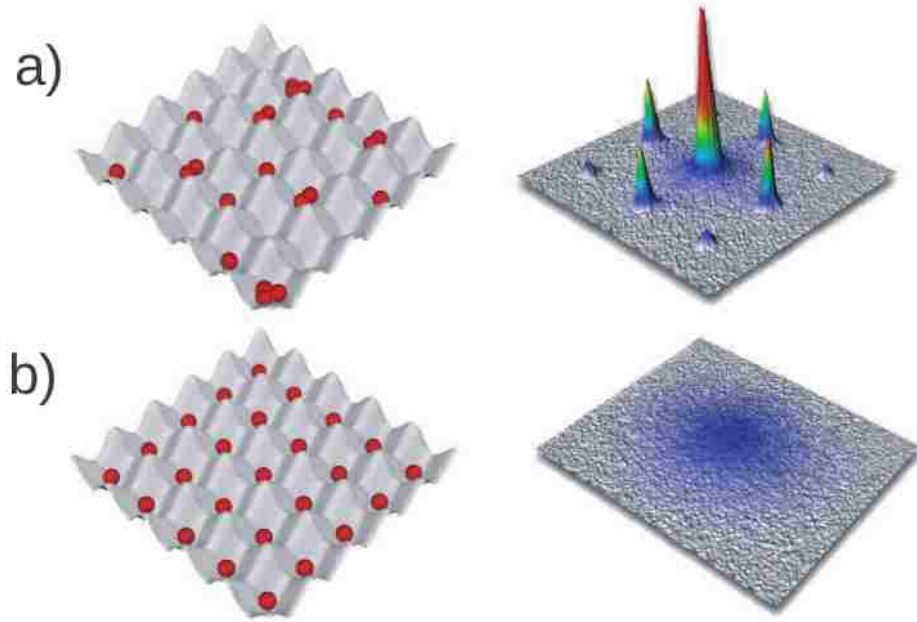
Figure 1.6: The superfluid to Mott insulator experiment by Greiner et al. [18]. Top left figure in a) shows the superfluid state, the atoms are free to hop around the lattice. Right figure shows a multiple wave interference pattern upon release and expansion of the condensate. Bottom left figure in b) shows the Mott behavior of the atoms with the same number of atoms per site. There is no matter wave interference as shown in right bottom panel.

where L is the number of lattice sites. Creation and annihilation operators $a_i^\dagger$ and a_i satisfy bosonic commutation rules, $[a_i, a_j] = [a_i^\dagger, a_j^\dagger] = 0$, $[a_i, a_j^\dagger] = \delta_{ij}$, and $\hat{n}_i = a_i^\dagger a_i$ is the operator that measures the number of bosons on site i. The parameter t is the global magnitude of the hopping integrals. The sum $\sum_{\langle i,j \rangle}$ runs over all distinct pairs of first neighboring sites i and j and the parameter U determines the strength of the on-site interaction.

At zero temperature the physics described by the BH Hamiltonian can be divided into two different regimes. One is the interaction dominated regime where t is much smaller than U, and the system is in the Mott Insulator (MI) phase. The other is the kinetic energy dominated regime which overcomes the repulsion energy cost, and the system exhibits superfluid (SF) properties.
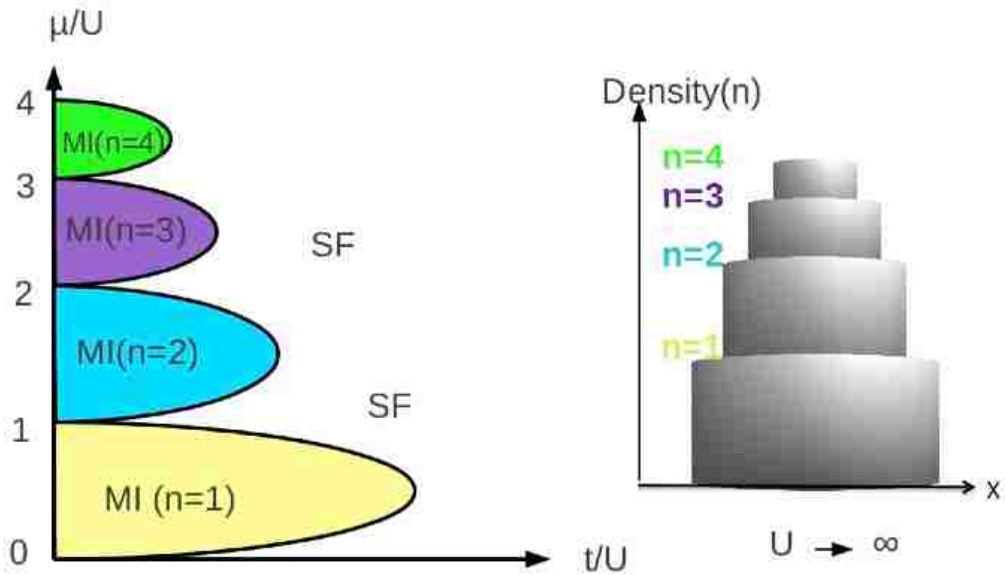
Figure 1.7: Ground state phase diagram of the Bose Hubbard model (BH) with chemical potential over interaction (μ/U) as a function of hopping over interaction (t/U). This is the superfluid (SF) to Mott insulator (MI) transition phase diagram for the BH model. Left panel: The Mott lobes have an integer occupation number and the other regions are SF. Right panel: The "wedding cake" structure of the density at the strong interaction regime.

The onset of superfluidity comes as a consequence of the competition between the kinetic energy and the interaction energy. The kinetic energy tries to delocalize particles by increasing their number fluctuations and the interaction energy tries to localize particles by reducing their number fluctuations. In the superfluid regime, the kinetic energy term dominates and particles are delocalized over the lattice with equal relative phases between adjacent sites. Those particles exhibit an interference pattern when the lattice is turned off, as expected from an array of phase coherent matter wave sources. In this regime, quantum correlations can be neglected and the system can be described by a macroscopic wave function since the many body state is almost a product over identical single particle wave functions. The system is superfluid with a macroscopic well-defined phase called the SF phase. On the

other hand as interaction increases, an average kinetic energy required for an atom to hop from one site to the next becomes insufficient to overwhelm the interaction energy. Then, atoms tend to get localized at individual lattice sites and number fluctuations are small. The ground state of the system consists of localized atomic wave functions with a fixed number of atoms per site. This phase is identified as a MI phase and characterized by the existence of an energy gap. The gap is determined by the energy necessary to create one particle-hole pair because the lowest lying excitations are particle-hole excitations (adding and removing a particle from the system).

The ground state phase diagram in the left panel of Fig. 1.7 describes the SF to MI transition of the translational invariant system represented by Eq. (1.15). The ground state exhibits lobe-like MI phases in the $t/U - \mu/U$ plane. The existence of the Mott gap means that the μ/U can be changed within the gap without changing the density. When the system is placed in a trap, it shows density plateaus corresponding to the Mott state. This leads to a "wedding cake" structure of the density profile as shown in the right panel of Fig. 1.7. Each Mott lobe has a fixed integer density. Inside these Mott lobes, the compressibility is zero, which is defined as $\kappa = \dfrac{\partial \rho}{\partial \mu}$ with ρ the average density of the system. The physics behind this phase diagram can be understood by allowing a particle to hop around the lattice. If you start at a point in the Mott lobe and increase μ/U by keeping t/U fixed, there is a point that lets an extra particle move freely around the lattice and enter the SF regime. Similarly, by decreasing μ/U from a point in the Mott lobe, there is a point that removes a particle from the system and enters to SF phase. The width of the lobes decreases with t/U and shape of the lobes depends on system dimension [89]. Distance between the upper and lower boundaries of the lobe for fixed t/U is the energy gap.

Mott insulator phase occurs only at integer densities, while non-integer densities lie entirely in the superfluid phase. Thus the phase diagram has two continuous phase transitions. They belong to two different universality classes. At a commensurate density, the transition driven by phase fluctuations belongs to the (d+1)- dimensional XY universality class

(Kosterlitz Thouless transition) [90–93]. On the other hand, the transition driven by density fluctuation belongs to generic superfluid to Mott insulator transition [90–92]. Basic concepts of phase transition are discussed in Appendix B.

1.7 Thesis Structure

The overall goal of this thesis is to study equilibrium interacting problems of cold bosons loaded in optical lattices by using analytical and computational techniques. Although there has been a considerable amount of work done to study the Bose Hubbard (BH) model and its variants, still there are many important issues remaining to be understood. Among them, exotic quantum phases are always exciting and important. This thesis describes several problems studied by using exact quantum Monte Carlo (QMC) simulations. Although most of the work is theoretical, discussions of its connection to the ongoing experimental research are included.

This thesis is organized as follows. Chapter 2 describes the computational algorithm to engineer such large system sizes and emulate accurately quantum systems. The finite temperature path integral QMC Stochastic Green Function method enables us to exactly solve any complicated interaction by doing updates efficiently in time and space. This chapter reviews this formalism and clarifies some algorithmic modification completed during my Ph.D. research.

Chapter 3 describes the recently developed new confining method for ultra-cold atoms on optical lattices. This off-diagonal confinement method constrains atoms via a hopping integral that decreases as a function of the distance from the center of the lattice. We show that this method can lead to lower temperatures than the existing diagonal confinement method.

In Chapter 4 we study the inhomogeneous Bose Hubbard model. This is an extension of the well known homogeneous Bose Hubbard model. The ground state phase diagram of interacting bosons on a ring-shape lattice with a region of weak hopping integrals is addressed

here. We found a novel phase, we called local Mott phase, in addition to the usual Mott insulator and superfluid phases present in the homogeneous Bose Hubbard model. Further, new experimental descriptions and atomtronics applications of the model are discussed.

Chapter 5 focuses on the two species Bose Hubbard model due to increasing interest in mixtures of atoms. Novel phases can arise due to the complexity associated with multiple species. The phase diagram of the model displays multiple phases including ordered and coexistence phases. By changing doping we find a total of five distinct phases. The phase diagram includes a normal liquid phase at higher temperature, and four different phases at lower temperature. Away from half filling the phase diagram displays a ferromagnetic phase separated phase inside the superfluid region at even lower temperatures. In this novel phase separated region, the heavy species has Mott behavior with integer filling, while the lighter species shows phase separated Mott and superfluid behaviors. The global entropy of this phase is relatively high which may provide a new avenue to obtain a polarized phase or a Mott insulator in cold atom experiments. Complex quantum phases in strongly correlated systems are very useful due to their possible functionality to make advanced devices.

Finally Chapter 6 presents the conclusion of this thesis. Further the basic concepts of quantum and classical phase transitions are reviewed in Appendix B.

Chapter 2
Stochastic Green Function Algorithm

In condensed matter physics, we are interested in macroscopic systems with about 10^{23} particles. Solving the Schrödinger equation directly for such a system is impossible. Over the years, many numerical methods have arisen with powerful computer technology. Exact Diagonalization (ED) can be used to solve small clusters exactly. Variational approaches are biased by the priori information about the system and can hardly be trusted to reveal new features. They only provide information about the ground state. Density Matrix Renormalization Group introduced with the concept of entanglement, but it is still limited to the study of one dimensional systems. The widely used Quantum Monte Carlo (QMC) simulations allow us to sample a region of phase space by exploring it in a stochastic manner. QMC is computationally exact within statistical errors, due to the stochastic processes used in the algorithm. There are several QMC methods that have been developed to solve many-body systems, such as variational, diffusion, path integral, worm, auxiliary field, determinant, stochastic series expansion, loop algorithm, and stochastic green function [85, 98–102]. Among them, the Stochastic Green Function (SGF) algorithm is designed to solve equilibrium interacting bosonic problems [102–104]. It can simulate any complicated interaction of the lattice Hamiltonian with the form of $\hat{\mathcal{H}} = \hat{\mathcal{V}} - \hat{\mathcal{T}}$, where $\hat{\mathcal{V}}$ is the diagonal part of the Hamiltonian in a chosen occupation number basis, and $\hat{\mathcal{T}}$ is the non diagonal part of the Hamiltonian which is assumed to have positive matrix elements only. The SGF algorithm is designed for a canonical ensemble, but a simple extension allows us to simulate the grand canonical ensemble too.

This method is very useful to solve problems with several species of particles. Since it is numerically difficult to control several numbers of particles in the grand-canonical ensemble, this algorithm is the best way to solve those kind of complex systems. The SGF can be used to calculate any static quantity. Another important property of the algorithm is its access to n-body Green functions which allows us to calculate important quantities such as the momentum distribution function, an important quantity used to connect theory and experiments. In this chapter I review the theory of the SGF algorithm by following references [102–104], and explain some algorithmic modification completed during my Ph.D. research.

2.1 The Partition Function and the Extended Partition Function

The algorithm samples the partition function $Z(\beta) = Tre^{-\beta\hat{\mathcal{H}}}$ with an inverse temperature β by operating directly on physical states. By expanding the non-diagonal part of the Hamiltonian, $\hat{\mathcal{T}}$, in imaginary time axis we can write a partition function suited for the worldline representation. Hence, the partition function in the interaction representation can be expressed as time ordered exponential integration of non diagonal operators. By summing all configurations it can be written as

$$\mathcal{Z}(\beta) = Tre^{-\beta\hat{V}}\sum_{n\geq 0}\int_{0<\tau_1<...<\tau_n<\beta}\hat{\mathcal{T}}(\tau_n)...\hat{\mathcal{T}}(\tau_2)\hat{\mathcal{T}}(\tau_1)\ d\tau_1...d\tau_n \tag{2.1}$$

where the time evolution of the operator $\hat{O}$ is defined as $\hat{O}(\tau) = e^{\tau\hat{V}}\hat{O}e^{-\tau\hat{V}}$. By inserting a complete set of states in occupation number basis ($\hat{\mathcal{V}}$ is diagonal in this basis) $I = \sum_{\Psi}|\Psi><\Psi|$ in between non diagonal operators $\mathcal{T}$s, we can rewrite the partition function as

$$\mathcal{Z}(\beta) = \sum_{n\geq 0}\sum_{\Psi_1,...,\Psi_n}e^{-\beta\hat{V}}\int_{0<\tau_1<...<\tau_n<\beta}\langle\Psi_0|\hat{\mathcal{T}}(\tau_n)|\Psi_{n-1}\rangle$$
$$...\langle\Psi_2|\hat{\mathcal{T}}(\tau_2)|\Psi_1\rangle\langle\Psi_1|\hat{\mathcal{T}}(\tau_1)|\Psi_0\rangle d\tau_1...d\tau_n. \tag{2.2}$$

Since the same state Ψ_0 appears both at the beginning and the end of the imaginary time evolution, the structure of the partition function is appropriate for a world line description. Therefore, worldlines, the trajectories of the particles, are periodic with this inverse temperature β. To sample the partition function in Eq. (2.2), an extended partition function is defined by breaking up the exponential part $e^{-\beta\hat{\mathcal{H}}}$ at imaginary time τ and by introducing the Green Operator $\hat{\mathcal{G}}$ as $\mathcal{Z}(\beta,\tau) = Tr e^{-(\beta-\tau)\hat{\mathcal{H}}}\hat{\mathcal{G}}e^{-\tau\hat{\mathcal{H}}}$. After repeating the same procedure done to get Eq. (2.2), the extended partition function takes the form

$$
\mathcal{Z}(\beta,\tau) = \sum_{n\geq 0}\sum_{\Psi_1...\Psi_n} e^{-\beta\hat{V}}\int_{0<\tau_1<...<\tau_n<\beta}\langle\Psi_0|\hat{\mathcal{T}}(\tau_n)|\Psi_{n-1}\rangle
$$
$$
...\langle\Psi_L|\hat{\mathcal{G}}(\tau)|\Psi_R\rangle...\langle\Psi_2|\hat{\mathcal{T}}(\tau_2)|\Psi_1\rangle\langle\Psi_1|\hat{\mathcal{T}}(\tau_1)|\Psi_0\rangle d\tau_1...d\tau_n. \qquad (2.3)
$$

The extended partition function $\mathcal{Z}(\beta,\tau)$ includes all diagonal configurations that belong to the normal partition function $\mathcal{Z}(\beta)$, and non-diagonal configurations that do not belong to $\mathcal{Z}(\beta)$. Therefore the extended partition function can be written as the sum of those all configurations;

$$
\mathcal{Z}(\beta,\tau) = \mathcal{Z}(\beta) + \sum_{\Psi_L\neq\Psi_R}\text{Tr } e^{-(\beta-\tau)\hat{\mathcal{H}}}|L\rangle\langle\Psi_L|\hat{\mathcal{G}}|\Psi_R\rangle\langle\Psi_R|e^{-\tau\hat{\mathcal{H}}}. \qquad (2.4)
$$

The Green operator $\hat{\mathcal{G}}$ has a matrix element between any states which is the number of broken worldlines between the states as $\langle\psi_L|\mathcal{G}|\Psi_R\rangle = g(|n^L - n^R|)$, where g() is a decreasing function of discontinuity (the number of broken worldlines), as g(0)=1 when the matrix element of $\hat{\mathcal{G}}$ gets diagonal. The algorithm should evolve between two diagonal configurations via many non-diagonal configurations. The Green operator $\hat{\mathcal{G}}$ will propagate through the operator string by allowing the transition from one configuration to another. This can be done by adding and removing $\hat{\mathcal{T}}$ operators to the operator string.
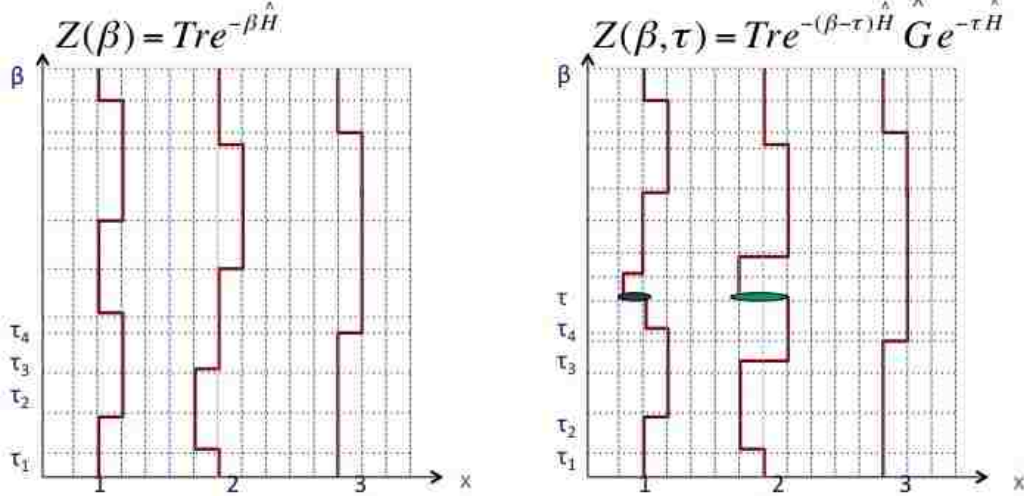
Figure 2.1: Worldlines representation of the normal partition function (left) and the extended partition function (right). This is a one-dimensional system which has three particles, 1, 2 and 3. Lines show the particle paths called worldlines. X is the space axis and β is the imaginary time axis. Worldlines are periodic at time β. Horizontal jumps are $\hat{\mathcal{T}}$ operators and green ovals at time τ shows the Green operator, $\hat{\mathcal{G}}$ that moves through the operator string in space and time.

2.2 Update Scheme

As described in the above section, by creating and destroying $\hat{\mathcal{T}}$ operators with given probabilities, the Green operator $\hat{\mathcal{G}}$ allows us to sample the terms of the partition function expansion as shown in Fig. 2.1. First we generate the configurations of the extended partition function by using a empty string of $\hat{\mathcal{T}}$ operators. That means that we only have diagonal configurations of $\hat{\mathcal{G}}$ at time τ, the left and the right wave-functions of $\hat{\mathcal{G}}$ are the same but randomly chosen. The propagation direction of the Green operator $\hat{\mathcal{G}}$ can be selected either by removing a $\hat{\mathcal{T}}$ operator or adding a $\hat{\mathcal{T}}$ operator to the left or to the right of $\hat{\mathcal{G}}$. So if you choose the propagation of $\hat{\mathcal{G}}$ to the left, the probability of the chosen direction is $P^{LR}(\leftarrow)$. Next we have to choose either a creation or a destruction by following the update scheme as shown in Fig. 2.2. If it is a creation, the probability for creation is $P^{LR}_{\leftarrow}(\dagger)$ and if it is a destruction, the probability for destruction is $1 - P^{LR}_{\leftarrow}(\dagger)$. After choosing the direction, it should follow the update scheme as follows:

- Creation: A state $\psi_{R'}$ will be chosen with the probability $1 - P_{\leftarrow}^{LR}(\psi_{R'})$ and a $\hat{\mathcal{T}}$ operator is inserted on the right of $\hat{\mathcal{G}}(\tau)$ at time $\tau_{R'} = \tau$; $|\psi_{R'}\rangle\langle\psi_{R'}|\hat{\mathcal{T}}(\tau_{R'})$. Next the $\hat{\mathcal{G}}(\tau)$ operator takes a time shift $\Delta\tau$ to the left as $\Delta\tau = \tau_L - \tau_{R'}$. The probability to choose this time shift is $P_{\leftarrow}^{LR'}(\Delta\tau)$. The probability to go through the update scheme is $P_{\leftarrow}^{LR'}(go)$ and not to continue the update is $1 - P_{\leftarrow}^{LR'}(go)$.

- Destruction: The time index the $\hat{\mathcal{G}}(\tau)$ operator will take is τ_L. The left $\hat{\mathcal{T}}$ operator will remove $\hat{\mathcal{T}}(\tau_L)|\psi_L\rangle\langle\psi_L|$. The probability to go through the update scheme loop is $P_{\leftarrow}^{L-1R}(go)$ and not to continue is $1 - P_{\leftarrow}^{L-1R}(go)$.

- Update continue: The next creation and destruction will be chosen until the update is ended.

Since the Green operator $\hat{\mathcal{G}}$ has a finite probability to move in the same direction continuously, this update scheme is directed in the imaginary time axis. Further, the $\hat{\mathcal{T}}$ operator can be inserted to the operator string at any imaginary time indices. Therefore, the update of this algorithm ensures ergodicity.

2.3   Detailed Balance

By considering a random walk through the configurational space, the so-called Markov chain of configurations, the probability of being in an initial configuration P_i and a final configuration P_f can be related with the probability to propose a transition from an initial to a final configuration $S_{i\to f}$ and a final to an initial configuration $S_{f\to i}$. This is the detailed balance equation:

$$P_i S_{i\to f} A_{i\to f} = P_f S_{f\to i} A_{f\to i}, \tag{2.5}$$

where the acceptance rate for the transition from the initial to the final configuration is $A_{i\to f}$ and the acceptance rate for the transition from the final to the initial configuration is $A_{f\to i}$.

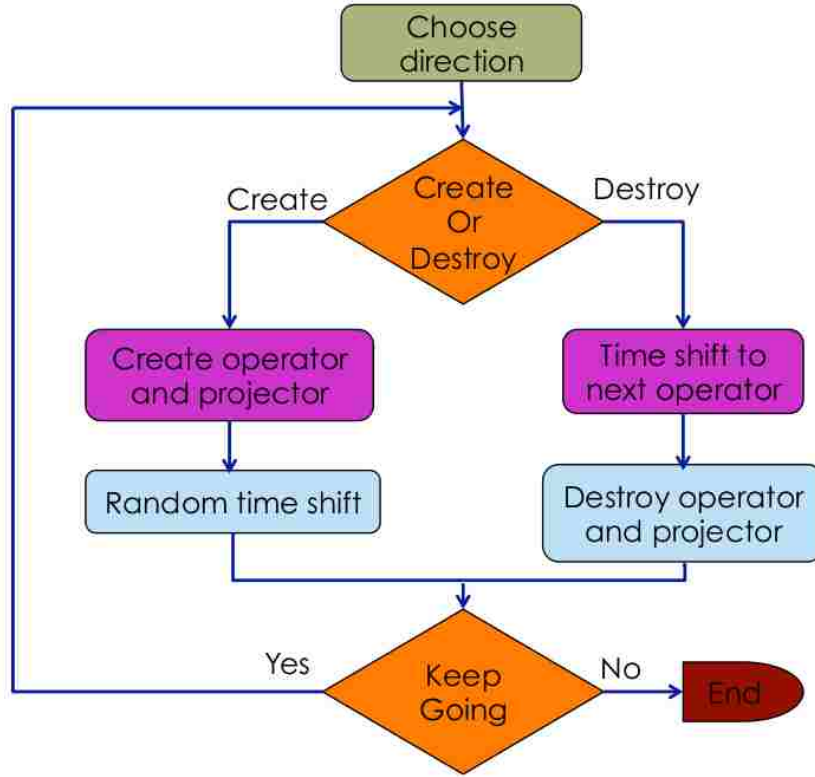Figure 2.2: Flow diagram for the directed update scheme for the SGF (see text for details).

Next we use Metropolis solution to find the acceptance rate as

$$A_{i \to f} = min(1, q_{i \to f}), \quad A_{f \to i} = min(1, q_{f \to i}) \tag{2.6}$$

with the acceptance factors

$$q_{i \to f} = \frac{P_f S_{f \to i}}{P_i S_{i \to f}}, \quad q_{f \to i} = \frac{P_i S_{i \to f}}{P_f S_{f \to i}}. \tag{2.7}$$

2.3.1 Probabilities

The probability to go through the update scheme can be calculated by satisfying detailed balance and ergodicity. Therefore, we can choose those probabilities more efficiently. In this way we can generate the operator string with the extended Boltzmann weight.

As an example:

When the SGF algorithm chooses to create a non diagonal term $\hat{\mathcal{T}}$ in the right direction, it will insert the term as $\langle \Psi_L | \hat{\mathcal{G}}(\tau) | \Psi_R \rangle \longrightarrow \langle \Psi_L | \hat{\mathcal{G}}(\tau) | \Psi \rangle \langle \Psi | \hat{\mathcal{T}}(\tau) | \Psi_R \rangle$ to the right, and then a time shift to $\hat{\mathcal{G}}$ is made as $\hat{\mathcal{G}}(\tau) \longrightarrow \hat{\mathcal{G}}(\tau + \Delta\tau)$. By choosing the primed and non-primed labels for the final and initial configurations respectively, the Boltzmann weight P_i of the initial configuration for the process

$$\langle \Psi_L | \hat{\mathcal{G}}(\tau) | \Psi_R \rangle \longrightarrow \langle \Psi'_L | \hat{\mathcal{G}}(\tau') | \Psi'_R \rangle \langle \Psi'_R | \hat{\mathcal{T}}(\tau'_R) | \Psi'_{R1} \rangle \tag{2.8}$$

can be written as

$$P_i \quad \propto \quad \langle \psi_L | \hat{\mathcal{G}}(\tau) | \psi_R \rangle \propto \langle \psi_L | \hat{\mathcal{G}} | \psi_R \rangle e^{\tau(V_L - V_R)}. \tag{2.9}$$

Similarly, the Boltzmann weight of the final configuration is

$$
\begin{aligned}
P_f \quad &\propto \quad \langle \psi'_L | \hat{\mathcal{G}}(\tau') | \psi'_R \rangle \langle \psi'_R | \hat{\mathcal{T}}(\tau'_R) | \psi'_{R1} \rangle \\
&\propto \quad \langle \psi'_L | \hat{\mathcal{G}} | \psi'_R \rangle \langle \psi'_R | \hat{\mathcal{T}} | \psi'_{R1} \rangle e^{\tau'(V'_L - V'_R)} e^{\tau'_R(V'_R - V'_{R1})}.
\end{aligned}
\tag{2.10}
$$

The probability to choose the transition from the initial to the final configuration, $S_{i \to f}$, can be written as the product of all the probabilities in the process of the update scheme such as the probability to choose a propagation to the left, do a creation, choose the new state, choose the time for $\hat{\mathcal{G}}$ and stop the update scheme;

$$S_{i \to f} \quad = \quad P^{LR}(\leftarrow) P^{LR}_{\leftarrow}(\dagger) P^{LR}_{\leftarrow}(\psi'_R) P^{L'R'}(\tau' - \tau'_R)(1 - P^{L'R'}_{\leftarrow}(go)). \tag{2.11}$$

The probability to choose the transition from the final to the initial configuration, $S_{f\to i}$, can be written as the multiplication of all the probabilities in the process of the update scheme such as the probability to choose a propagation to the right, do an annihilation and stop the update scheme. This is the reverse process of the above;

$$S_{f\to i} = P^{L'R'}(\to)(1 - P_\to^{L'R'}(\dagger))(1 - P_\to^{LR}(go)). \tag{2.12}$$

Now by identifying the the relationships $V_{L'} = V_L$, $V'_{R1} = V_R$ and $\tau'_R = \tau$, the acceptance factor can be expressed as

$$q_\leftarrow^c = \frac{\langle\psi_L|\hat{\mathcal{G}}|\psi'_R\rangle\langle\psi'_R|\hat{\mathcal{T}}|\psi_R\rangle e^{-(\tau'-\tau'_R)(V'_R-V'_L)}}{\langle\psi_L|\hat{\mathcal{G}}|\psi_R\rangle P^{LR}(\leftarrow)P_\leftarrow^{LR}(\dagger)P_\leftarrow^{LR}(\psi'_R)} \frac{P^{L'R'}(\to)(1 - P_\to^{L'R'}(\dagger))(1 - P_\to^{LR}(go))}{P^{LR}(\leftarrow)P_\leftarrow^{LR}(\dagger)(1 - P_\leftarrow^{L'R'}(go))}. \tag{2.13}$$

If it is possible to cancel the exponential part of this acceptance factor by choosing an exponential distribution for the Green operator time shift as follows:

$$P_\leftarrow^{LR}(\Delta\tau) = \frac{(V'_R - V_L)e^{\Delta\tau(V'_R-V_L)}}{1 - e^{-(\tau_L-\tau_R)(V_R-V_L)}}, \tag{2.14}$$

$$P_\to^{LR}(\Delta\tau) = \frac{(V_L - V_R)e^{\Delta\tau(V_L-V_R)}}{1 - e^{-(\tau_L-\tau_R)(V_L-V_R)}}. \tag{2.15}$$

By writing the probability for choosing an important state as proportional to the weight of the new matrix elements;

$$P_\leftarrow^{LR}(\psi) = \frac{\langle\psi_L|\hat{\mathcal{G}}|\psi\rangle\langle\psi|\hat{\mathcal{T}}|\psi_R\rangle}{\langle\psi_L|\hat{\mathcal{G}}\hat{\mathcal{T}}|\psi_R\rangle}, \tag{2.16}$$

$$P_\to^{LR}(\psi) = \frac{\langle\psi_L|\hat{\mathcal{T}}|\psi\rangle\langle\psi|\hat{\mathcal{G}}|\psi_R\rangle}{\langle\psi_L|\hat{\mathcal{T}}\hat{\mathcal{G}}|\psi_R\rangle}, \tag{2.17}$$

we can rewrite the acceptance factor as independent of intermediate configurations as

$$q_{\leftarrow}^c = \frac{\langle\psi_L|\hat{\mathcal{G}}\hat{\mathcal{T}}|\psi_R\rangle(1 - P_{\rightarrow}^{LR}(go))}{\langle\psi_L|\hat{\mathcal{G}}|\psi_R\rangle P^{LR}(\leftarrow)P_{\leftarrow}^{LR}(\dagger)} \frac{P^{L'R'}(\rightarrow)(1 - P_{\rightarrow}^{L'R'}(\dagger))[1 - e^{-(\tau_L' - \tau_R')(V_R' - V_L')}]}{(V_R' - V_L')(1 - P_{\leftarrow}^{L'R'}(go))}.\text{(2.18)}$$

Another important factor you can recognize is $q_{\rightarrow}^d = 1/q_{\leftarrow}^c$. Therefore, the left propagation acceptance factor with a destruction can be written as

$$q_{\leftarrow}^d = \frac{(V_R - V_L)(1 - P_{\rightarrow}^{LR}(go))}{P^{LR}(\leftarrow)(1 - P_{\leftarrow}^{LR}(\dagger))[1 - e^{-(\tau_L - \tau_R)(V_R - V_L)}]} \frac{\langle\psi_L'|\hat{\mathcal{G}}|\psi_R'\rangle P^{L'R'}(\leftarrow)P_{\leftarrow}^{L'R'}(\dagger)}{\langle\psi_L'|\hat{\mathcal{G}}\hat{\mathcal{T}}|\psi_R'\rangle(1 - P_{\rightarrow}^{L'R'}(go))}.\text{(2.19)}$$

If we choose $q_{\leftarrow}^c = q_{\leftarrow}^d$, we are doing a uniform sampling. In this way we can find the creation probabilities as

$$P_{\leftarrow}^{LR}(\dagger) = \frac{\langle\psi_L|\hat{\mathcal{G}}\hat{\mathcal{T}}|\psi_R\rangle}{\langle\psi_L|\hat{\mathcal{G}}\hat{\mathcal{T}}|\psi_R\rangle + \langle\psi_L|\hat{\mathcal{G}}|\psi_R\rangle\frac{(V_L - V_R)}{1 - e^{-(\tau_L - \tau_R)(V_L - V_R)}}},\tag{2.20}$$

$$P_{\rightarrow}^{LR}(\dagger) = \frac{\langle\psi_L|\hat{\mathcal{T}}\hat{\mathcal{G}}|\psi_R\rangle}{\langle\psi_L|\hat{\mathcal{T}}\hat{\mathcal{G}}|\psi_R\rangle + \langle\psi_L|\hat{\mathcal{G}}|\psi_R\rangle\frac{(V_R - V_L)}{1 - e^{-(\tau_L - \tau_R)(V_R - V_L)}}}.\tag{2.21}$$

We can write $P_{\leftarrow}^{LR}(go)$ and $P_{\rightarrow}^{LR}(go)$ as follows:

$$P_{\leftarrow}^{LR}(go) = \alpha\min\left(1, \frac{f_{\rightarrow}^{LR}}{f_{\leftarrow}^{LR}}\right),\tag{2.22}$$

$$P_{\rightarrow}^{LR}(go) = \alpha\min\left(1, \frac{f_{\leftarrow}^{LR}}{f_{\rightarrow}^{LR}}\right),\tag{2.23}$$

by writing

$$f_{\leftarrow}^{LR} = \frac{\langle\psi_L|\hat{\mathcal{G}}|\psi_R\rangle}{\langle\psi_L|\hat{\mathcal{G}}\hat{\mathcal{T}}|\psi_R\rangle + \langle\psi_L|\hat{\mathcal{G}}|\psi_R\rangle\frac{(V_L - V_R)}{1 - e^{-(\tau_L - \tau_R)(V_L - V_R)}}},\tag{2.24}$$

$$f_{\rightarrow}^{LR} = \frac{\langle\psi_L|\hat{\mathcal{G}}|\psi_R\rangle}{\langle\psi_L|\hat{\mathcal{T}}\hat{\mathcal{G}}|\psi_R\rangle + \langle\psi_L|\hat{\mathcal{G}}|\psi_R\rangle\frac{(V_R - V_L)}{1 - e^{-(\tau_L - \tau_R)(V_R - V_L)}}}.\tag{2.25}$$

Here α is an optimization parameter to be chosen between 0 and 1. Within those choices, we can write the acceptance factor in any update without the details of the intermediate configuration, so that it only depends on the initial and final configurations:

$$q^c_{\leftarrow} = q^d_{\leftarrow} = \frac{P^{L'R'}(\rightarrow)Q^{LR}(\leftarrow)}{P^{LR}(\rightarrow)Q^{L'R'}(\leftarrow)}, \tag{2.26}$$

$$q^c_{\rightarrow} = q^d_{\rightarrow} = \frac{P^{L'R'}(\leftarrow)Q^{LR}(\rightarrow)}{P^{LR}(\leftarrow)Q^{L'R'}(\rightarrow)}, \tag{2.27}$$

where,

$$Q^L R(\leftarrow) = \frac{1 - P^{LR}_{\rightarrow}(go)}{f^{LR}_{\leftarrow}}, \tag{2.28}$$

$$Q^L R(\rightarrow) = \frac{1 - P^{LR}_{\leftarrow}(go)}{f^{LR}_{\rightarrow}}, \tag{2.29}$$

and

$$P^{LR}(\leftarrow) = \frac{Q^{LR}(\leftarrow)}{Q^{LR}(\leftarrow) + Q^{LR}(\bar{\sigma})}, \tag{2.30}$$

$$P^{LR}(\rightarrow) = \frac{Q^{LR}(\rightarrow)}{Q^{LR}(\rightarrow) + Q^{LR}(\leftarrow)}. \tag{2.31}$$

If we define $\phi^{LR} = Q^{LR}(\leftarrow) + Q^{LR}(\rightarrow)$, we can write the unique acceptance factor for any update as

$$q = \frac{\phi^{LR}}{\phi^{L'R'}}. \tag{2.32}$$

By defining $\phi_i = \phi^{LR}$ and $\phi_f = \phi^{L'R'}$, we can rewrite detail balance as

$$\frac{P_f \phi_f S_{f\rightarrow i}}{P_i \phi_i S_{i\rightarrow f}} = 1. \tag{2.33}$$

This means that accepting all transitions with a probability 1 is equivalent to sampling the extended partition function with the pseudo-Boltzmann weight $P\phi$ instead of the true Boltzmann weight P of the normal partition function.

In this terminology we can calculate statistical average of any operator $\hat{\mathcal{O}}$ with a simple renormalization as

$$\langle\hat{\mathcal{O}}\rangle_P = \frac{\langle\hat{\mathcal{O}}/\phi\rangle_{P\phi}}{\langle 1/\phi\rangle_{P\phi}}. \tag{2.34}$$

2.3.2 Measurements

By considering any operator $\hat{\mathcal{O}}$ in the interaction representation, $\hat{\mathcal{O}}(\tau) = e^{\tau\hat{\mathcal{V}}}\hat{\mathcal{O}}e^{-\tau\hat{\mathcal{V}}}$, the SGF algorithm allows us to calculate any physical quantity. When we measure a statistical average, we need to understand the difference between the SGF statistical average and the Boltzmann statistical average. These averages can be written as

$$\langle\hat{\mathcal{O}}\rangle^S = \frac{1}{\mathcal{Z}}\text{Tr}\ \hat{\mathcal{A}}e^{-\beta\hat{\mathcal{H}}}, \tag{2.35}$$

$$\langle\hat{\mathcal{O}}\rangle^{SGF} = \frac{1}{\mathcal{Z}}\text{Tr}\ e^{-\beta\hat{\mathcal{V}}}\mathbf{T}_\tau\left[\hat{\mathcal{A}}e^{\int_0^\beta \hat{\mathcal{T}}(\tau)d\tau}\right]. \tag{2.36}$$

If the operator is independent of imaginary time, those two statistical averages are equivalent.

The left state $|\psi_L\rangle$ and the right state $|\psi_R\rangle$ of the Green operator are related to the extended Boltzmann weight of the extended partition function as

$$P(\psi_L, \psi_R) = \frac{\langle\psi_L|\hat{\mathcal{G}}|\psi_R\rangle\langle\psi_R|e^{-\beta\hat{\mathcal{H}}}|\psi_L\rangle}{\mathcal{Z}(\beta, \tau)}. \tag{2.37}$$

By using the Boltzmann weight, we can measure desired operator $\hat{\mathcal{O}}$ by considering the expectation value of the operator

$$\langle\hat{\mathcal{O}}\rangle = \frac{\text{Tr}\ \hat{\mathcal{O}}e^{-\beta\hat{\mathcal{H}}}}{\mathcal{Z}(\beta)} = \frac{\sum_\psi\langle\psi|\hat{\mathcal{O}}e^{-\beta\hat{\mathcal{H}}}|\psi\rangle}{\mathcal{Z}(\beta)}. \tag{2.38}$$

Since all diagonal matrix elements of $\hat{\mathcal{G}}$ are equal to 1 within the set of complete states, we can rewrite the equation as

$$\langle\hat{\mathcal{O}}\rangle = \frac{\sum\limits_{\psi_L,\psi_R}\langle\psi_L|\hat{\mathcal{O}}|\psi_R\rangle\langle\psi_R|e^{-\beta\hat{\mathcal{H}}}|\psi_L\rangle}{\mathcal{Z}(\beta)} = \frac{\sum\limits_{\psi_L,\psi_R}\frac{\langle\psi_L|\hat{\mathcal{O}}|\psi_R\rangle}{\langle\psi_L|\hat{\mathcal{G}}|\psi_R\rangle}P(\psi_L,\psi_R)}{\sum\limits_{\psi_L,\psi_R}\delta_{\psi_L,\psi_R}P(\psi_L,\psi_R)}, \qquad (2.39)$$

where δ_{ψ_L,ψ_R} is the Krönecker delta.

With an importance sampling $S_{\psi_L\psi_R}$ over S samples of states $|\psi_L\rangle$ and $|\psi_R\rangle$ with the distribution $P(\psi_L,\psi_R)$ and taking D as the number of diagonal configurations in the set of samples

$$\langle\hat{\mathcal{O}}\rangle = \lim_{S\to\infty}\frac{\sum\limits_{S_{\psi_L\psi_R}}\frac{\langle\psi_L|\hat{\mathcal{O}}|\psi_R\rangle}{\langle\psi_L|\hat{\mathcal{G}}|\psi_R\rangle}}{\sum\limits_{S_{\psi_L\psi_R}}\delta_{\psi_L,\psi_R}} = \lim_{S\to\infty}\frac{1}{D}\sum\limits_{S_{\psi_L\psi_R}}\frac{\langle\psi_L|\hat{\mathcal{O}}|\psi_R\rangle}{\langle\psi_L|\hat{\mathcal{G}}|\psi_R\rangle}. \qquad (2.40)$$

By performing the renormalization discussed in (2.34), the $\hat{\mathcal{O}}$ becomes

$$\langle\hat{\mathcal{O}}\rangle = \lim_{S\to\infty}\frac{\sum\limits_{S_{\psi_L\psi_R}}\frac{\langle\psi_L|\hat{\mathcal{O}}/\phi|\psi_R\rangle}{\langle\psi_L|\hat{\mathcal{G}}|\psi_R\rangle}}{\sum\limits_{S_\psi}\langle\psi|1/\phi|\psi\rangle}. \qquad (2.41)$$

In this way we can measure any desired operator within the SGF algorithm.

2.4 Implementation

In the SGF algorithm, we have to calculate all the probabilities shown in the update scheme efficiently. Basically we have to consider the following two processes and design a better scaling to improve the efficiency of the SGF.

- The SGF algorithm chooses to create a non diagonal term $\hat{\mathcal{T}}$ in the right direction: $\langle\Psi_L|\hat{\mathcal{G}}(\tau)|\Psi_R\rangle \longrightarrow \langle\Psi_L|\hat{\mathcal{G}}(\tau)|\Psi_{R'}\rangle\langle\Psi_{R'}|\hat{\mathcal{T}}(\tau)|\Psi_R\rangle$ and a time shift to $\hat{\mathcal{G}}$ is made as $\hat{\mathcal{G}}(\tau) \longrightarrow \hat{\mathcal{G}}(\tau+\Delta\tau)$.

- The SGF algorithm chooses to destroy a non diagonal term $\hat{\mathcal{T}}$ in the right direction:

  $\langle \Psi_L | \hat{\mathcal{G}}(\tau) | \Psi_R \rangle \langle \Psi_R | \hat{\mathcal{T}}(\tau) | \Psi_{R-1} \rangle \longrightarrow \langle \Psi_L | \hat{\mathcal{G}}(\tau) | \Psi_{R-1} \rangle$ on the right without any time shift to $\hat{\mathcal{G}}$.

For any Hamiltonian non-diagonal terms scale linearly with the system size. The fastest way to do an update is logarithmic on the non-diagonal terms of the Hamiltonian. This is achieved a binary tree structure.

In the first process mentioned above, the creation, we need to test all possible projectors $|\Psi_{R'}\rangle\langle\Psi_{R'}|$, the number of solutions is proportional to the number of lattice sites L. The new projector is chosen with probability proportional to $\langle \Psi_L | \hat{\mathcal{G}}(\tau) | \Psi_{R'} \rangle \langle \Psi_{R'} | \hat{\mathcal{T}}(\tau) | \Psi_R \rangle$. A simple implementation, evaluating all these possibilities one by one will scale as L. Our new fast algorithm is able to perform this operation with $logL$ complexity. In this process, the projectors are categorized according to their offsets, the number of broken worldlines (see next paragraph). The number of possible offset values depends on the model, normally it is a few integers. Next the weights of the projectors belonging to a given category are stored in a binary tree whose parent nodes contain the sum of the weights of the children. Then choosing a particular projector can be done in two steps: (1) choosing an offset (constant scaling) and (2) selecting a leaf in the binary tree starting from the root by following a random path (log L scaling). This implementation is explained briefly as follows.

The relative probability we need will be the product of the matrix element $\langle \Psi_{R'} | \hat{\mathcal{T}}(\tau) | \Psi_R \rangle$ and the matrix element of the Green operator $\langle \Psi_L | \hat{\mathcal{G}}(\tau) | \Psi_{R'} \rangle$, which can be evaluated by the function $g(N_{LR'})$, which depends on the updated number of broken world lines, $N_{LR'} = \sum_i |n_i^L - n_i^{R'}|$, where i is the number of sites, n_i^L is the occupancy of state Ψ_L and $n_i^{R'}$ is the occupancy of state $\Psi_{R'}$. A few indices of the occupancies of Ψ'_R and Ψ_R will change due to the new insertion of a $\hat{\mathcal{T}}$ term. If this change of the occupation numbers is $\delta n_{i,k}$, the updated number of broken lines can be written as $N_{LR'} = N_{LR} + \delta n_{k,LR}$ with $\delta n_{k,LR} = \sum_i |n_i^L - n_i^R + \delta n_{i,k}| - |n_i^L - n_i^R|$, where $\delta n_{k,LR}$ is the additional number of broken lines (or the offset) and $\delta n_{i,k}$ is the change of occupancy due to the new insertion of a non-diagonal

Figure 2.3: The fast update procedure of SGF for a simple 1-D Hamiltonian which has 8 non-diagonal terms as discussed in the text.

term at the ith index. The number of possible offset values depends on the Hamiltonian, but not on the size of the lattice. This offset is always an integer and its values depend on the non-diagonal terms of the Hamiltonian; it may take the values -2, 0, and $+2$ for the simple models. Therefore, we can use these offset values to categorize the non-diagonal operators of the Hamiltonian. First we choose an offset and next the operator from the corresponding group. Then the term is inserted or removed from the original group of offsets and added to the final group. Those pairs of operators for each group are included in binary trees by using pointers to two children and the parent. Since the binary tree operations always have log(N) scale when it has N leaves, the method gives total complexity as $O(L \, log(L))$ when the system size is L.

A simple example for this updates in the tree structure is shown in Fig 2.3. First we make tree leaves. The number of leaves equals to the number of non-diagonal terms of the Hamiltonian. For this simple one dimensional case we have 8 terms. We know the first time offset $+2$ is the only one with non zero values, because there are a creation and a destruction in each term. Then we fill up the leaves by acting on each term in the initial state. Then we make a binary tree by adding those weights until it reaches a root node. Next we choose a term by using a random number and checking it with the weights of the tree. In this case we choose the 6th term. Then we have to change the right state to a new state. Then we go back and update all weights according to their offset. Finally we have to update all the values of the trees. Then those weights can be used to calculate the necessary probabilities which are the sum of all offsets times of the nodes.

There is another simplification for hard core bosons. In this special case, all the non diagonal matrix elements are either 0 or 1 because we know that all non diagonal matrix elements are given by the square root of the product of occupation numbers that are either 0 or 1. Therefore, matrix elements of the term $\hat{\mathcal{T}}$ are always either 0 or 1. This allows us to update the probabilities with a constant scaling instead of $log(L)$ in the binary tree structure. Here we simply build the list of terms that are allowed for each offset. When choosing a term, we first choose an offset, then we have to choose a term at random in the list of terms that are corresponding to the chosen offset. Since all terms have the same weight, we have to choose a particular term with a uniform distribution by using an integer random number in between [0,Num[where Num is the number of terms in the particular offset. This can be done in a constant time.

Chapter 3
Off-diagonal Confinement as a Cooling Method

In this chapter, I present a new confining method for ultra-cold bosons on optical lattices. In a recent letter [Phys. Rev. Lett. **104**, 167201 (2010)] my collaborators proposed this new method, which is based on off-diagonal confinement (ODC). This method was shown to have distinct advantages over the conventional diagonal confinement (DC), that makes use of a trapping potential, such as the existence of pure Mott phases and highly populated condensates. In this study, we show that the ODC method can also lead to lower temperatures than the DC method for a wide range of control parameters. Using exact diagonalization, we determine this range of parameters for the hard-core case; then we extend our results to the soft-core case by performing quantum Monte Carlo (QMC) simulations for both DC and ODC systems at fixed temperature and analyzing the corresponding entropies. We also propose a method for measuring the entropy in QMC simulations.

This work was done in collaboration with V. G. Rousseau, M. Jarrell, J. Moreno, and D. E. Sheehy. The material presented in this chapter has been published in Physical Review A [112]. My contribution in this project involved doing exact diagonalization, comparing the results with QMC simulations, performing QMC simulations on supercomputers (XSEDE, HPC@LSU and LONI), and analyzing the data.

V. G. Rousseau, K. Hettiarachchilage, M. Jarrell, J. Moreno, and D. E. Sheehy, *Using Off-diagonal Confinement as a Cooling Method*, Phys. Rev. A 82, 063631 (2010).

3.1 Introduction

With recent experimental developments on cold atoms in optical lattices, the interest in the Bosonic Hubbard model [37, 106] has dramatically increased. This model is characterized by a superfluid-to-Mott quantum phase transition for large onsite repulsion and integer values of the density of particles. In actual experiments atoms are confined to prevent them from leaking out of the lattice. Currently this can be obtained by applying a spatially dependent magnetic field [18]. A parabolic potential adds into the Hubbard model [108] to mimic the effect of the magnetic field. Therefore, the resulting model does not exhibit a true superfluid-to-Mott transition, since Mott regions always coexist with superfluid regions. This was predicted theoretically [108], and later confirmed experimentally [151].

Recently a new confining method was developed for ultra-cold atoms on optical lattices based on off-diagonal confinement (ODC) [111] where the atoms are confined via a hopping integral that decreases as a function of the distance from the center of the lattice. Since the confinement of the particles is due to the hopping or off-diagonal operators, they called it as *Off-Diagonal Confinement* (ODC), as opposed to the conventional diagonal confinement (DC) which makes use of a parabolic confinement potential that is reflected in the density profile [108]. For large on-site repulsion the ODC model exhibits pure Mott phases at commensurate filling while at other fillings it exhibits more populated condensates than the DC model. Another advantage of ODC is that simple energy measurements can provide insights into the Mott gap, while the presence of the harmonic potential may renormalize the value of the gap with respect to the uniform case [122].

Here is the description of ODC method for best cooling. We show that the new ODC method can lead to lower temperatures than the DC method for a wide range of control parameters. Producing low temperatures in experiments is challenging, especially with fermions for which laser cooling is not as efficient as for bosons.

In current experiments, fermions are cooled down by convection in the presence of cold bosons, leading to Bose-Fermi mixtures [123–126]. Achieving lower temperatures for bosonic condensates will therefore result in colder Bose-Fermi mixtures.

3.2   Model and Method

We consider bosons confined to a one-dimensional optical lattice with L sites and lattice constant $a = 1$. The Hamiltonian takes the form:

$$\hat{\mathcal{H}} = -\sum_{\langle i,j \rangle} t_{ij} \left(a_i^\dagger a_j + h.c. \right) + \frac{U}{2} \sum_i \hat{n}_i (\hat{n}_i - 1) + W \sum_i (i - L/2)^2 \hat{n}_i \qquad (3.1)$$

The creation and annihilation operators $a_i^\dagger$ and a_i satisfy bosonic commutation rules, $[a_i, a_j] = [a_i^\dagger, a_j^\dagger] = 0$, $[a_i, a_j^\dagger] = \delta_{ij}$, and $\hat{n}_i = a_i^\dagger a_i$ is the number of bosons on site i. The sum $\sum_{\langle i,j \rangle}$ runs over all distinct pairs of first neighboring sites i, j, and t_{ij} is the hopping integral between i and j. The parameter U is the strength of the local on-site interaction, and W describes the curvature of the external trapping potential.

In this work we consider the grand-canonical partition function,

$$\mathcal{Z} = \mathrm{Tr}\; e^{-\beta \left(\hat{\mathcal{H}} - \mu \hat{\mathcal{N}} \right)}, \qquad (3.2)$$

where $\beta = \dfrac{1}{k_B T}$, k_B is the Boltzmann constant and T the temperature. The chemical potential μ controls the average number of particles, $N = \langle \hat{\mathcal{N}} \rangle$, with $\hat{\mathcal{N}} = \sum_i \hat{n}_i$. The conventional DC model is obtained by setting $t_{ij} = 1$ for all pairs of first neighboring sites i, j, and using $W > 0$. For this model the value of L is irrelevant as long as it is sufficiently large to contain the whole gas. The ODC model is obtained by setting $W = 0$ and using a hopping integral t_{ij} that decreases as a function of the distance from the center of the lattice, and vanishes at the edges. For this model, L fully determines t_{ij} as described below.

Typically the temperature is not a control parameter in cold-atoms experiments, and once laser cooling has been performed, the system has a fixed entropy which can be considered the control parameter. Then the temperature can be estimated numerically knowing the isentropies of the system [127]. Therefore, our strategy for determining which of the two confining methods can achieve the lowest temperature is based on switching adiabatically from DC to ODC, so the entropy is conserved. Then we determine the temperatures T_{dc} and T_{odc} of the DC and ODC systems by equating the entropies

We will consider an experiment in which a *fixed* number N of atoms is loaded into an optical lattice with a DC trap, described by Eq. (3.1) with parameters $t_{ij} = 1$, $W = 0.008$ (as in Ref. [108]). We use $L = 400$ in order to ensure the confinement of the whole gas. Then, we adiabatically switch to the ODC trap by slowly varying t_{ij} and W to $t_{ij} = (i + j + 1)(2L - i - j - 1)/L^2$ with $L = 70$, and $W = 0$ (as in Ref. [111]), keeping N and U the same.

However, in our calculation, it is actually more convenient to control the temperature than the entropy. Thus we consider both DC and ODC systems for a set temperatures T, and measure the corresponding entropies, $S_{dc}(T)$ and $S_{odc}(T)$. Then, knowing the initial temperature T_{dc}, the final temperature T_{odc} can be extracted graphically by imposing the equality, $S_{dc}(T_{dc}) = S_{odc}(T_{odc})$, as described in the next section.

3.3 The Hard-core Case: Exact Analytical Results

The hard-core limit ($U = +\infty$) of the model can be solved analytically. These exact results provide a solid benchmark for our study of the general soft-core case in the next section. We follow here the method used by Rigol [128]. In the hard-core limit, the U term in (3.1) can be dropped if the standard bosonic commutation rules are replaced by $[a_i, a_j] = [a_i^\dagger, a_j^\dagger] = [a_i, a_j^\dagger] = 0$ for $i \neq j$, and $a_i a_i^\dagger + a_i^\dagger a_i = 1$, and $a_i^2 = a_i^{\dagger 2} = 0$. With this algebra, the model (3.1) reduces to

$$\hat{\mathcal{H}} = -\sum_{\langle i,j \rangle} t_{ij} \left(a_i^\dagger a_j + h.c. \right) + W \sum_i (i - L/2)^2 \hat{n}_i, \qquad (3.3)$$

which describes hard-core bosons. By performing a Jordan-Wigner transformation, the hard-core creation and annihilation operators can be mapped onto fermionic creation and annihilation operators, $f_i^\dagger$ and f_i,

$$a_j^\dagger = f_j^\dagger \prod_{q=1}^{j-1} e^{i\pi f_q^\dagger f_q}, \quad a_j = \prod_{q=1}^{j-1} e^{-i\pi f_q^\dagger f_q} f_j, \tag{3.4}$$

which satisfy the usual fermionic anticommutation rules, $\{f_i, f_j\} = \{f_i^\dagger, f_j^\dagger\} = 0$, $\{f_i, f_j^\dagger\} = \delta_{ij}$. This leads to a model that describes free spinless fermions,

$$\hat{\mathcal{H}} = -\sum_{\langle i,j \rangle} t_{ij} \left(f_i^\dagger f_j + h.c. \right) + W \sum_i (i - L/2)^2 \hat{n}_i, \tag{3.5}$$

where $\hat{n}_i = f_i^\dagger f_i$ represents the number of fermions on site i. Because the model (3.5) is a quadratic form of $f_i^\dagger$ and f_i, it can be solved by a simple numerical diagonalization of the $L \times L$ matrix. Denoting by ϵ_k with $k \in [1, L]$ the eigenvalues of this matrix, the partition function (3.2) takes the form

$$\mathcal{Z} = \prod_{k=1}^{L} \left(1 + e^{-\beta(\epsilon_k - \mu)} \right). \tag{3.6}$$

The entropy is defined as $S = -k_B \text{Tr} \, \mathcal{D} \ln \mathcal{D}$ with the density matrix $\mathcal{D} = \frac{1}{\mathcal{Z}} e^{-\beta(\hat{\mathcal{H}} - \mu \hat{\mathcal{N}})}$. Working in a system of units where the Boltzmann constant $k_B = 1$ and using the properties of the density matrix, it follows that $S = \ln \mathcal{Z} + \beta \langle \hat{\mathcal{H}} \rangle - \beta \mu \langle \hat{\mathcal{N}} \rangle$. Substituting $\langle \hat{\mathcal{H}} \rangle - \mu \langle \hat{\mathcal{N}} \rangle = -\frac{\partial}{\partial \beta} \ln \mathcal{Z}$ and using expression (3.6) for $\mathcal{Z}$, the entropy takes the form

$$S(\beta, \mu) = \sum_{k=1}^{L} \left[\ln \left(1 + e^{-\beta(\epsilon_k - \mu)} \right) + \frac{\beta(\epsilon_k - \mu)}{e^{\beta(\epsilon_k - \mu)} + 1} \right]. \tag{3.7}$$

The average number of particles N is obtained by summing the Fermi-Dirac distribution,

$$N(\beta, \mu) = \sum_{k=1}^{L} \frac{1}{e^{\beta(\epsilon_k - \mu)} + 1}. \tag{3.8}$$
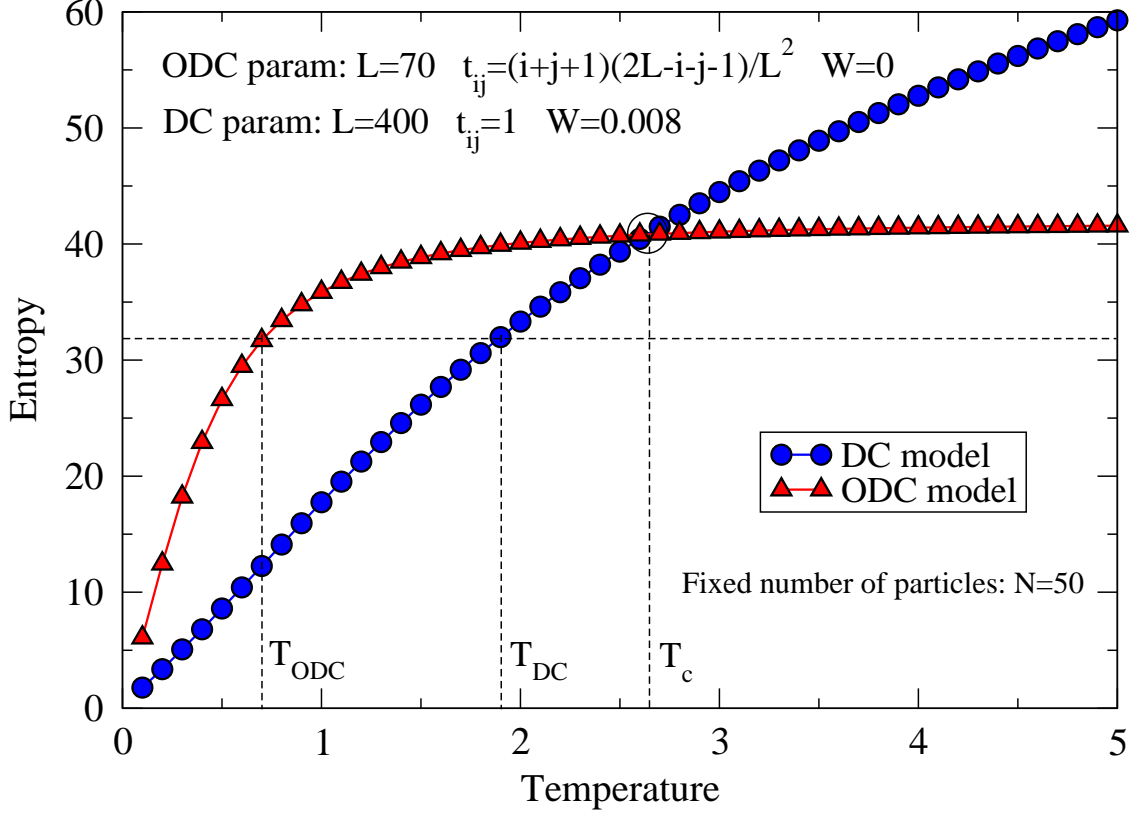
Figure 3.1: The entropy as a function of temperature for 50 hard-core bosons, in the DC case (circles) and in the ODC case (triangles). There exists a critical temperature T_c where the two curves cross. If the initial temperature T_{dc} is below T_c, then the conservation of the entropy when switching adiabatically from DC to ODC implies that the final temperature T_{odc} is lower.

Fig. 3.1 shows the entropy (3.7) as a function of temperature for both DC and ODC cases. The chemical potential μ is adjusted such that the average number of particles (3.8) remains constant ($N = 50$). An interesting feature is that the two curves cross at a temperature T_c, and that below T_c the entropy of the ODC system is greater than the entropy of the DC system. Thus, if the initial temperature T_{dc} is below T_c, then the final temperature T_{odc} is lower when switching adiabatically from DC to ODC.

Next we generalize our discussion by calculating, for a fixed number of particles N, the critical temperature T_c below which the ODC method produces a temperature lower than the DC method when the confinement is switch adiabatically.

In order to determine T_c for given parameters t_{ij}^{dc} and W for the conventional DC system, and t_{ij}^{odc} for the ODC model, one needs to solve for each value of N a system of three coupled non-linear equations,

$$
\begin{cases}
S_{odc}(\beta_c, \mu_{odc}) = S_{dc}(\beta_c, \mu_{dc}) \\
N_{odc}(\beta_c, \mu_{odc}) = N \\
N_{dc}(\beta_c, \mu_{dc}) = N
\end{cases}
\tag{3.9}
$$

where S_{odc} (S_{dc}) is given by Eq. (3.7) and N_{odc} (N_{dc}) is given by Eq. (3.8), with $\mu = \mu_{odc}$ ($\mu = \mu_{dc}$), and $\beta = \beta_c$. The first equation corresponds to the conservation of the entropy when switching from DC to ODC, and the two others correspond to the conservation of the number of particles. Solving this system of equations determines the critical inverse temperature $\beta_c = 1/T_c$, and the chemical potentials μ_{odc} and μ_{dc} that give the desired number of particles N.

For this purpose, we define an *error* function:

$$
\begin{aligned}
\mathcal{E}(\beta_c, \mu_{odc}, \mu_{dc}) \;=\;& (S_{odc}(\beta_c, \mu_{odc}) - S_{dc}(\beta_c, \mu_{dc}))^2 \\
& + (N_{odc}(\beta_c, \mu_{odc}) - N)^2 \\
& + (N_{dc}(\beta_c, \mu_{dc}) - N)^2.
\end{aligned}
\tag{3.10}
$$

By construction, the solution of Eq. (3.9) minimizes this error function. Starting with an initial guess for β_c, μ_{odc}, and μ_{dc}, we calculate the error $\mathcal{E}(\beta_c, \mu_{odc}, \mu_{dc})$ and its gradient $\vec{\nabla}\mathcal{E} = (\partial\mathcal{E}/\partial\beta_c, \partial\mathcal{E}/\partial\mu_{odc}, \partial\mathcal{E}/\partial\mu_{dc})$. Writing the initial guess as a vector, $\vec{r} = (\beta_c, \mu_{odc}, \mu_{dc})$, we perform a correction $\Delta\vec{r}$ by following the opposite direction of the gradient $\vec{\nabla}\mathcal{E}$. Then we iterate until convergence.

Fig. 3.2 shows the critical temperature T_c and the DC isotherms as functions of N. For a given number of particles and an initial temperature $T = T_c(N)$, the ODC and DC systems have the same temperature $T_{odc} = T_{dc}$ when the confinement is switch adiabatically. Below (above) T_c, the ODC system has a temperature T_{odc} that is lower (higher) than the
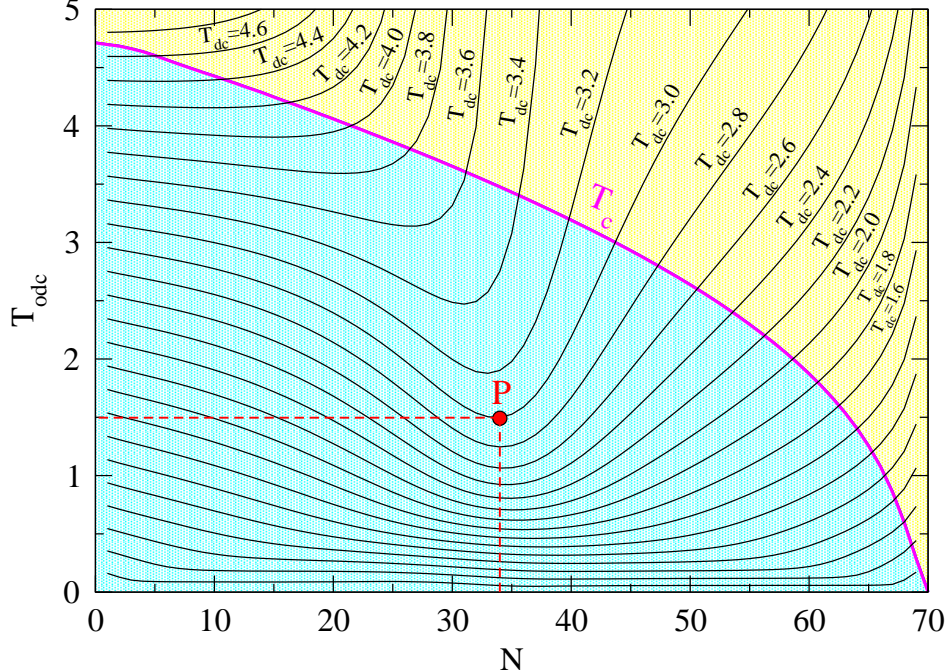
Figure 3.2: The critical temperature T_c and the DC isotherms as functions of the number of particles N. At $T = T_c$, there is no change in temperature when switching adiabatically from DC to ODC. Below T_c (blue region), the ODC method gives a temperature T_{odc} that is lower than the temperature T_{dc} obtained with the DC method. Above T_c (yellow region), it is the DC method that gives the lowest temperature. For example, the point P corresponds to a system with 34 particles, an initial temperature $T_{dc} = 3$, and a final temperature $T_{odc} \approx 1.5$.

temperature T_{dc} of the DC system. The point P illustrates how the figure should be read: For a system with 34 particles and an initial DC temperature $T_{dc} = 3$, the final ODC temperature is $T_{odc} \approx 1.5$. Note that T_c vanishes when N=L=70. The resulting Mott phase found in the ODC case always has lower entropy than the mixed phases found in the DC case. This will be discussed in greater detail in the next section.

3.4   Quantum Monte Carlo Algorithm and Entropy

For the treatment of soft-core interactions, we perform quantum Monte Carlo (QMC) simulations using the Stochastic Green Function (SGF) algorithm [102] with tunable directionality [103]. Although this algorithm was developed for the canonical ensemble, a trivial extension [152] allows us to simulate the grand-canonical ensemble. We propose a new
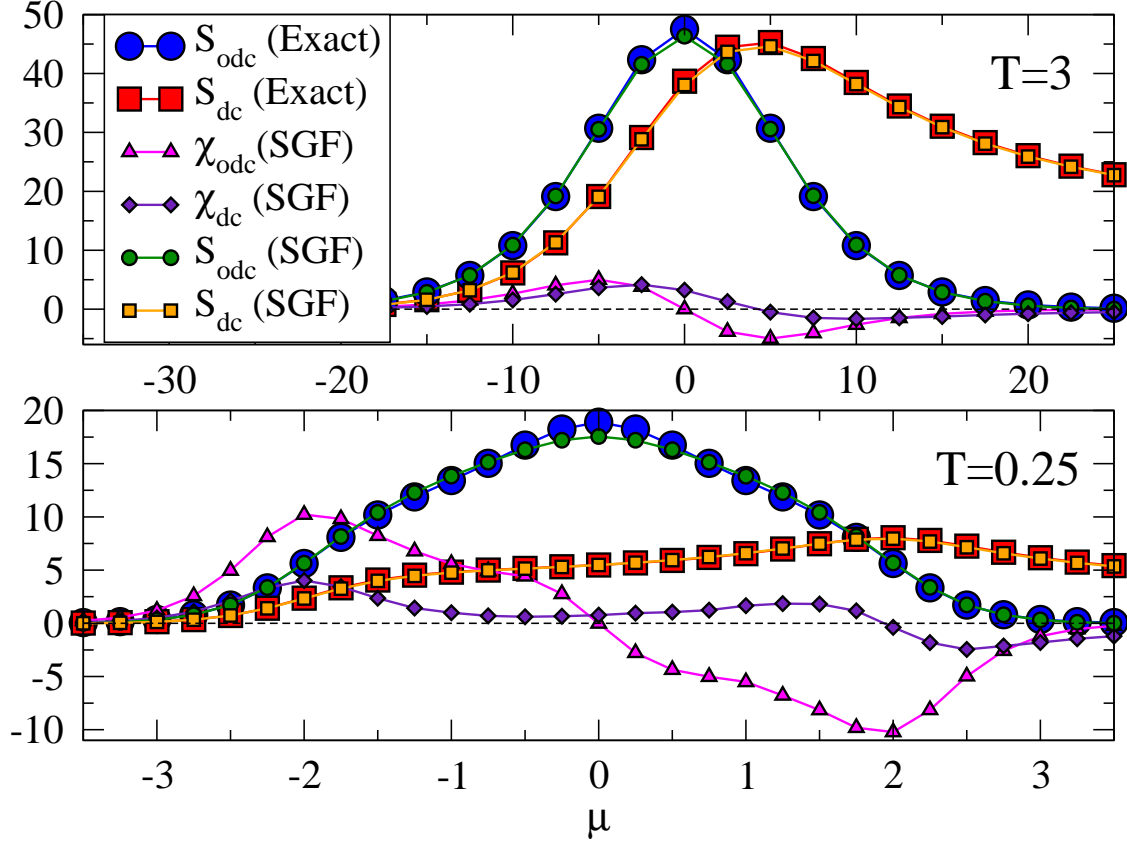
Figure 3.3: The entropy S and the thermal susceptibility χ in the hard-core case. Comparison between results obtained with exact diagonalization using Eq. (3.7) and QMC results with the SGF algorithm and Eq. (3.15). Two different temperatures are considered, $T = 3$ and $T = 0.25$, for both DC and ODC systems.

method to measure the entropy by taking advantage of the grand-canonical ensemble. Our thermodynamic control parameters are the temperature T, the volume V (number of sites L), and the chemical potential μ. Unlike the analytical hard-core case, a direct measurement of the entropy is not possible with a single QMC simulation because the value of $\mathcal{Z}$ is unknown. However it is still possible to evaluate the entropy with a set of QMC simulations. For this purpose, we define the *thermal susceptibility* χ_{th} by the response of the number of particles N to an infinitesimal change of the temperature T as

$$\chi_{th}(T, V, \mu) = \left. \frac{\partial N}{\partial T} \right|_{V,\mu}. \tag{3.11}$$

By substituting $N = \frac{1}{\mathcal{Z}} \text{Tr} \, \hat{\mathcal{N}} e^{-\beta(\hat{\mathcal{H}} - \mu \hat{\mathcal{N}})}$ in expression (3.11), we get an expression for the thermal susceptibility that can be directly measured in our simulations:

$$\chi_{th} = \beta^2 \Big[\langle \hat{\mathcal{N}}(\hat{\mathcal{H}} - \mu \hat{\mathcal{N}}) \rangle - \langle \hat{\mathcal{N}} \rangle \langle (\hat{\mathcal{H}} - \mu \hat{\mathcal{N}}) \rangle \Big] \tag{3.12}$$

Considering the energy $E = \langle \hat{\mathcal{H}} \rangle$ and the associated differential $dE = TdS - PdV + \mu dN$, where the pressure P is defined as $P = -\dfrac{\partial E}{\partial V}\Big|_{S,N}$, and performing a Legendre transformation over the variables S and N, we can define the grand-canonical potential Ω that depends only on our natural variables, $\Omega(T, V, \mu) = E - TS - \mu N = -PV$. Its differential takes the form

$$d\Omega = -SdT - PdV - Nd\mu. \tag{3.13}$$

We can then extract a useful Maxwell relation,

$$\frac{\partial S}{\partial \mu}\Big|_{V,T} = \frac{\partial N}{\partial T}\Big|_{V,\mu}, \tag{3.14}$$

so the entropy can be easily obtained by integrating the thermal susceptibility over the chemical potential and keeping the temperature and the volume constant,

$$S(T, V, \mu) = \int_{\mu_0}^{\mu} \chi_{th}(T, V, \mu') d\mu', \tag{3.15}$$

where μ_0 is the critical value of the chemical potential below which the average number of particles N and the thermal susceptibility χ_{th} are vanishing.

In order to check the reliability of Eq. (3.15), we show on Fig. 3.3 a comparison of the entropy of the hard-core case obtained with the SGF algorithm by integrating the thermal susceptibility (3.12), and the entropy computed with Eq. (3.7). The agreement is good for both DC and ODC systems at high ($T = 3$) and low temperatures ($T = 0.25$).
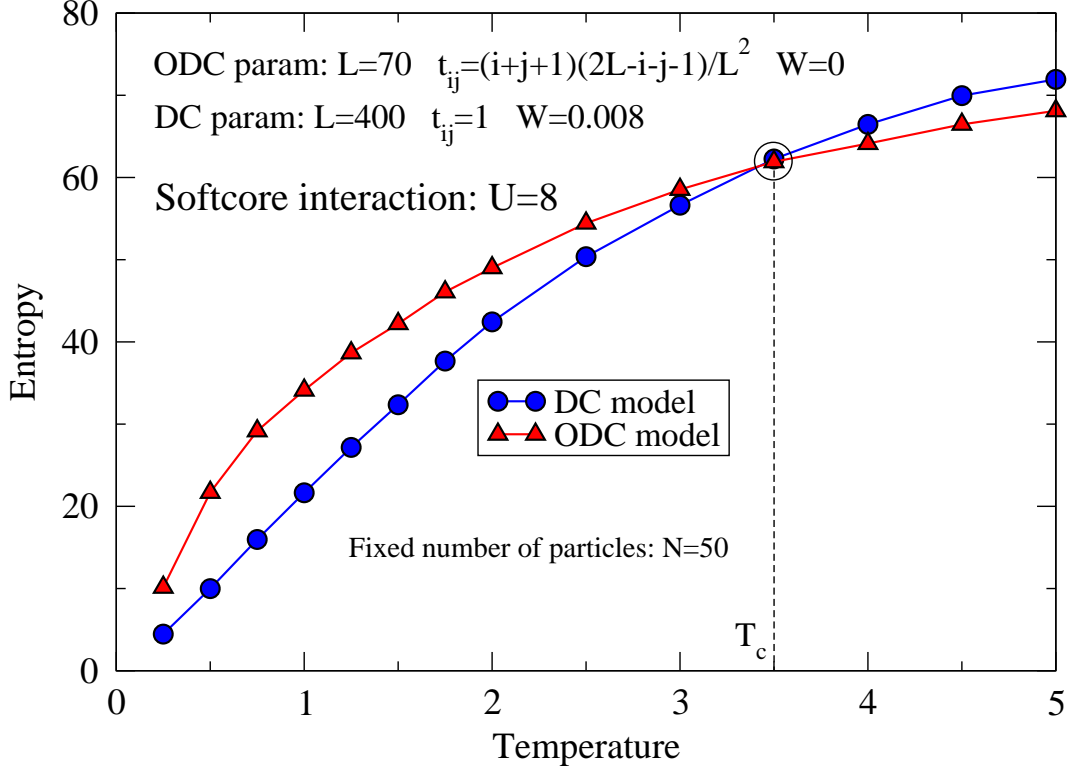
Figure 3.4: The entropy as a function of temperature for 50 soft-core bosons with $U = 8$, in the DC case (circles) and in the ODC case (triangles). As in the hard-core case (Fig.3.1), there exists a critical temperature T_c below which the entropy of the ODC system is higher than the entropy of the DC system, thus making the ODC method more efficient than the DC method for producing low temperatures.

We now release the hard-core constraint and set the onsite repulsion $U = 8$. Fig. 3.4 shows the entropies for the DC and the ODC models as functions of temperature for $N = 50$. The curves differ from the hard-core case only quantitatively, not qualitatively, showing that the method of cooling by switching from DC to ODC still works. Moreover, one notices that the critical temperature $T_c \approx 3.5$ is higher than in the hard-core case ($T_c \approx 2.65$) which makes easier to access the regime where ODC is more efficient than DC.

Further, we extend our soft-core results to different values of the onsite repulsion. Fig. 3.5 shows the entropy for the DC and the ODC models as function of the inverse onsite repulsion $1/U$ for $N = 50$ and $T = 1.0$. The curves show that the entropy of the ODC model is above the one of the DC model for any value of U. Thus, for this filling, the ODC method produce
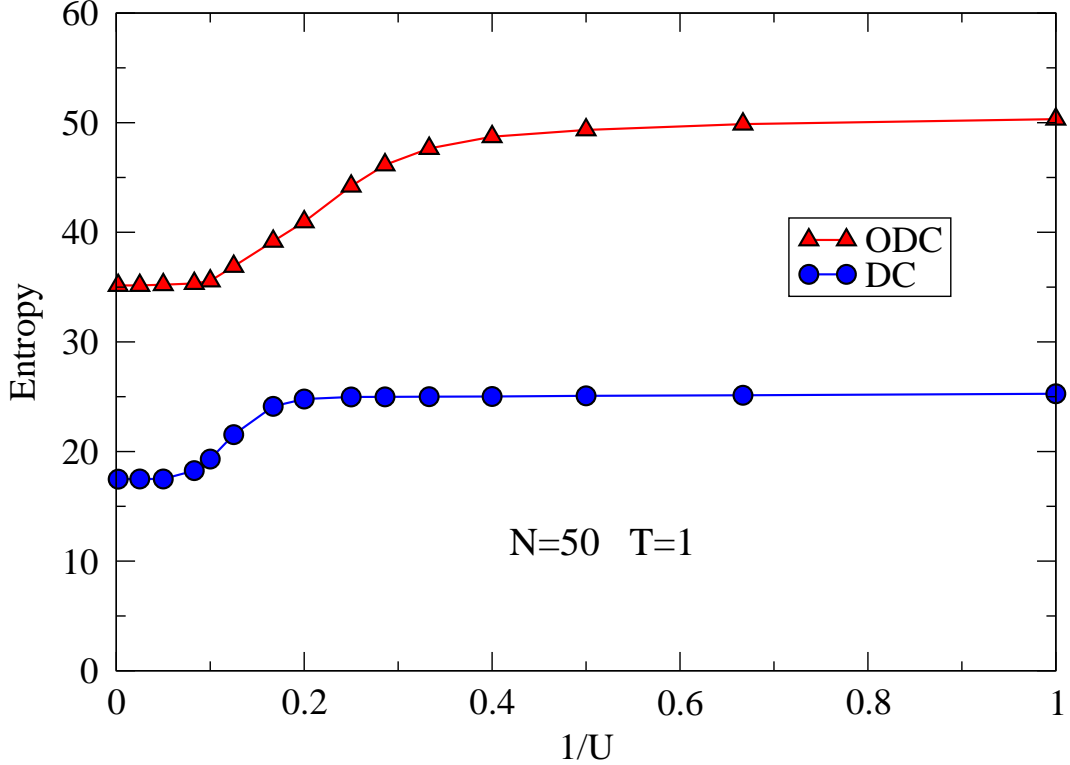
Figure 3.5: The entropy as a function of the inverse onsite interaction $1/U$ for 50 soft-core bosons at $T = 1$, in the DC (circles) and ODC cases (triangles). The entropy of the ODC system remains greater than the entropy of the DC system for any value of the onsite repulsion U, showing that our suggested cooling method works deep into the soft-core case.

temperatures lower than the DC method for any value of the onsite repulsion. When U is large, the results match with those obtained in the preceding section for the hard-core case (Fig. 3.1).

However, the situation is different for $N = 70$ as Fig. 3.6 illustrates. At this integer filling, the entropy of the ODC model, which vanishes in the large U limit, intersects the curve for the DC model. In this regime, the ODC model exhibits a pure Mott phase, hence with zero entropy. However the phase of the DC model has Mott regions coexisting with superfluid regions, so the entropy remains finite. Thus, ODC cannot be used to cool the system in this region.

Concerning the experimental realization of our model, a holographic technique recently developed [130] can be used to build the optical lattice with off-diagonal confinement. Using
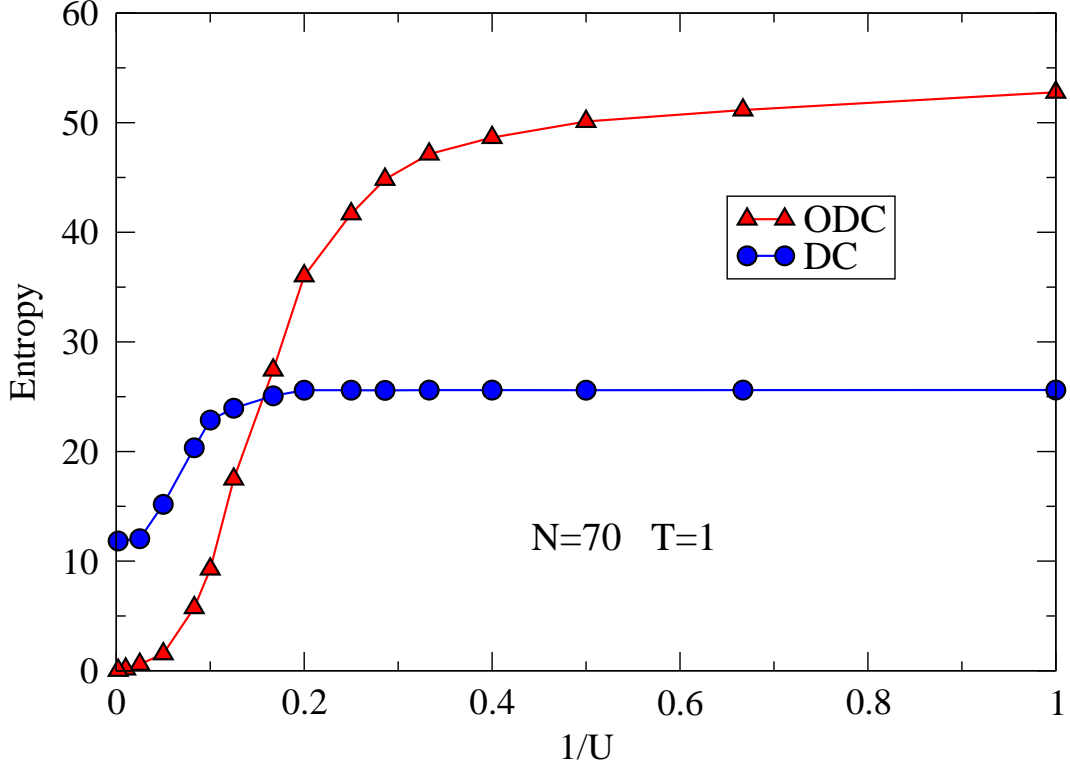
Figure 3.6: The entropy as a function of the inverse onsite interaction $1/U$ for 70 soft-core bosons at $T = 1$, in the DC case (circles) and in the ODC case (triangles). For the ODC case the filling is commensurate and the system forms a pure Mott phase that cannot carry any entropy. Thus ODC cannot be used as a cooling method for commensurate fillings.

this method, an off-diagonal trap can be superposed to an existing diagonal trap. Then the diagonal trap can be turned off. The switching between the two traps can be in principle very fast, however the technical details of how this will work go beyond the scope of the present manuscript and must be developed by experimentalists. Nevertheless, a qualitative analysis reveals that three time scales must be considered. The time scale τ_m of the model system or roughly $\tau_m = 1/t$ (in units where $\hbar = 1$), the time scale of the experiment τ_e, and the time scale τ_c which describes the coupling of the model system to its environment which includes the effects of the laser heating, evaporation, etc. In our proposal, it is important that the trap is adiabatically switch on the experimental time scale, but not on the time scale which describes the coupling of the trap to its environment, so that $\tau_m \ll \tau_e \ll \tau_c$.

3.5   Conclusion

In this manuscript we propose that the adiabatic switch from the DC to the ODC method can produce lower temperatures for a wide range of initial temperatures and system parameters. In the hard-core limit, we determine the critical temperature T_c for which the two methods have the same entropy. Below (above) T_c and at constant entropy, the ODC method leads to temperatures that are lower (higher) than with the DC method. In order to extend our results to the soft-core case, we propose a simple method for evaluating the entropy with QMC, by measuring the thermal susceptibility χ_{th} in the grand-canonical ensemble and integrating it over the chemical potential μ. Then we make use of the SGF algorithm [102] with tunable directionality [103], and show that the soft-core results are qualitatively the same as in the hard-core case.

Chapter 4
Bose-Hubbard Model with Tunable Weak Links

In this chapter, I present our study of interacting bosons with tunable weak links in the one dimensional Bose-Hubbard model. Motivated by recent experiments on toroidal Bose-Einstein condensates in all-optical traps with tunable weak links, we study the one-dimensional Bose-Hubbard model on a ring-shaped lattice with a small region of weak hopping integrals using quantum Monte Carlo simulations. Besides the usual Mott insulating and superfluid phases, we find a novel phase which is compressible but non superfluid with a local Mott region. This new *local Mott* phase extends in a large region of the phase diagram. These results suggest that the insulating and conducting phases can be tuned by a local parameter which may provide a new insight to the design of atomtronic devices.

This work was done in collaboration with V. G. Rousseau, Ka-Ming Tam, M. Jarrell, and J. Moreno. The material presented in this chapter has been published in Physical Review A [113]. In this project, I wrote a quantum Monte Carlo (QMC) C++ code and an exact diagonalization C++ code that simulate the model studied, performed QMC simulations on supercomputers (XSEDE, HPC@LSU and LONI), and analyzed the data.

Kalani Hettiarachchilage, Valéry G. Rousseau, Ka-Ming Tam, Mark Jarrell, and Juana Moreno, *Phase diagram of the Bose-Hubbard model on a ring-shaped lattice with tunable weak links*, Phys. Rev. A 87, 051607 (2013).

4.1 Introduction

Cold atom experiments utilizing an optical lattice provide an excellent testbed for quantum many body problems which were previously inaccessible in conventional materials. A remarkable achievement is the realization of the Bose-Hubbard (BH) model using ultracold atoms on optical lattices [17,18] with the addition of a confining potential that results in the "wedding cake" structure [108]. Over the last two decades, a considerable amount of work has been devoted to understand the ground state phase diagram of the BH model and its variants [37,86–88,106,107]. In general, the model contains a superfluid (SF) phase at incommensurate fillings and a Mott insulating (MI) phase at commensurate fillings and strong coupling. The SF phase is gapless, whereas the MI phase is characterized by the existence of an energy gap for creating a particle-hole pair. As the density is changed or the interaction strength is varied, the BH model can be tuned from the MI to the SF. Tuning between insulating and conducting phases by controlling the external parameters provides a tantalizing opportunity of creating analogs to electronic devices and circuits by using ultra cold atoms in optical lattices, which have been recently defined as 'atomtronics' [109,114]. The conventional electronic system is based on the electron charge, whereas the atomtronic system can use neutral atoms which are either bosons or fermions, moreover the optical lattice is better controlled. Based on this unique property, it has been suggested that these atomtronic systems may be useful in quantum computing [19]. Some theoretical models have already been proposed for atomtronic devices such as batteries, wires, diodes, and transistors [19–21,97,115–117].

A recent advance on optical lattices is the realization of confining potentials with toroidal shapes by using the intersection of two different red-detuned laser beams [78,109]. The versatility of this technique allows the creation of ring-shaped lattices by superimposing an optical lattice on a toroidal confining potential, which is a realization of a quasi one-dimensional lattice with periodic boundary conditions. Remarkably, it is possible to control the *local* hopping parameter in a region of the ring by applying a magnetic field and an

additional laser beam [78]. This opens up the new possibility that the different phases in a boson system not only can be tuned by a global parameter, such as the coupling strength or chemical potential, but also by a *local* parameter, such as the tunneling strength of a small region of the entire lattice. It has been suggested that this property can be utilized as an alternative realization of atomtronics [78].

In this project, by using quantum Monte Carlo (QMC), we show that introducing weak links in a ring lattice can produce a local Mott (LM) phase in addition to the usual MI and SF phases present in the homogeneous BH model. Zero temperature local incompressible MI behavior was shown in a one dimensional system of interacting bosons in a confining potential [108]. Our non-confined model exhibits a LM phase which is gapless and non-SF, and a region of LM insulator which exhibits incompressible MI behavior. This is an important result which suggested that by controlling the local tunneling strength the system can be tuned between a SF phase and a MI phase thorough a non-SF LM phase. This provides theoretical support that atomtronic switches can be implemented by tuning certain local parameters in a quasi one-dimensional system.

4.2   Model and Method

We consider a bosonic system on a torus-shaped lattice, where the section of the torus is sufficiently small compared to the primary radius so the physics can be reduced to a one-dimensional lattice with periodic boundary conditions. The Hamiltonian takes the form

$$\hat{\mathcal{H}} = -t \sum_{\langle i,j \rangle} w_{ij} \left(a_i^\dagger a_j + H.c. \right) + \frac{U}{2} \sum_{i=1}^{L} \hat{n}_i (\hat{n}_i - 1), \tag{4.1}$$

where L is the number of lattice sites. The creation and annihilation operators $a_i^\dagger$ and a_i satisfy bosonic commutation rules, $[a_i, a_j] = [a_i^\dagger, a_j^\dagger] = 0$, $[a_i, a_j^\dagger] = \delta_{ij}$, and $\hat{n}_i = a_i^\dagger a_i$ is the operator that measures the number of bosons on site i. The parameter t is the global magnitude of the hopping integral. In this paper, we use $t = 1$ to set the energy scale.
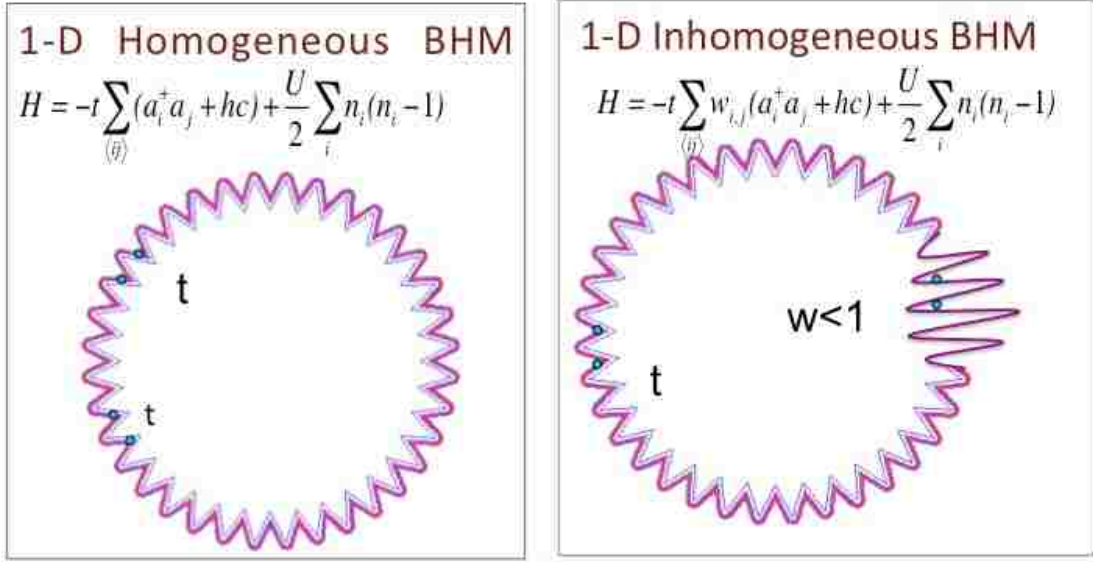
Figure 4.1: One-dimensional homogeneous bosonic Hubbard model (BH) with periodic boundary condition can show as a ring shape lattice with the homogeneous hopping integral t. The inhomogeneous BH with weak links can show as a ring shape lattice with two hopping integrals t and less than t.

The sum $\sum_{\langle i,j \rangle}$ runs over all distinct pairs of first neighboring sites i and j, and $w_{ij} \in [0;1]$ determines the weakness of the hopping integral between i and j (see Fig. 4.1). In the following we consider a system with M consecutive weak links for which $w_{ij} = J/t$, where $J \in [0;t]$ is a control parameter, and $L - M$ strong links with $w_{ij} = 1$. We restrict our study to the case with 10% of weak links ($M = L/10$). The parameter U determines the strength of the on-site interaction.

In order to solve this model, we perform exact QMC in both canonical and grand-canonical ensembles by using the Stochastic Green Function algorithm [102, 103] with global space-time updates [104]. In the canonical ensemble, the number of particles N is a parameter and remains constant during the simulation. The chemical potential μ is measured at zero temperature by the finite energy difference $\mu(N) = E(N+1) - E(N)$. In the grand-canonical ensemble, the number of particles is given by the quantum average of the operator $\hat{N} = \sum_i \hat{n}_i$,
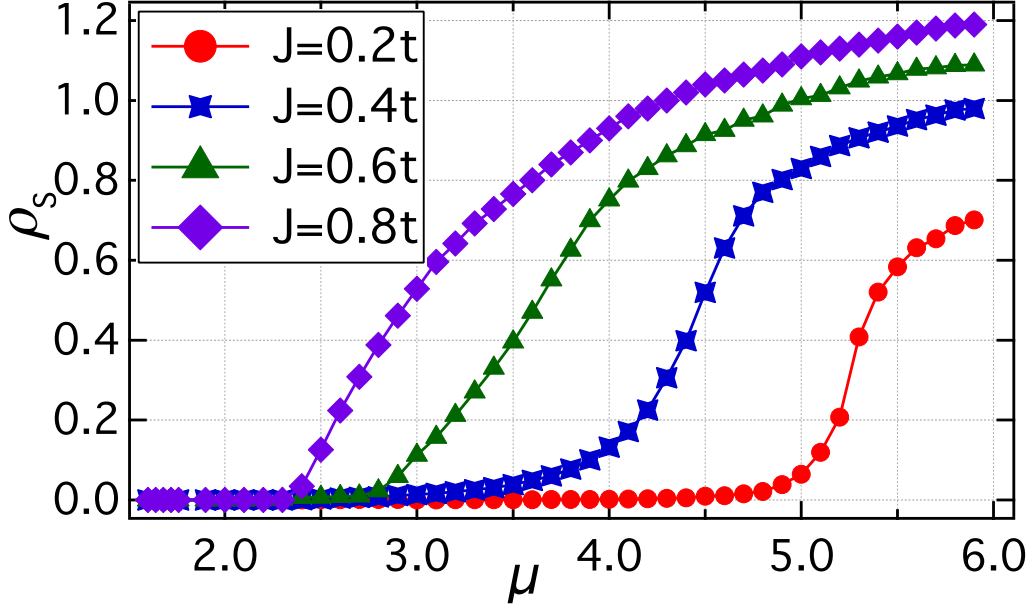
Figure 4.2: The Superfluid density ρ_s as a function of the chemical potential μ for $L = 50$ and $U = 8$ in the ground state. The figure shows results for different values of the weak hopping integrals, $J = 0.2t$ (circles), $J = 0.4t$ (stars), $J = 0.6t$ (triangles) and $J = 0.8t$ (square).

and is controlled by adding to the Hamiltonian (3.1) the term $-\mu \hat{N}$ where μ is a control parameter. We use an inverse temperature $\beta = L/t$ in order to capture the ground-state properties.

4.3 Superfluid Density and Compressibility

For the uniform system, $J = t$, only two phases are present (MI or SF). The MI phase occurs at commensurate fillings and large onsite repulsion U, and is characterized by a vanishing compressibility, $\kappa = \frac{\partial \rho}{\partial \mu}$, where $\rho = N/L$. The SF phase is detected by measuring the superfluid density, ρ_s, given by the response of the system to a phase twist of the wave function at the boundaries of the system.
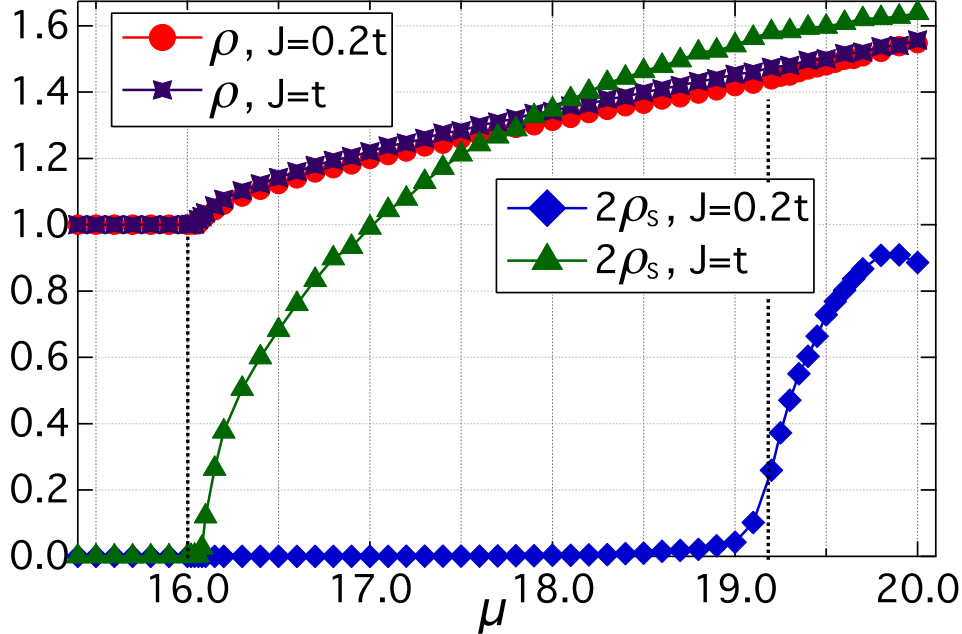
Figure 4.3: The density ρ and the superfluid density ρ_s as functions of the chemical potential μ for the homogeneous system $(J = t)$ and an inhomogeneous system $(J = 0.2t)$, for $L = 50$ and $U = 20$.

In our quantum Monte Carlo simulations, it is convenient to relate this superfluid density to the fluctuations of the winding number, W, via Pollock and Ceperley's formula [118],

$$\rho_s = \frac{\langle W^2 \rangle L}{2t\beta}. \tag{4.2}$$

We have checked analytically and with exact diagonalization that the above formula remains valid for the non-uniform system, $J < t$.

In the following, we show that there exists a range of parameters for the non-uniform system for which we observe a vanishing superfluid density and a finite compressibility at incommensurate fillings. Fig. 4.2 shows the superfluid density ρ_s as a function of the chemical potential μ for $L = 50$ and $U = 8$. Here we use grand-canonical simulations for different weak link hoppings J. We can clearly see that the region with vanishing superfluid density expands over a large range of chemical potentials μ when the strength of the weak links is lowered.
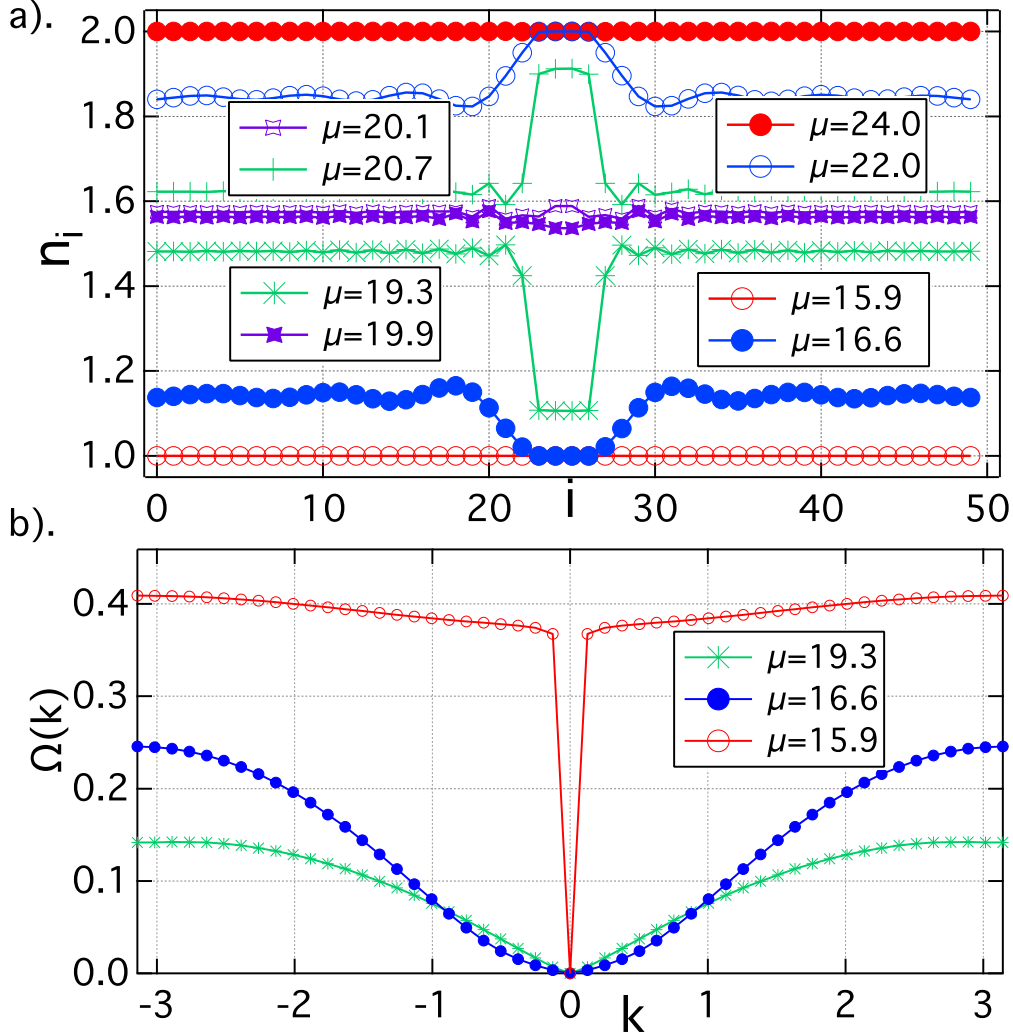
Figure 4.4: The local density (top panel) and the excitation spectrum (bottom panel) for $L = 50$ and $U = 20$, in the ground state. Top panel: The local density n_i as a function of the site index i for different values of the chemical potential μ. Bottom panel: The low energy excitation spectrum $\Omega(k)$ in the three regions of the phase diagram: SF, LM and MI.

Fig. 4.3 shows the density ρ and the superfluid density ρ_s as functions of the chemical potential μ, for both homogeneous $(J = t)$ and inhomogeneous $(J = 0.2t)$ systems. We can see that a Mott plateau at $\rho = 1$ exists until $\mu = 16.1$ with a vanishing superfluid density ρ_s and compressibility κ, for both systems. For $\mu > 16.1$, the density ρ starts the increase and the compressibility κ is finite. As it is well known, the superfluid density ρ_s of the homogeneous system is non-zero as soon as the density is no longer an integer. However, for

the inhomogeneous system, the superfluid density remains zero until $\mu \approx 19.1$. Thus there exists a finite range of values for the chemical potential for which the superfluid density is vanishing but the compressibility is finite. Therefore, as the chemical potential is increased, the inhomogeneous system undergoes a phase transition from a MI phase to a new phase, then to a SF phase.

4.4   Properties of Phases

We investigate the intermediate phase first by analyzing the local density of the lattice. The local density in the homogeneous model is uniform, whether the system is in the MI or SF phase. For the inhomogeneous model, we have phases with a non-uniform local density, as shown in Fig. 4.4a. We insert 10% of the weak links in the middle of the lattice. In the MI region, the local density n_i throughout the entire lattice is uniform and sticks to integer values ($n_i = 1$ for the first Mott lobe, $n_i = 2$ for the second one, etc).

When additional particles or holes are added to the lattice the weak link region keeps its integer density (see Fig. 4.4a). Outside the weak link region, the local density shows an oscillatory behavior. These two observations indicate that the additional particles do not affect the MI character of the weak link region until the number of additional particles or holes is beyond a critical density. For a one-dimensional system, the superfluid density or the winding is zero when part of the system is locally Mott. As a result we identify this locally integer-density region as a local Mott (LM) phase. The weak link provides a fixed boundary condition for the density profile, the additional particles or holes accumulate outside. Then, the region with $J = t$ can be effectively described by the hard-core boson model with $L - L_{weak}$ number of sites. For a one dimensional system, the hard-core boson can be written in terms of spinless fermions using the Jordan-Wigner transformation, [119] and the oscillation of the local density can then be explained by Friedel oscillations, [120] where $n_i \sim cos(k_F x_i)$, where k_F is the Fermi wavevector given by the particle density. This explanation is corroborated by the numerical data which show that the cycle of the oscillation
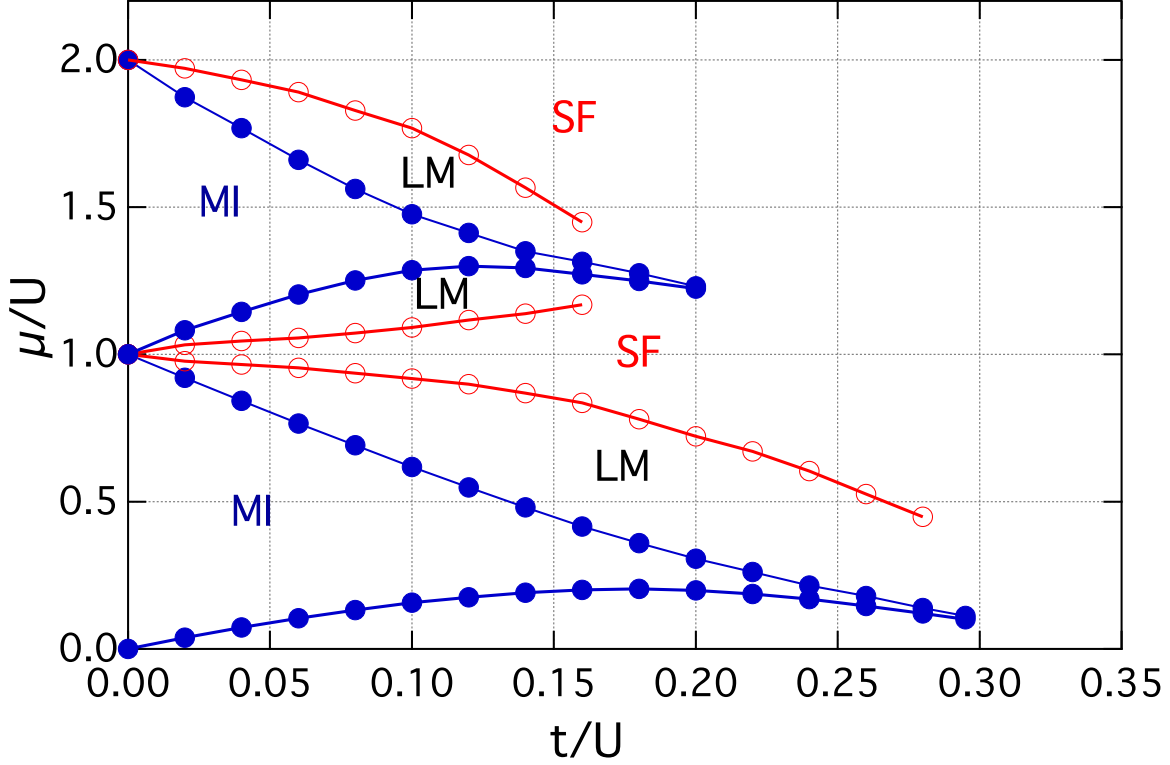
Figure 4.5: The ground state phase diagram of the inhomogeneous system ($J = 0.2t$) in the $(\mu/U, t/U)$ plane. The lines with solid circles show the first and the second Mott lobes, and the lines with open circles show the boundaries between the LM and the SF regions.

of the local density is approximately given by $1/|n - 1.0|$ for $\mu = 16.6$ and $1/|n - 2.0|$ for $\mu = 22$ (see Fig. 4.4a).

When adding more particles beyond the critical density, the local density at the weak link shifts away from integer values. This suggests that the LM insulating region is destroyed. Thus it opens the path for the flow, and we find that the superfluid density becomes finite when this happens.

We study the dynamics of the model by evaluating the low energy excitation spectrum. Using the Feynman single-mode approximation, the low energy excitation spectrum $\Omega(k)$ can be written as [121]

$$\Omega(k) = \frac{E_k}{S(k)} \tag{4.3}$$

where,

$$E_k = \frac{-t}{L}(\cos k - 1)\langle\Psi_0|\sum_{i=1}^{L}(a_i^\dagger a_{i+1} + a_{i+1}^\dagger a_i)|\Psi_0\rangle, \tag{4.4}$$

$|\Psi_0\rangle$ is the ground state, and $S(k)$ is the static structure factor.

Fig. 4.4b displays the low energy excitation spectrum throughout the reciprocal lattice space. In the MI region it shows a gap near zero wave vector, whereas it has a linear dependence for the SF phase. The linear behavior is expected in the SF region due to the gapless Goldstone mode. In the LM region the low energy spectrum shows a parabolic behavior, as expected for disordered free-particles. Since the LM does not follow a linear behavior near $k = 0$, no signal of super-flow exists in the LM region.

4.5   Ground State Phase Diagram

The MI phase is characterized by an integer local density and the existence of a finite gap for single particle excitations. At zero temperature, the gap can be easily obtained in the canonical ensemble. We define the gap as $\Delta = \mu_+ - \mu_-$, where μ_- and μ_+ are the minimum and maximum values of the chemical potential for which the MI phase exists. By definition, $\mu_+ = E(N+1) - E(N)$ and $\mu_- = E(N) - E(N-1)$, where N is the number of particles in the MI phase. The functions $\mu_-(t, J, U)$ and $\mu_+(t, J, U)$ determine the boundaries between the MI and LM regions. Since the total density remains unchanged for $\mu \in [\mu_-; \mu_+]$, the compressibility κ is vanishing in the MI region.

We determine the phase boundary between the LM and SF regions by using the grand canonical simulations and scanning over the chemical potential, as in Fig. 4.3. The critical value μ_c of the chemical potential where the superfluid density becomes non-zero depends on the size of the system, L, and converges to a finite value in the thermodynamic limit. As the size increases, the curve displaying the superfluid density becomes sharper and sharper.

Since we work with a fixed large size, $L = 50$, we define μ_c by the value of the chemical potential that corresponds to the maximum slope for the superfluid density curve. The curve $\mu_c(t, J, U)$ determines the boundary between the LM and SF phases.
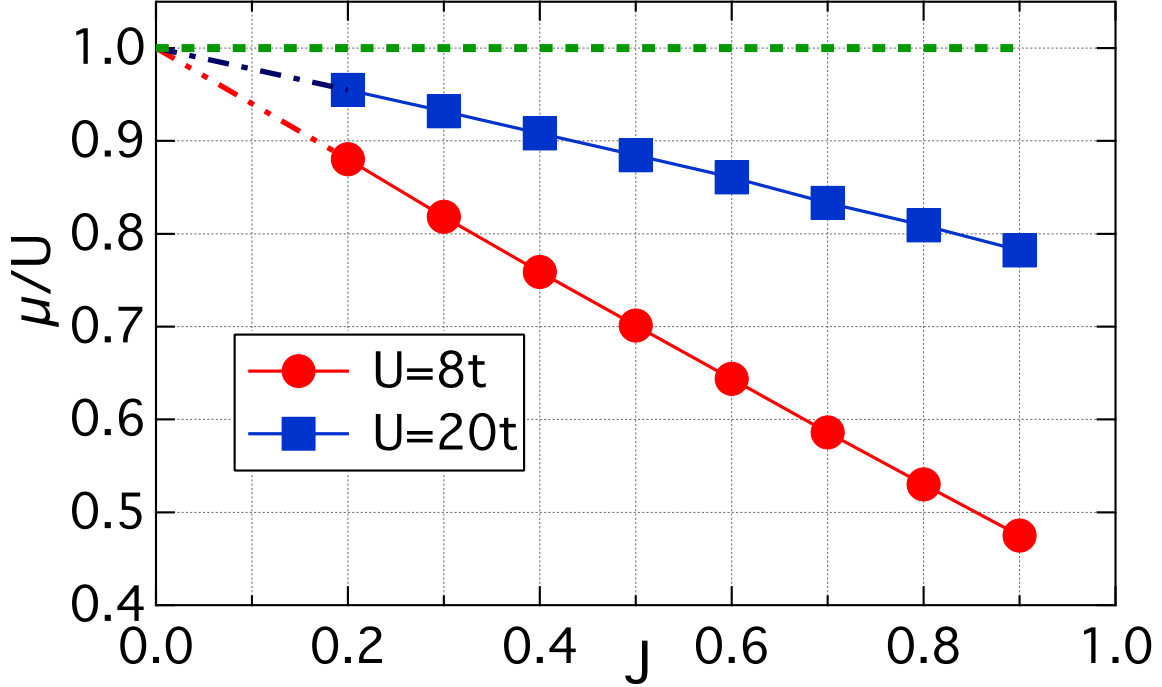
Figure 4.6: The critical value of the chemical potential μ_c between the LM and SF regions, as a function of the weak link hoping J, for $U = 8$ and $U = 20$. The variation with J is quasi-linear.

In our simulations the density varies continuously as a function of the chemical potential. This suggests that the transitions from MI to LM and from LM to SF are continuous, as it is the case for the homogeneous model [90–92]. We show in Fig. 4.5 the ground state phase diagram for $J = 0.2t$ in the $(\mu/U, t/U)$ plane. The Mott lobes that are present in the homogeneous model are weakly deformed by the presence of the LM phase. The phase boundaries near the tip of the Mott lobes are difficult to estimate due to the very small LM region.

We now investigate the variation of the phase boundary between the LM and SF regions as a function of weak link hopping J, Fig. 4.6. For a fixed value of the interaction U, the phase boundary lifts up linearly when decreasing the hopping J in the weak link reducing the size of the SF region in the phase diagram. In the limit $J = 0$ the curve extrapolates to $\mu/U = 1$, and the SF region completely disappears since the system is no longer periodic.

4.6 Conclusion

In this study, we propose that a superconducting ring with weak links might display a new phase which is gapless, compressible, and non-superfluid, with local Mott insulating behavior. This phase does not exist in the homogeneous Bose-Hubbard model. We expect that in the thermodynamic limit, the weak link acts effectively as a domain wall which suppresses the superfluid. While a thorough characterization of the phases and the critical properties of the model will require an analysis of the inhomogeneous Luttinger liquid coupled to a lattice, which is an interesting challenging topic by itself [133–136], we hope our work motivate further study in this direction. Perhaps the most important aspect of the present study is to understand the mechanism of controlling superfluid flow by local perturbation on a finite size system, which is directly related to atomtronic. In the experiment by Raman et al., a toroidal condensate is created with a smooth trapping potential [78]. If the experiment can be repeated by superimposing a lattice on top of the toroidal potential, our model could be directly studied experimentally. Our results have direct implications for atomtronic devices [19, 20]. For example, if the chemical potential μ, the weak link hopping J, and the interaction U/t are tuned so that only the link is a Mott insulator, then a gate above the link can be used to switch the conductivity of the link on and off. The non-linearity of the switching can be tuned by adjusting the link width and hoping J/t. Complex circuits with highly non-linear behavior may be constructed by a series of such switches.

Chapter 5
Two Species Bosonic Hubbard Model

In this chapter, I present our study of the two-dimensional two-species hardcore bosonic Hubbard model away from half filling using Quantum Monte Carlo. The model includes a repulsive interspecies interaction and different nearest-neighbor hopping terms for the two species. By changing the doping, we find a total of five distinct phases, including a normal liquid phase at higher temperature and four different phases at lower temperature. We find an anti-ferromagnetically ordered Mott insulator and a region of coexistent anti-ferromagnetic and superfluid phases near half filling. Further away from half filling, the phase diagram displays a superfluid phase and a novel phase inside the superfluid region at even lower temperatures. In this novel *ferromagnetic phase separated* region, the heavy species has Mott behavior with integer filling, while the lighter species shows phase separated Mott and superfluid behaviors. The entropy of the heavy species is squeezed out into the light species allowing the formation of a Mott phase with high global entropy. This mechanism may provide a new avenue to obtain a polarized Mott insulator in cold atom experiments.

This work was done in collaboration with V. G. Rousseau, Ka-Ming Tam, M. Jarrell, and J. Moreno. The material presented in this chapter has been submitted for publication in Physical Review Letter [131]. In this project, I wrote a quantum Monte Carlo (QMC) C++ code that simulates the model studied, performed QMC simulations on supercomputers (XSEDE, HPC@LSU and LONI), and analyzed the data.

Kalani Hettiarachchilage, Valéry G. Rousseau, Ka-Ming Tam, Mark Jarrell, and Juana Moreno, *Complex phases in the two species bosonic Hubbard Model*, arXiv:1212.4478 (2013).

5.1 Introduction

Cold atoms experiments [18] have become a playground for realizations of the Hubbard [37, 138] and other strongly correlated model Hamiltonians, since model parameters can be tuned using laser and magnetic fields [48, 49]. Recently, there is an increasing interest in studies of mixtures of atoms [38–44] due to the complexity associated with multiple species and the possibility of discovering novel phases. The experimental study of the ^{84}Rb-^{41}K, ^{6}Li-^{40}K and different alkaline earth mixtures in an optical lattice [45–47] have motivated theoretical studies of the Hubbard model with two species with different masses [83, 141–145]. These studies reveal a rich phase diagram at half-filling. Experimental studies of the two species Bose-Hubbard shows that the massive species exhibits Mott while the other shows superfluid behavior [45]. Since the experiment can control the carrier concentration, we explore the doping dependence of the model to find complex phases and exotic phenomena [1–6,8–13,137] such as high-T_c [139] superconductivity.

While experimental controllability is a remarkable aspect of atomic systems, the major goal of simulating quantum magnetism still remains a challenge. The main obstacle is reaching the low entropy and temperature required to observe magnetically ordered or Mott insulating phases. Various methods have been suggested in the last decade or so [146–148]. A recent proposal by Ho and Zhou suggests that the entropy of a Fermi gas can be squeezed into a surrounding Bose-Einstein condensed gas, which acts as a heat reservoir [149]. These light particles are then evaporated, leaving behind a low-entropy Fermi gas. In this letter, we show that the two species bosonic Hubbard model with a mass imbalance at *finite* doping exhibits a novel ferromagnetic phase separated state, in addition to superfluid and antiferromagnetic phases. This novel state has entropy similar to the superfluid indicating that it should have similar experimental accessibility.

Furthermore, this novel state exhibits the entropy squeezing phenomenon in which the heavy particles form a Mott insulating phase, while the light particles form a superfluid phase that act as a heat reservoir to absorb entropy. We also study the phase diagram of this two species bosonic Hubbard model as a function of temperature and doping.

5.2   Model and Method

Our study is based on the two-species Hubbard model with hard-core bosons a and b confined to a two-dimensional lattice. ensemble in L-sites lattice. The Hamiltonian takes the form:

$$\hat{\mathcal{H}} = -\sum_{\langle i,j \rangle} t_a \left(a_i^\dagger a_j + h.c. \right) - \sum_{\langle i,j \rangle} t_b \left(b_i^\dagger b_j + h.c. \right) + \sum_i U^{ab} n_i^a n_i^b \tag{5.1}$$

where $a_i^\dagger$ ($b_i^\dagger$) and a_i (b_i) are the creation and annihilation operators, respectively, of hard-core bosons a (b), with number operators $n_i^a = a_i^\dagger a_i$, $n_i^b = b_i^\dagger b_i$. The sum $\sum_{\langle i,j \rangle}$ runs over all distinct pairs of first neighboring sites i and j, $t_a(t_b)$ is the hopping integral between i and j sites for species a (b), and U^{ab} is the strength of the interspecies repulsion. In the hard-core limit, the creation and annihilation operators satisfy commutation rules on different sites and anti-commutation rules on identical sites.

We perform quantum Monte Carlo simulations using the stochastic green function algorithm [102, 103] with global space-time updates [104] for the canonical ensemble on $L \times L$ lattices. We use an inverse temperature $\beta = 8L$ to capture the ground state properties. Our results at half-filling reproduce the phase diagram of Ref. [83]. We focus on the unpolarized phase diagram, so our total density is $\rho = N/L$ with $N = N_a + N_b = 2N_a$, with N_a and N_b the number of heavy a and light b particles, respectively. We restrict our simulation to the following parameters corresponding to the strongly AF region at half filling: $t_a = 0.08\,t$, $t_b = t$, and $U^{ab} = 6t$, where $t = 1$.
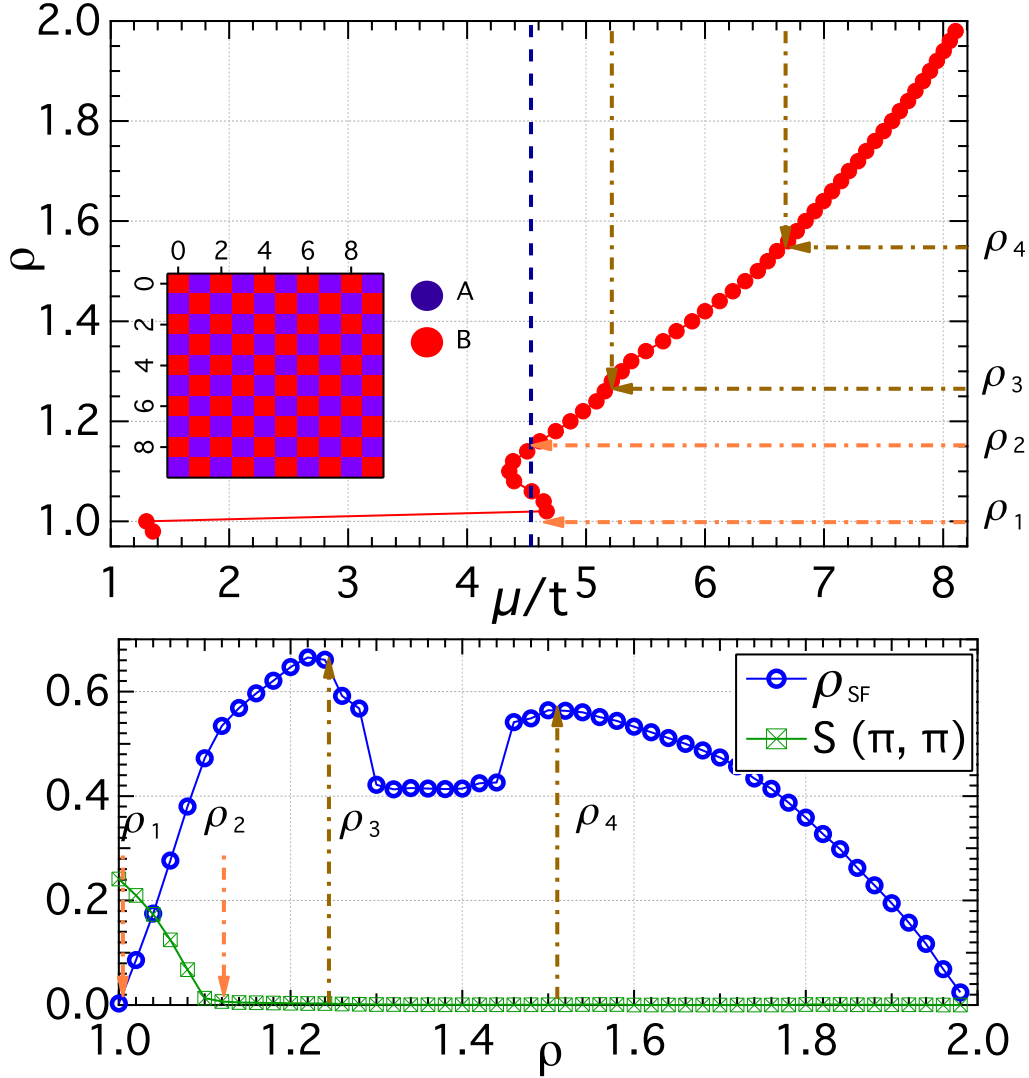
Figure 5.1: (Color online) Top panel: The average density, $\rho = N/L$ as a function of the chemical potential, μ. The vertical blue dashed line shows the Maxwell construction between ρ_1 and ρ_2. The brown dotted-dashed lines show different phase boundaries at ρ_3 and ρ_4 as discussed in the text. The inset shows a snapshot of the density profile at half filling, $\rho = \rho_1 = 1$, with the blue (red) squares indicating $\langle n_i^a \rangle = 1$ ($\langle n_i^b \rangle = 1$). Bottom panel: The superfluid density (blue circles) and the staggered structure factor (green squares) as a function of ρ. The dot-dashed lines show different phase boundaries. All data are for $L = 10$, $\beta = 80$, $t_a = 0.08$, $t_b = 1.00$ and $U^{ab} = 6$. Error bars are smaller than symbol sizes.

5.3 Superfluid Density and Average Density

Fig. 5.1 displays signatures of ordering. To look for phase separation and Mott states, we calculate the chemical potential by adding one a and one b particle to the system as $\mu = (E(N+2)-E(N))/2$. The superfluid (SF) phase is detected by measuring the superfluid density, ρ_{SF}, using the fluctuations of the winding number, W, via Pollock and Ceperley's formula [118]. The AF phase is characterized by a finite density-density static structure factor:

$$S(\vec{k}) = \frac{1}{L^2} \sum_{k,l} exp[i\vec{k} \cdot (\vec{r}_k - \vec{r}_l)] \langle n_k^{(a,b)} n_l^{(a,b)} \rangle. \tag{5.2}$$

We find an AF phase at half filling $\rho_1 = 1$. It is characterized by a vanishing compressibility, $\kappa = \partial\rho/\partial\mu$ (top panel), a finite static staggered structure factor (bottom panel), as well as AF ordering as shown in a snapshot of the density profile (inset of the top panel). Near half filling, $\rho = N/L$ vs. μ displays a first-order phase transition between ρ_1 and $\rho_2 \sim 1.16$. The instability is characterized by a region of negative slope. These two phases with densities ρ_1 and ρ_2 coexist for any density value between the two end points. Since, in this region the system displays finite values of $S(\pi, \pi)$ and ρ_{SF} we conclude that the AF and SF phases coexist for any $\rho_1 < \rho < \rho_2$. A homogeneous SF state exists between ρ_2 and $\rho_3 \sim 1.25$ identified by measuring the superfluid density ρ_{SF}. At ρ_3 the superfluid density displays a decrease and the ρ versus μ plot shows a small bump. Another small feature is displayed in the top panel at $\rho_4 \sim 1.52$. Finally, the homogeneous SF phase continues until full filling. Next, we investigate the unexpected lowering of the superfluid density between ρ_3 and ρ_4.

5.4 Density Profiles

Fig. 4.4 shows snapshots of the average local density of both species for $\rho_3 < \rho = 1.44 < \rho_4$. Simulations with both open and periodic boundary conditions show clear evidence of ferromagnetic phase separation into regions with polarizations $\langle n_i^a - n_i^b \rangle$ of opposite sign.
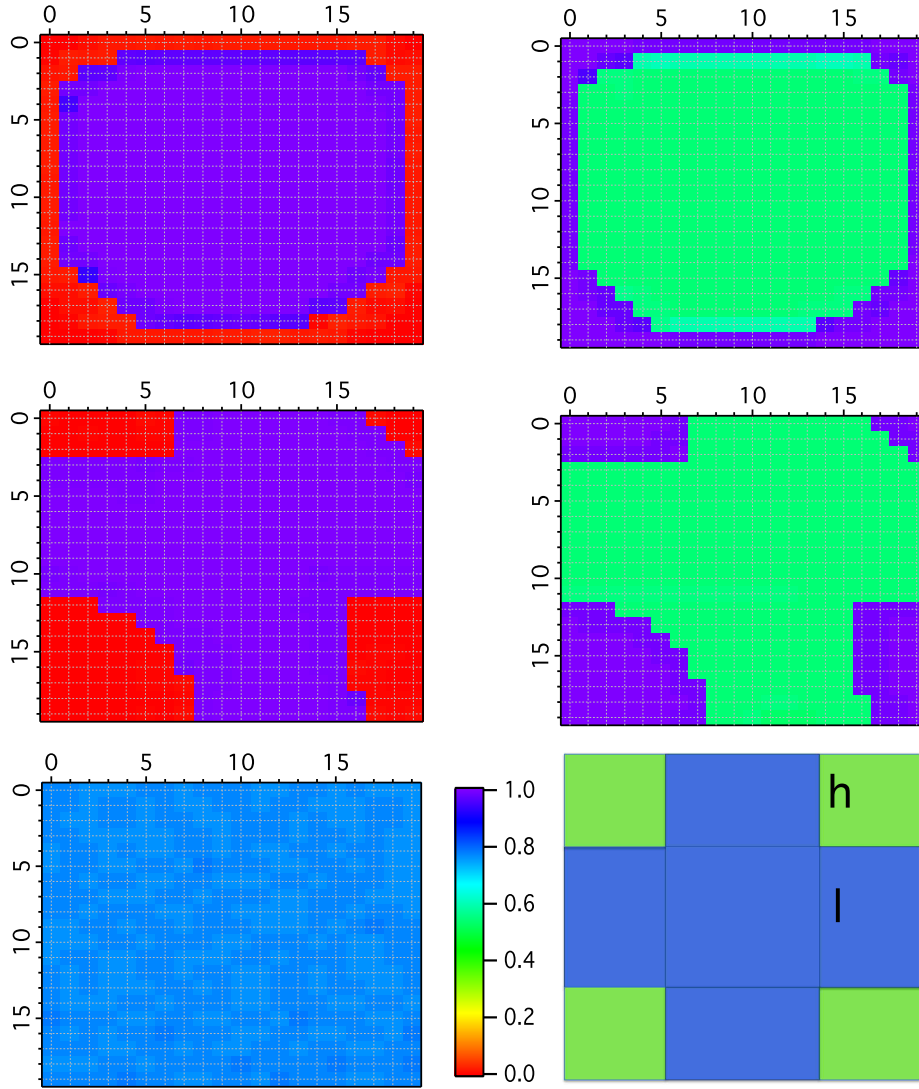
Figure 5.2: (Color online) Snapshot of the average local densities for $L = 20$ and $\rho = 1.44$. Top panel: Open boundary conditions. For a particles (left panel), sites close to the boundary (red) have $\langle n_i^a \rangle \sim 0$, while the occupation of the central (blue) region is $\langle n_i^a \rangle \sim 1$. For b particles (right panel) the density close to the boundary (blue region) is $\langle n_i^b \rangle \sim 1$, and at the center (green region), $\langle n_i^b \rangle \sim 0.60$. Middle panel: The same quantities shown in the top panel but with periodic boundary conditions. Bottom panel: At the left the homogeneous density distribution of both a and b particles for $\rho = 1.72$. At the right, a sketch of the density profile for a simulation with periodic boundary conditions.

The heavy species a shows Mott behavior with integer fillings, $\langle n_i^a \rangle \sim 0$ or 1, while the light species b shows Mott ($\langle n_i^b \rangle \sim 1$) and SF ($\langle n_i^b \rangle \sim 0.60$) phases. We can understand the tendency of the system to form such a mixed phase by extending the bosonic mean-field formalism [37, 154] to two species in the hardcore limit [141]. We use the Gutzwiller variational approach [155], in which the most general site factorized wave function can be written as

$$\Psi = \prod_i [sin\frac{\theta}{2}(sin\frac{\alpha}{2}a_i^\dagger + cos\frac{\alpha}{2}b_i^\dagger) + cos\frac{\theta}{2}(sin\frac{\beta}{2} + cos\frac{\beta}{2}a_i^\dagger b_i^\dagger)]|0\rangle. \tag{5.3}$$

The energy per site takes the form

$$\frac{E}{L^2} = -t_a sin^2\theta cos^2\left(\frac{\alpha - \beta}{2}\right) - t_b sin^2\theta sin^2\left(\frac{\alpha + \beta}{2}\right) + U^{ab}cos^2\frac{\theta}{2}cos^2\frac{\beta}{2}. \tag{5.4}$$

We solve these equations by minimizing the energy of the superfluid and phase separated states when $L = 20$, $t_a = 0.08$, $t_b = 1.0$ and $\rho = 1.44$, subject to the constraints

$$n_a = \frac{N_a}{L^2} = \sum_i \frac{\langle\Psi|n_i^a|\Psi\rangle}{L^2} \tag{5.5}$$

and

$$n_b = \frac{N_b}{L^2} = \sum_i \frac{\langle\Psi|n_i^b|\Psi\rangle}{L^2}. \tag{5.6}$$

For $\rho = 1.44$ we find that the phase separated state is lower in energy than a homogeneous superfluid phase. The total energy of a homogeneous superfluid with densities $\rho_a = \rho_b = 0.72$ is 804.33. The phase separated state is illustrated in the bottom right panel of Fig. 4.4 with a central cross with area $(2h+l)^2 - 4h^2$ and four corner squares of area h^2. If we assume that in the cross $\langle n_i^a \rangle = 1.0$ and $\langle n_i^b \rangle = 0.60$ for all i sites, then the mean-field energy is 754.19. The PS region is stabilized by the reduction of the potential energy, consequently there is a critical U_c^{ab} above which the phase separated state is stable. We estimate $U_c^{ab} \sim 4.8$.

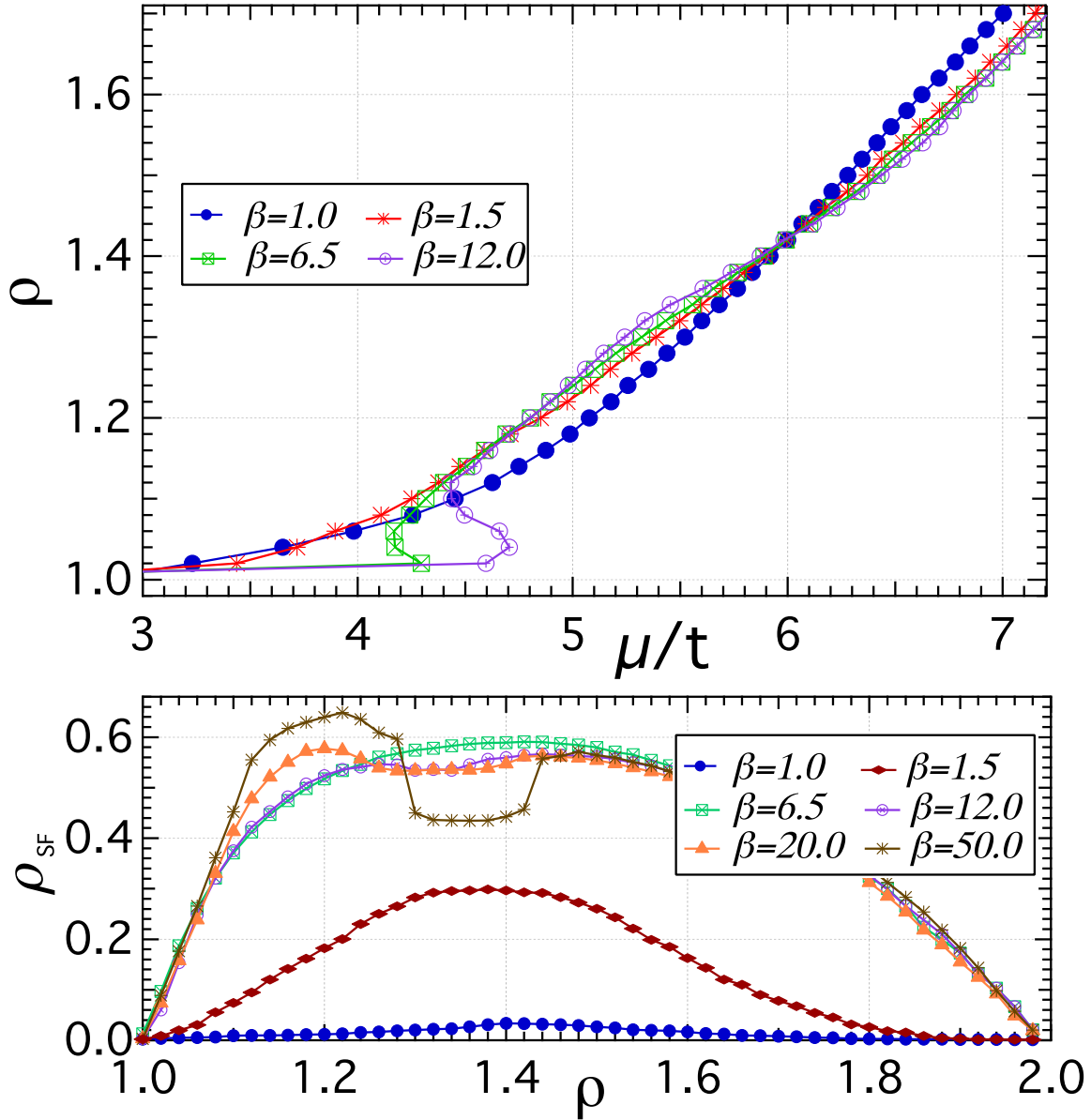Figure 5.3: (Color online) Top panel: Average density, ρ, versus chemical potential, μ, for different temperatures. Bottom panel: The superfluid density, ρ_{SF}, as a function of ρ for different temperatures. All data are for system size $L = 10$. Error bars are smaller than symbol sizes.

5.5   Finite Temperature Phase Diagram

Next we study the temperature dependence of ρ and ρ_{SF}. The top panel of Fig. 5.3 shows ρ versus μ for a system of size $L = 10$ and different inverse temperatures. Since there is a clear signature of phase separation for $\beta = 6.5$ but not for $\beta = 1.5$, we can conclude that the critical AF temperature occurs between these two temperatures. Similarly, from the ρ_{SF} vs. ρ curves for different temperatures (see bottom panel of Fig. 5.3), we can conclude that for this cluster size the phase separated region between ρ_3 and ρ_4 appears for temperatures between $\beta = 6.5$ and $\beta = 12$. We infer the phase diagram by appropriate scaling of our finite-size results.

Fig. 5.4 displays the temperature, T, vs. doping, $\delta = \dfrac{N_a + N_b}{2L^2} - \dfrac{1}{2}$, phase diagram. In the thermodynamic limit, the AF phase only exists at half filling $\delta_1 = 0$ and low temperatures. The top left panel shows the scaling of the AF to normal liquid (NL) continuous phase transition at $\delta_1 = 0$. This transition belongs to the two-dimensional Ising universality class for which the static staggered structure factor scales as

$$S(\pi, \pi) = L^{-(2\beta/\nu)} f((T - T_c^{AF})L^{1/\nu}), \tag{5.7}$$

where f is a universal scaling function, and β and ν are the critical exponents for the order parameter and the correlation length, respectively. The factor $2\beta/\nu = 1/4$ in two-dimensional systems. Therefore we can read the critical temperature at the point where the $S(\pi, \pi)L^{1/4}$ vs. T curves for different system sizes cross. For our parameters $T_c^{AF} = 0.116$, and $S(\pi, \pi)L^{1/4}$ vs. $(T - T_c^{AF})L$ curves collapse. The AF phase is represented by a red line ending on a blue diamond in Fig. 5.4. As we illustrate in previous figures, near half filling, we find a discontinuous transition from AF to SF phases and a phase separation region for doping $\delta_1 = 0.0 \leq \delta \leq \delta_2 = 0.06$ (dark blue region in Fig. 5.4). The boundary of the AF/SF phase separated region is found by a Maxwell's construction of the ρ vs. μ plots. The PS region inside the SF phase exists for $\delta_3 = 0.13 \leq \delta \leq \delta_4 = 0.28$. For a
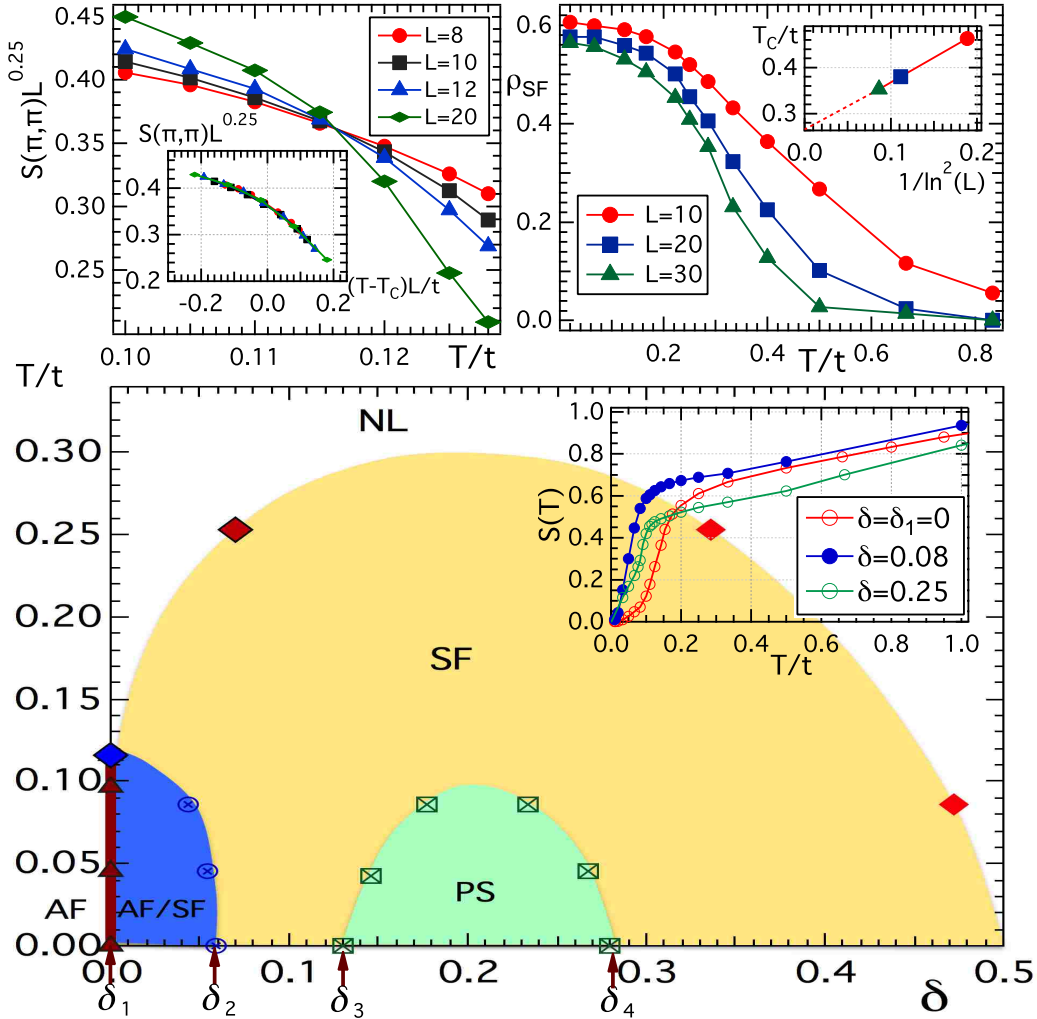
Figure 5.4: (Color online) Bottom panel: The temperature, T, versus doping, δ, phase diagram with equal population of each species. At half-filling, the system is antiferromagnetic (AF) below $T_c^{AF} \sim 0.116$ and normal liquid (NL) at larger temperatures. By increasing the doping a discontinuous transition from AF to superfluid (SF) phase occurs, and an AF/SF phase separated region develops between $\delta_1 = 0$ and $\delta_2 = 0.06$. Between $\delta_3 = 0.13$ and $\delta_4 = 0.28$ phase separation (PS) occurs with the heavy species becoming Mott while the light one displays regions with either Mott or superfluid behaviors. The inset shows entropy as a function of temperature for three dopings. Top left panel: Scaling behavior of the static staggered structure factor for the continuous transition from AF to NL at half filling, $\delta_1 = 0$ (corresponds to the filled blue diamond in the bottom panel). The inset shows the scaling near the critical temperature with Ising-like critical exponents. Top right panel: Superfluid density as a function of temperature for different system sizes at $\delta = 0.07$ (filled red diamond). The inset shows the finite size scaling to find the SF critical temperature in the thermodynamic limit for the continuous transition at $\delta = 0.07$. The data points are based on simulation results, the lines are guides to the eye.

given temperature we determine its boundaries by estimating the filling where ρ_{SF} starts decreasing (ρ_3 in Fig. 5.1) or stops increasing (ρ_4). For the rest of the dopings we encounter a SF phase at low temperatures and an NL at higher temperatures. The top right panel of Fig. 5.4 shows the superfluid density as a function of temperature for different system sizes. The order parameter, the superfluid density, has the universal jump of $\frac{\rho_{SF}}{T} = \frac{2}{\pi}$ at the critical point [93]. The transition from SF to NL is continuous and belongs to the Kosterlitz Thouless universality class. We find T_c in the thermodynamic limit by using the relation between the size dependent critical temperature $T_c(L)$ and the cluster size [156]:

$$T_c(L) - T_c(\infty) \propto \frac{1}{ln^2(L)}. \tag{5.8}$$

The inset on the right top panel displays this scaling. For $\delta = 0.07$ ($\rho = 1.14$) we find $T_c = 0.254$. Scaled transition points are shown as red diamonds in Fig. 5.4. The inset of the bottom panel shows the entropy for a $L = 10$ system calculated by following Ref. [157] for $\delta = 0$, $\delta = 0.08$ and $\delta = 0.25$. The entropy of the PS ferromagnetic phase is greater than the AF phase and similar to the SF phase, especially for low temperatures, indicating that it may be experimentally accessible. In addition, the entropy of this novel phase will mainly be carried by the light superfluid particles, enabling entropy squeezing [149].

5.6 Conclusion

In summary, with doping we find complex phases in the two-dimensional two-species hardcore bosonic Hubbard model for equal populations and unequal masses. We find a first order phase transition between the AF phase at half filling and a SF phase near half filling with a region of SF and AF coexistence. For a broad region of fillings and temperatures away from half filling, a SF phase is found. Most significantly, within the SF phase at finite doping we find a dome-shaped region containing an inhomogeneous ferromagnetic phase. Density profiles of this novel phase separated region show that the heavy species displays Mott insulating

behavior, while the light species is phase separated in Mott and superfluid regions. Despite the magnetic order, this novel phase has an entropy much greater than the AF phase, and similar to the SF phase. For a large system size, the entropy of the heavy species in this phase is essentially zero. This phenomenon can be considered as squeezing out the entropy from the heavy species into the light species, while both species are bosonic, in contrast with the recent proposal for cooling the boson-fermion mixture [149]. Farther from half filling, both species display a homogeneous superfluid phase.

This complex phase diagram reminds us of the phase diagram of cuprates. In particular, our phase diagram displays a region that is similar to the so-called "superconducting dome" away from half-filling. Further, we believe our work will encourage experimental studies of this model on cold atoms traps. Indeed the experimental realization of the half-filling AF phase is difficult due to the low entropy associated with this phase, while the complex ferromagnetic phase that we identify away from half-filling can be expected to have a high entropy and, then, be easier to obtain. To further explore this complex phase diagram we are planning to extend our simulations to polarized systems with different species population.

Chapter 6
Conclusion

Several competing tendencies in strongly correlated materials lead to very rich phase diagrams, containing a variety of phases with spin, charge, and orbital degrees of freedom, such as superconducting states, metals and insulators, multiferroics, and other states. These phases are interesting by themselves. Small changes in the parameters such as the composition, temperature, pressure, and external fields can induce a transition from one phase to another. This may cause interesting effects such as magnetoresistance and high-temperature superconductivity as shown in strongly correlated electronic materials. Understanding such interesting phenomena and exotic phases are of major interests in the field of condensed matter physics.

The thesis has been focused on the studies of equilibrium interacting problems of cold bosons loaded in optical lattices by using analytical and computational techniques. Although there is a considerable amount of work done to study Bose Hubbard model and its variants, many important issues still remain to be understood. We have used the quantum Monte Carlo (QMC) simulation, a large class of computer algorithms, and numerical calculations to solve quantum many-body systems. The QMC algorithm that we have used is the Stochastic Green Function (SGF) algorithm that is appropriate to deal with interacting bosons in equilibrium. The algorithm is exact since it does not have errors beyond statistical errors. The SGF can simulate any complicated sign-problem-free Hamiltonian. Taking advantage of the flexibility of the method, we have studied several interesting problems.

We have found a new confining method for ultra-cold atoms on optical lattices. This is called off-diagonal confinement (ODC) method which has distinct advantages over the existing diagonal confinement (DC) methods. Atoms are confined via a hoping integral that decreases as a function of the distance from the center of the lattice. The ODC method can also lead to lower temperatures than the DC method for a wide range of control parameters. Using exact diagonalization we determine this range of parameters for the hard-core case. Then, we extend our results to the soft-core case by using quantum Monte Carlo (QMC) simulations for both DC and ODC systems at fixed temperature. Further, we propose a new method to calculate entropy within QMC simulations by using the grand-canonical potential. By analyzing the corresponding entropies for both confinement systems we show that the ODC method can lead to lower temperatures than the existing DC method.

We propose that a superconducting ring with weak links might display a new phase which is gapless, compressible, and non-superfluid, with local Mott insulating behavior. The model contains an on-site repulsive interaction and two regions of different hopping. Important applications to atomtronics devices, ultra-cold-atom analogs of electronic devices, can be developed by introducing tunable weak links to a ring shape lattice. Our results have direct implications for atomtronic devices. For example, if the chemical potential, the weak link hopping, and the interaction are tuned so that only the link is a Mott insulator, then a gate above the link can be used to switch the conductivity of the link on and off. The non-linearity of the switching can be tuned by adjusting the link width and hopping. Complex circuits with highly non-linear behavior may be constructed by a series of such switches.

With the discovery of high-temperature superconductors, computational studies of two dimensional fermion systems have increased dramatically. However, exact QMC simulations of fermion systems are limited by the so-called sign problem. This motivates us to study boson systems, which can often be described by sign- problem-free Hamiltonian. Hence, we include doping dependence as a control parameter to study the two species two dimensional hard-core boson Hubbard model, which was recently studied at half filling. By changing

doping, the phase diagram shows an anti-ferromagnetically ordered Mott insulator phase, phase separated regions and a superfluid phase. We find coexistent anti-ferromagnetic (AF) and superfluid (SF) phases near half filling and a novel ferromagnetic phase-separated region inside the superfluid region away from half filling. In this novel ferromagnetic phase separated region, the heavy specie always has Mott behaviors while the other specie shows Mott and superfluid behaviors. Despite the magnetic order, this novel phase has an entropy much greater than the AF phase, and similar to the SF phase. For a large system size, the entropy of the heavy species in this phase is essentially zero. This phenomenon can be considered as squeezing out the entropy from the heavy species into the light species, while both species are bosonic, in contrast with the recent proposal for cooling the boson-fermion mixture. We also find a normal liquid phase at finite temperatures. In total five distinct phases are found. Most of the work is done in the context of theoretical effort, but they are really connected to the ongoing experimental research. Close interaction between theory and experiment has been crucial to progress in the field of condensed matter. The complexity of systems, their rich phase diagrams, self-organization, and nonlinear responses may suggest their potential use in device applications. Although there is a potential barriers aside technological applications, which will take some time to realize, the interesting properties of such materials clearly define an exciting field of fundamental scientific research that is full of surprises, and will surely continue to provide exciting and challenging phenomena in the near future.

References

[1] S. Yunoki, J. Hu, A. Malvezzi, A. Moreo, N. Furukawa and E. Dagotto, Phys. Rev. Lett., **80**, 845 (1998).

[2] A. Moreo, S. Yunoki and E. Dagotto, Science, 2034, **283** (1999).

[3] V. Kiryukhin, B. G. Kim, V. Podzorov and S. -W. Cheong, Phys. Rev. B., **63**, 024420 (2000).

[4] M. Uehara, S. Mori, C. H. Chen, S. -W. Cheong, Nature, **399**, 560 (1999).

[5] E. Dagotto, T. Hotta and A. Moreo, Phys. Rep., **344**, 1-153 (2001).

[6] P. Coleman and A. J. Schfield, Nature, **433**, 227 (2005). Q. Si and F. Steglich, Science, **329**, 1161 (2010).

[7] E. Dagotto, Science, **309**, 257 (2005).

[8] S. Nakatsuji, V. Dobrosavljević, D. Tanasković, M. Minakata, H. Fukazawa, and Y. Maeno, Phys. Rev. Lett., **93**, 146401 (2004).

[9] J. F. Mitchell, D. N, Argyriou, A. Berger, K.E. Gray, R. Osborn, and U. Welp , J. Phys. Chem. B., **105**, 10731 (2001).

[10] M. Vershinin, S. Misra1,S. Ono, Y. Abe, Y. Ando and A. Yazdani, Science, **303**, 1995 (2004).

[11] M. L. Foo, Y. Wang, S. Watauchi, H. W. Zandbergen, T. He, J. Cava, N. P. Ong, Phys. Rev., Lett. **92**, 247001 (2004).

[12] P. Limelette, P. Wzietek, S. Florens, A. Georges, T. A. Costi, C. Pasquier, D. Jérome, C. Méziére, and P. Batail, Phys. Rev. Lett., **91**, 016401 (2003).

[13] V. A. Sidorov, M. Nicklas, P. G. Pagliuso, J. L. Sarrao, Y. Bang, A. V. Balatsky, and J. D. Thompson, Phys. Rev. Lett., **89**, 157004 (2002).

[14] E. Loh et. al. Phys. Rev. B., **41**, 9301-9307 (1990).

[15] G. G. Batrouni and P. D. Forcrand, Phys. Rev. B., **48**, 589 (1993).

[16] M. Troyer and U. J. Wiese, Phys. Rev. Lett., **94**, 170201 (2005).

[17] D. Jaksch, C. Bruder, J. I. Cirac, C. W. Gardiner, and P. Zoller, Phys. Rev. Lett., **81**, 3108 (1998).

[18] M. Greiner, O. Mandel, T. Esslinger, T. W. Hänsch, and I. Bloch, Nature (London), **415**, 39-44 (2002).

[19] R. A. Pepino, J. Cooper, D. Z. Anderson and M. J. Holland, Phys. Rev. Lett., **103**, 140405 (2009).

[20] B. T. Seaman, M. Krämer, D. Z. Anderson and M. J. Holland, Phys. Rev. A., **75**, 023615 (2007).

[21] B. T. Seaman, M. Krämer, D. Z. Anderson and M. J. Holland, Phys. Rev. B., **72**, 054524 (2005).

[22] http://almaz.com/nobel/physics/.

[23] M. Lewenstein, A. Sanpera, V. Ahufinger, B. Damski, A. Sen(De) and U. Sen, Advances in Physics Vol., **56**, No. 2, 243-379 (2007).

[24] R. J. Glauber, Phys. Rev., **130**, 2529 (1963).

[25] M. O. Scully and W. E. Lamb, Phys. Rev., **159**, 2088 (1967).

[26] H. Haken, Z. Phys., **190**, 3278 (1966).

[27] R. J. Glauber, Phys. Rev., **131**, 2766 (1963).

[28] S. Chu, Rev. Mod. Phys., **70**, 685 (1998).

[29] C. N. Cohen-Tannoudji, Rev. Mod. Phys., **70**, 707 (1998).

[30] W. D. Phillips, Rev. Mod. Phys., **70**, 721 (1998).

[31] A. Einstein, Sitzungsbericht der Preussischein Akademie der Wissenschaften, p. **3** (1925).

[32] S. N. Bose, Z. Phys., **26**, 178 (1924).

[33] P. W. Anderson, Phys. Rev., **109** (1958).

[34] A. Niederberger, T. Schulte, J. Wehr, M. Lewenstein, L. Sanchez-Palencia, and K. Sacha, Phys. Rev. Lett., **100**, 030403 (2008).

[35] V. Ahufinger, L. Sanchez-Palencia, A. Kantian, A. Sanpera and Lewenstein, Phys. Rev. A., **72** (6), 063616 (2005).

[36] D. A. Abanin, P. A. Lee and L. S. Levitov, Phys. Rev. Lett., **98** (15), 156801 (2007).

[37] M. P. A. Fisher, P. B. Weichman, G. Grinstein, and D. S. Fisher, Phys. Rev. B., **40**, 546 (1989).

[38] F. Schreck, L. Khaykovich, K. L. Corwin, G. Ferrari, T. Bourdel, J. Cubizolles, and C. Salomon, Phys. Rev. Lett., **87**, 080403 (2001).

[39] A. Albus, F. Illuminati and J. Eisert, Phys. Rev. A., **68**, 023606 (2003).

[40] G. Modugno, G. Roati, F. Riboli, F. Ferlaino, R.J. Brecha, and M. Inguscio, Science, **297** (2002).

[41] C. Ospelkaus, S. Ospelkaus, K. Sengstock, and K. Bongs, Phys. Rev. Lett., **96**, 020401 (2006).

[42] G. Roati, M. Zaccanti, C. D′ Errico, J. Catani, M. Modugno, A. Simoni, M. Inguscio, and G. Modugno, Phys.Rev. Lett., **99**, 010403 (2007).

[43] G. Thalhammer, G. Barontini, L. De Sarlo, J. Catani, F. Minardi, and M. Inguscio,Phys. Rev. Lett., **100**, 210402 (2008).

[44] S. B. Papp, J. M. Pino,and C. E. Wieman: Phys. Rev. Lett., **101**, 040402 (2008).

[45] J. Catani, L. De. Sarlo, G. Barontini, F. Minardi, and M. Inguscio, Phys. Rev. A., **77**, 011603 (2008).

[46] M. Taglieber, et al., Phys. Rev. Lett., **100**, 010401 (2008).

[47] S. Taie, et al., Phys. Rev. Lett., **105**, 190401 (2010).

[48] E. Timmermans, P. Tommasini, M. Hussein, and A. Kerman, Phys. Rep., **315**, 199, (1999).

[49] T. Köhler, K. Góral, and P. S. Julienne, Reviews of Modern Physics, **78**, 1311, (2006).

[50] James, R. Anglin and W. Ketterle, Nature, **416**, (2002).

[51] Dirk van Delft, Freezing physics, Heike Kamerlingh Onnes and the quest for cold, edited by Edita KNAW, Amsterdam (2007).

[52] F. London, Nature, **141**, 643 (1938).

[53] I. Bloch, Nature Phys., **11** (2005).

[54] M. H. Anderson, J. R. Ensher, M. R. Matthews, C. E. Wieman, and E. A. Cornell, Science, **269**, 198 (1995).

[55] K. B. Davis, M. O. Mewes, M. R. van Druten, D. S. Durfee, D. M. Kurn, and W. Ketterle, Phys. Rev. Lett., **75**, 3969 (1995).

[56] C. C. Bradley, C. A. Sackett, J. J. Tollett, and R. G. Hulet, Phys. Rev. Lett. **75**, 1687 (1995) and Phys. Rev. Lett., **78**, 985 (1997).

[57] F. London, Phys. Rev., **54**, 947 (1938).

[58] L. Tisza, Nature, **141**, 913 (1938).

[59] L. Tisza, Phys. Rev., **72**, 838 (1947).

[60] B. P. Anderson and M. A. Kasevich, Science, **282**, 1686 (1998).

[61] L. D. Landau, J. Phys. USSR, **5:71** (1941).

[62] A.S. Parkins and D.F. Walls, Phys. Rep., **303** (1) (1998).

[63] F. Dalfovo, S. Giorgini, L. P. Pitaevskii, and S. Stringari, Rev. Mod. Phys., **71** (3): 463 (1999).

[64] A. J. Leggett, Rev. Mod. Phys., **73**, 307 (2001).

[65] C. J. Pethick and H. Smith, Cambridge University Press (2002).

[66] O. Penrose and L. Onsager, Physical Review, **104**, 576 (1956).

[67] Keith Burnett, Mark Edwards and Charles W. Clark, PHYSICS TODAY (1999).

[68] Gross, E.P., Il Nuovo Cimento **20** (3), 454-457 (1961).

[69] L. P. Pitaevsk, Soviet Physics JETP-USSR, **13**, No. 2 (1961).

[70] Tiesinga, E., Verhaar, B. J. and Stoof, H. T. C. , Phys. Rev. A **47**, 4114 (1993).

[71] Inouye, S. et al., Nature, **392**, 151 (1998).

[72] Courteille, P., Freeland, R. S., Heinzen, D. J., van Abeelen, F. A. and Verhaar, B. J., Phys. Rev. Lett., **81**, 69 (1998).

[73] S. Friebel, C. D′ Andrea, J. Walz, M. Weitz, and T. W. Hänsch, Phys. Rev. A., **57**, R20 (1998).

[74] Leonardo Fallani, Chiara Fort, Jessica Lye, and Massimo Inguscio, Optics Express, **13**, 4303 (2005).

[75] Leticia Tarruell, Daniel Greif, Thomas Uehlinger, Gregor Jotzu and Tilman Esslinger, Nature, **483**, 302 (2012).

[76] R. Saers, M. Rehn, T. Scheler, M. Zelán and A. Kastberg, the European Physical Journal Applied Physics, **42**, 269-273 (2008).

[77] I. Bloch, J. Dalibard, and W. Zwerger, Rev. Mod. Phys., **80**, 885 (2008).

[78] A. Ramanathan, K. C. Wright, S. R. Muniz, M. Zelan, W. T. Hill III, C. J. Lobb, K. Helmerson, W. D. Philips, and G. K. Campbell, Phys. Rev. Lett., **106**, 130401 (2011).

[79] Fisher, Matthew P. A.; Grinstein, G.; Fisher, Daniel S., Phys. Rev. B., **40**546 (1989).

[80] Eugene B. Kolomeisky, T. J. Newman, Joseph P. Straley, and Xiaoya Qi, Phys. Rev. Lett., **85**, 1146 (2000).

[81] V. J. Emery, S. A. Kivelson, and J. M. Tranquada, Proc. Natl. Acad. Sci., **96(16)**, 8814 (1999).

[82] Belén Paredes, Artur Widera, Valentin Murg, Olaf Mandel, Simon Fölling, Ignacio Cirac, Gora V. Shlyapnikov, Theodor W. Hänsch and Immanuel Bloch, Nature, **429**, 277 (2004).

[83] S. G. Söyler, B. Capogrosso-Sansone, N. V. Prokof'ev, and B. V. Svistunov, New J. Phys., **11**, 073036 (2009).

[84] Kim, E. and Chan, M. H. W., Nature, **427**, 225 (2004).

[85] G. G. Batrouni and R. T. Scalettar, Phys. Rev. B., **46**, 9051 (1992).

[86] W. Krauth and N. Trivedi, Europhys. Lett., **14**, 627 (1991).

[87] M. Cha, M. P. A. Fisher, S. M. Girvin, M. Wallin, and A. P. Young, Phys. Rev. B., **44**, 6883 (1991).

[88] J. K. Freericks and H. Monien, Phys. Rev. B., **53**, 2691 (1996).

[89] J. K. Freericks and H. Monien, Europhys. Lett., **26** 545 (1994).

[90] Till D. Kühner, Steven R. White, and H. Monien, Phys. Rev. B., **61**, 12474 (1999).

[91] V. A. Kashurnikov, A. V. Krasavin and B. V. Svistunov, JETP Lett., **64**, 92-96 (1996).

[92] V. F. Elesin, V. A. Kashurnikov and L. A. Openov, JETP Lett., **60**, 174-177 (1994).

[93] D. R. Nelson and J. M. Kosterlitz, Phys. Rev. Lett., **39**, 1201-1205 (1977).

[94] Goldenfeld, N., Lectures on Phase Transitions and the Renormalization Group, (Addison Wesley, Reading, MA) (1992).

[95] Kurt Binder, Rep. Prog. Phys., **50**, 783-859 (1987).

[96] Subir Sachdev, Cambridge University Press, NY, Quantum Phase Transitions, 2011, ISBN 0-521-58254-7(1999).

[97] C. P. Rubbo, *et al.*, Phys. Rev. A., **84**, 033638 (2011).

[98] R. Blankenbecler, D. J. Scalapino, and R. L. Sugar, Phys. Rev. D., **24**, 2278 (1981).

[99] A. W. Sandvik and J. Kurkijärvi, Phys. Rev. B., **43**, 5950 (1991).

[100] M. Rigol, and A. Muramatsu, Phys. Rev. A., **69**, 053612 (2004).

[101] M. Rigol, and A. Muramatsu, R. T. Scalettar, and G. G. Batrouni, Phys. Rev. Lett., **91**, 130403 (2003).

[102] V. G. Rousseau, Phys. Rev. E., **77**, 056705 (2008).

[103] V. G. Rousseau, Phys. Rev. E., **78**, 056707 (2008).

[104] V. G. Rousseau and D. Galanakis, arXiv:1209.0946 (2013).

[105] P. Jordan and E. Wigner, Z. Phys., **47**, 631 (1928).

[106] G. G. Batrouni, *et al.*, Phys. Rev. Lett., **65**, 1765 (1990).

[107] A. Nunnenkamp, *et al.*, Phys. Rev. A., **77**, 023622 (2008).

[108] G. G. Batrouni, V. Rousseau, T. T. Scalettar, M. Rigol, A. Muramatsu, P. J. H. Denteneer, and M. Troyer, Phys. Rev. Lett., **89**, 117203 (2002).

[109] C. Ryu, M. F. Andersen, P. Cladé, Vasant natarajan, K. helmerson and W. D. Philips, Phys. Rev. Lett., **99**, 260401 (2007).

[110] S. Fölling, A. Widera, T. Müller, F. Gerbier, and I. Bloch, Phys. Rev. Lett., **97**, 060403 (2006).

[111] V. G. Rousseau, G. G. Batrouni, D. E. Sheehy, J. Moreno, and M. Jarrell, Phys. Rev. Lett., **104**, 167201 (2010).

[112] V. G. Rousseau, K. Hettiarachchilage, D. E. Sheehy, J. Moreno, and M. Jarrell, Phys. Rev. A., **82**, 063631 (2010).

[113] Kalani Hettiarachchilage, Valéry G. Rousseau, Ka-Ming Tam, Mark Jarrell, Juana Moreno, Phys. Rev. A., **87**, 051607 (2013).

[114] S. G. Bhongale, L. Mathey, S.-W.Tsai, C. W. Clark, W. Charles and E. Zhao, Phys. Rev. Lett., **108**, 145301 (2012).

[115] A. Ruschhaupt and J. G. Muga, Phys. Rev. A., **70**, 061604 (R) (2004).

[116] A. Ruschhaupt and J. G. Muga, Phys. Rev. A., **73**, 013608 (2006).

[117] A. Ruschhaupt and J. G. Muga, J. Phys. B: At. Mol. Opt. Phys., **41**, 205503 (2008).

[118] E. L. Pollock and D. M. Ceperley, Phys. Rev. B., **36**, 8343 (1987).

[119] P. Jordan and E. Wigner, Z. Phys., **47**, 631 (1928).

[120] J. Friedel, Nuovo Cim. Suppl., **7**, 287 (1958).

[121] R. T. Scalettar, G. Batrouni, P. J. H. Denteneer, F. Hébert, A. Muramatsu, M. Rigol, V. Rousseau and M. Troyer, J. Low Temp. Phys., **140**, 313-332 (2005).

[122] J. Carrasquilla and F. Becca, arXiv:1005.4519 (2010).

[123] H. Ott, E. de Mirandes, F. Ferlaino, G. Roati, G. Modugno, and M. Inguscio, Phys. Rev. Lett., **92**, 160601 (2004).

[124] M. A. Cazalilla and A. F. Ho, Phys. Rev. Lett. **91**, 150403 (2003).

[125] F. Hébert, F. Haudin, L. Pollet, and G. G. Batrouni, Phys. Rev. A., **76**, 043619 (2007).

[126] A. Zujev, A. Baldwin, R. T. Scalettar, V. G. Rousseau, P. J. H. Denteneer, and M. Rigol, Phys. Rev. A., **78**, 033619 (2008).

[127] K. W. Mahmud, G. G. Batrouni, and R. T. Scalettar, Phys. Rev. A., **81**, 033609 (2010).

[128] M. Rigol, Phys. Rev. A., **72**, 063607 (2005).

[129] M. J. Wolak, V. G. Rousseau, C. Miniatura, B. Gremaud, R. T. Scalettar, and G. G. Batrouni, Phys. Rev. A., **82**, 013614 (2010).

[130] Waseem S. Bakr, Jonathon I. Gillen, Amy Peng, Simon Foelling, and Markus Greiner, Nature, **462**, 74-77 (2009).

[131] Kalani Hettiarachchilage, Valéry G. Rousseau, Ka-Ming Tam, Mark Jarrell, Juana Moreno, arXiv:1212.4478 (2013).

[132] S. Ejima, H. Fehske and F. Gebhard, Europhys Lett., **93**, 30002 (2011).

[133] J. Rech and K. A. Matveev, J. Phys.: Condens. Matter, **20**, 164211 (2008).

[134] D. L. Maslov and M. Stone Phys. Rev. B., **52** R5539 (1995).

[135] I. Safi and H. J. Schulz, Phys. Rev. B., **52** R17040 (1995).

[136] V V Ponomarenko, Phys. Rev. B., **52** R8666 (1995).

[137] A. R. Schmidt, M. H. Hamidian, P. Wahl, F. Meier, A. V. Balatsky, J. D. Garrett, T. J. Williams, G. M. Luke, and J. C. Davis, Nature, **465**, 7298 (2010).

[138] G. G. Batrouni and R. T. Scalettar, Phys. Rev. Lett., **84**, 1599 (2000).

[139] J. G. Bednorz, K. A. Mueller, Zeitschrift für Physik B., **64**, 189 (1986).

[140] Masatoshi Imada, Atsushi Fujimori, Yoshinori Tokura, Rev. Mod. Phys., **70**, 4 (1998); Elbio Dagotto, Rev. Mod. Phys., **66**, 763 (1994).

[141] E. Altman, W. Hofstetter, E. Demler, and M. D. Lukinn, New J. Phys., **5**, 113 (2003).

[142] B. Capogrosso-Sansone, S. G. Söyler, N. V. Prokof'ev, and B. V. Svistunov, Phys. Rev. A., **81**, 053622 (2010).

[143] Stephen Powell, Phys. Rev. A., **79**, 053614 (2009).

[144] A. Sotnikov, *et al.*, Phys. Rev. Lett., **109**, 065301 (2012).

[145] E. Khatami and M. Rigol, Phys. Rev. A., **86**, 023633 (2012).

[146] C. Monroe, D. M. Meekhof, B. E. King, S. R. Jefferts, W. M. Itano, D. J. Wineland, and P. Gould, Phys. Reve. Lett., **75**, 4011 (1995).

[147] M. Popp, *et al.*, Phys. Rev. A., **74**, 013622 (2006).

[148] X. Li, T. A. Corcovilos, Y. Wang, and D. S. Weiss, Phys. Rev. Lett., **108**, 103001 (2012).

[149] T.-L. Ho and Q. Zhou, Proc. Natl. Acad. Sci. USA, **106**, 6916 (2009).

[150] M. Boninsegni, Phys. Rev. Lett., **87**, 087201 (2001).

[151] S. Fölling, A. Widera, T. Müller, F. Gerbier, and I. Bloch, Phys. Rev. Lett., **97**, 060403 (2006).

[152] M. J. Wolak, V. G. Rousseau, C. Miniatura, B. Gremaud, R. T. Scalettar, and G. G. Batrouni, Phys. Rev. A., **82**, 013614 (2010).

[153] D. J. Thouless, Proc. Phys. Soc., London, **86**, 893 (1965).

[154] K. Sheshadri, H. R. Krishnamurthy, R. Pandit and T. V. Ramakrishnan, Europhys. Lett., **22**, 257 (1993).

[155] D. S. Rokhsar and B. G. Kotliar, Phys. Rev. B., **44**, 10328 (1991).

[156] M. Boninsegni, and N. Prokof'ev, Phys. Rev. Lett., **95**, 237204 (2005).

[157] F. Werner, *et al.*, Phys. Rev. Lett., **95**, 056401 (2005).

Appendix A: Permissions

The author has the right to use the article or a portion of the article in a thesis or dissertation without requesting permission from APS, provided the bibliographic citation and the APS copyright credit line are given on the appropriate pages.

From the website of the American Physical Society (APS).

1. V. G. Rousseau, K. Hettiarachchilage, M. Jarrell, J. Moreno, and D. E. Sheehy, *Using Off-diagonal Confinement as a Cooling Method*, Phys. Rev. A 82, 063631 (2010).

2. Kalani Hettiarachchilage, Valéry G. Rousseau, Ka-Ming Tam, Mark Jarrell, and Juana Moreno, *Phase diagram of the Bose-Hubbard model on a ring-shaped lattice with tunable weak links*, Phys. Rev. A 87, 051607 (2013).

3. Kalani Hettiarachchilage, Valéry G. Rousseau, Ka-Ming Tam, Mark Jarrell, and Juana Moreno, *Complex phases in the two species bosonic Hubbard Model*, arXiv:1212.4478, submitted for publication in Physical Review Letter (2013).

Appendix B: Basic Concepts of Phase Transitions

In recent years, the study of quantum phase transitions becomes a prominent field in science due to the complexity and emerging phenomena arising close to a quantum phase transition. In our daily lives, a phase transition is a very common phenomenon. As an example, when we boil water, we can see that the water is quiescent until it goes close to a temperature of $100^0 C$. Then water will boil by appearing bubbles and turn to vapor. When we cool water, it will turn to ice. The phase diagram of water in the plane of pressure (P) and temperature (T) is shown in Fig. B. 1.

The phase diagram has three separate phases: liquid, vapor and solid. They are separated from lines where two phases coexist: sublimation (solid-vapor), melting (solid-liquid), and vaporization (liquid-vapor), respectively. These three lines coincide at an unique point called a triple point, where all three phases coexist. There is a critical point or second order terminus at the end of the vaporization line.

The thermodynamic state of each phase should follow the most general Gibb's rules. This is given by $F = C - P + 2$ for a one component system when we sketch the phase diagram in the P-T plane, where F is the number of intensive variables, C is the number of components and P is the number of phases. At a location in the phase diagram where only one phase exists, $F = 1 - 1 + 2 = 2$ so that we have two intensive variables as P and T. The lines in the phase diagram where two phases coexist have $F = 1 - 2 + 2 = 1$, so there is only one independent variable, either P or T. At a location in the phase diagram where three phases coexist, $F = 1 - 3 + 2 = 0$, so there are no intensive variables. There is only one triple point in the phase diagram in Fig. B. 1, the point where the three phases coexist.

The critical point also can be seen in the P-V diagram of water shown in Fig. B. 2. This shows the process of water vaporization. Saturated states at various temperatures are
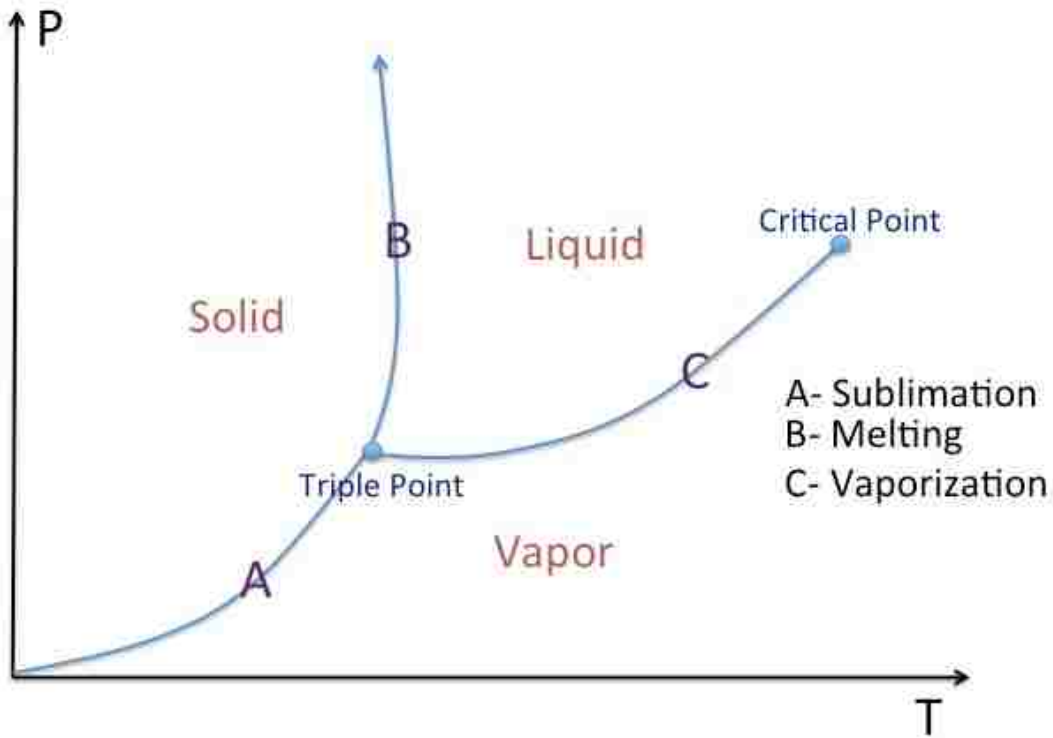
Figure B. 1: The phase diagram of water in the plane of pressure (P) and temperature (T). This shows the existing states of water as solid, liquid and vapor with transition lines as sublimation (solid to vapor), melting (solid to liquid) and vaporization (liquid to vapor), respectively.

labeled as saturated liquid line and saturated vapor line. At the critical temperature there is no coexistence of liquid and gas phases, but both phases become indistinguishable.

As seen in water, we can turn the state of a substance to different phases by changing its thermodynamic properties such as temperature and pressure. These phase transitions are thermal phase transitions and they occur due to thermal fluctuations at finite temperature. At zero temperature, those thermal fluctuations do not play any role, but quantum fluctuations driven by the Heisenberg uncertainty principle are still present. By changing a non-thermal control parameter of the system Hamiltonian, a quantum phase transition can occurs. Those are transitions driven by quantum fluctuations at absolute zero temperature. Transitions at zero temperature are important phenomena. They are associated with
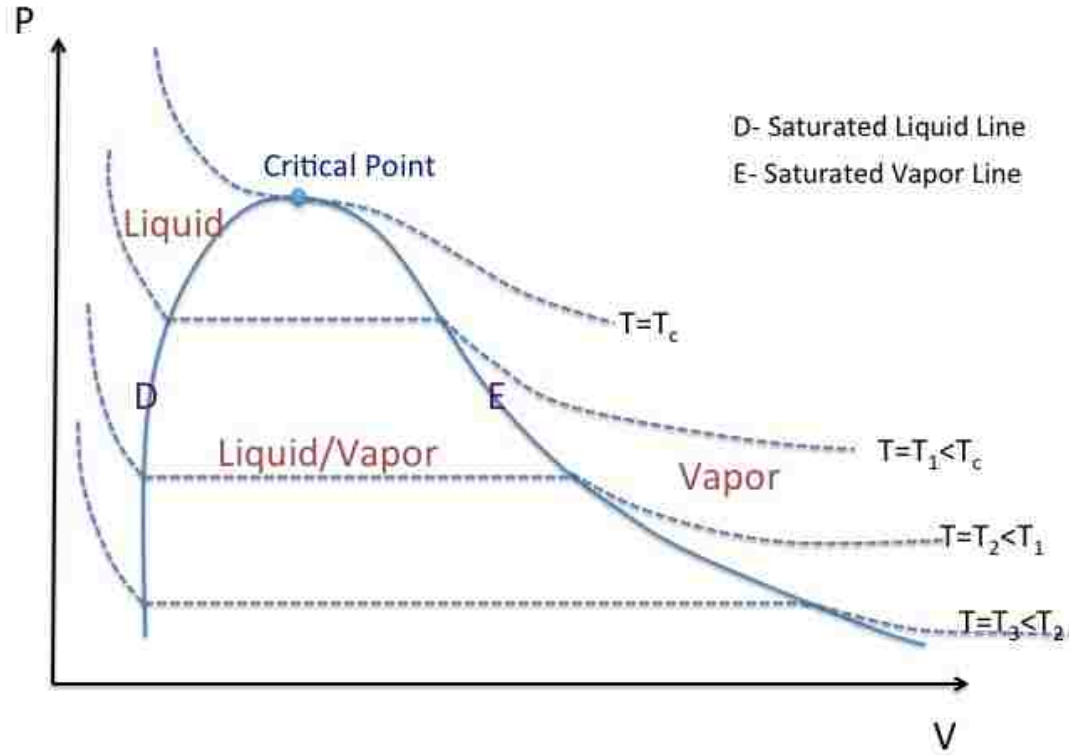
Figure B. 2: The phase diagram of water vaporization process in the plane of pressure (P) and volume (V). This shows coexistence of liquid and vapor phases as a function of different temperatures.

other important phenomena such as quantum criticality. A discussion on quantum phase transitions [94–96] follows.

According to Ehrenfest's discussion [94–96] it is possible to have first, second and higher order phase transitions depending on the non-analytic behavior of the free energy at the transition point. Although first order transitions are very common in nature, second order phase transitions and their critical behavior are essential to understand many recent experiments. The classification of phase transitions proposed by Ehrenfest is based on the behavior of the Gibb's free energy near the phase transformation. First-order phase transitions are characterized by the discontinuity of first derivatives of the Gibb's free energy. They are also called discontinuous transitions. In the same way, second-order phase transitions are characterized by the continuity of first derivatives of the Gibb's free energy, while second
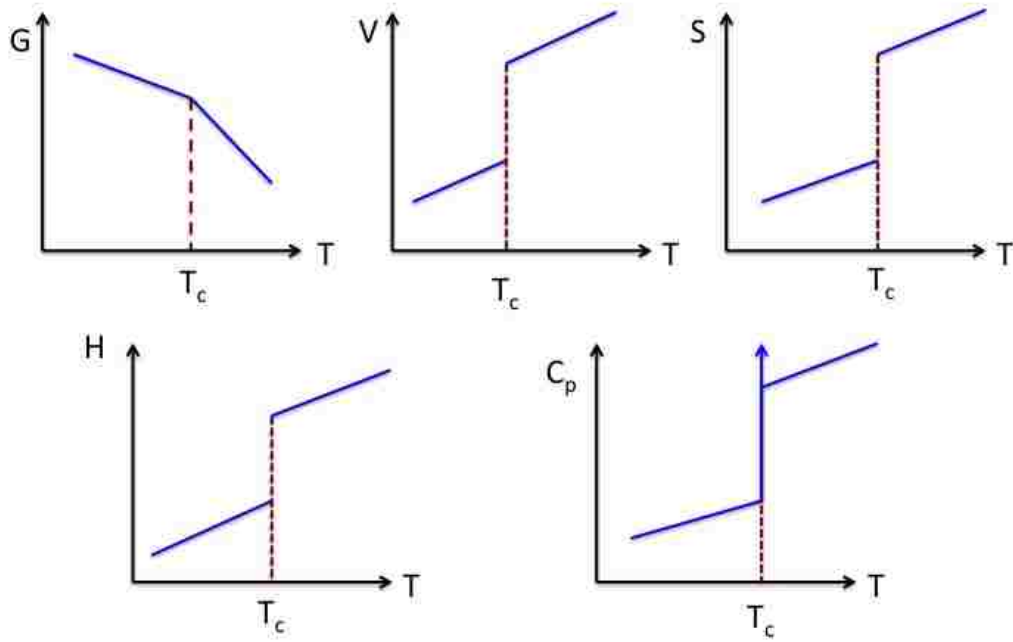
Figure B. 3: Non-analytic behavior of thermodynamic quantities in first order transition as a function of temperature. Behavior of Gibb's free energy (G), volume (V), entropy (S), enthalpy or heat (H) and heat capacity (C_p) are shown near critical temperature, T_c. Entropy, volume and enthalpy are discontinuous.

derivatives are discontinuous. They are called continuous transitions.

A well known example of first order phase transitions is the liquid-gas transition in water, while a ferromagnetic phase transitions, a superconducting transitions, and a superfluid to Mott insulator transitions are examples of the continuous phase transition. In second order phase transitions there is a divergence of thermodynamic quantities or response functions such as the susceptibility, correlation length and heat capacity. This is due to the power law decay of correlations near the transition point. Common thermodynamic properties around first order (discontinuous) and second order (continuous) phase transitions are shown in Fig. B. 3 and Fig. B. 4, respectively. Any correlation function near criticality can be written as $f(\tau) \approx \tau^k$, where $\tau = \dfrac{T - T_c}{T_c}$ and T is a temperature close to the critical temperature T_c such as $\tau \approx 0$. The k is the critical exponent. Above and below T_c there are two different phases. Continuous phase transitions can be identified by an order parameter.
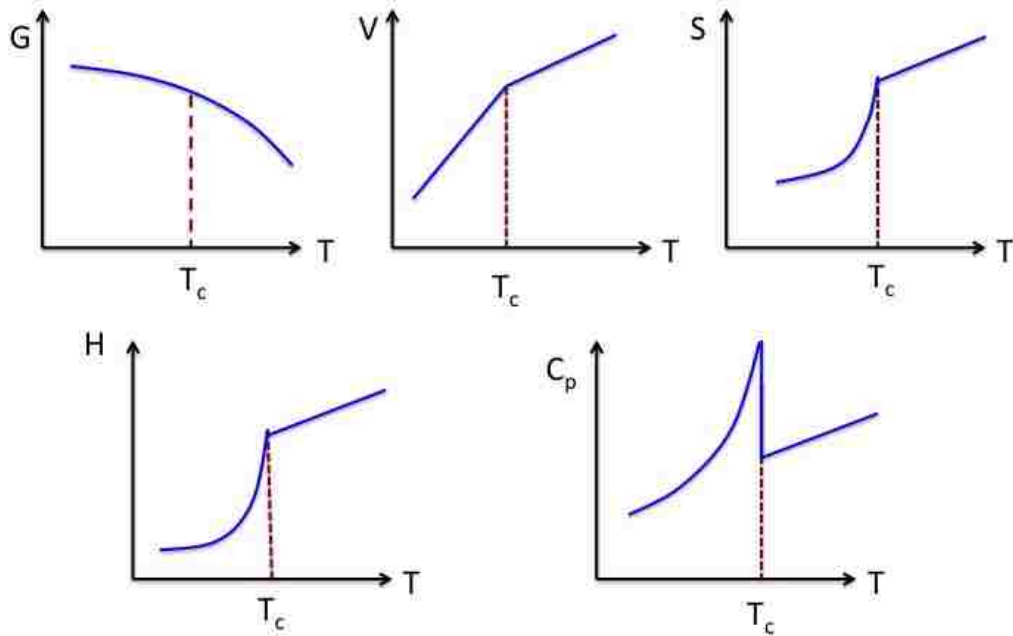
Figure B. 4: Non-analytic behavior of thermodynamic quantities in second order transition as a function of temperature. Behavior of Gibb's free energy (G), volume (V), entropy (S), enthalpy or heat (H) and heat capacity (C_p) are shown near critical temperature, T_c. All the response functions in second order transition are discontinuous.

The order parameter is the quantity that takes the value zero in the one phase (disordered phase or symmetric phase; $\tau > 0$) and non-zero in the other phase (ordered phase or non-symmetric phase; $\tau < 0$). Here, we should not forget that we have also several infinite order phase transitions such as Kosterlitz-Thouless transition in the XY-model, which also is a continuous transition, although there is no symmetry breaking.

Vita

Kalani Hettiarachchilage was born in SriLanka, a tiny island in the Indian Ocean. She was raised in a suburban area in the island with her brother and sister. She completed her high school education with high honors from the Kuliyapitiya Saranath Vidyalaya in SriLanka. Subsequently she was awarded a academic merit scholarship to pursue a bachelor degree of science at the very best university in the island, University of Peradeniya (UP), Sri Lanka in 1998. She obtained the highest honors BS degree in Physics with minor in Computer Science in 2002. Then she became an assistant lecturer in the department of physics at the UP, where she worked for two years. From 2004 to 2005, she was enrolled in a Mphil program on theoretical physics in the Postgraduate Institute of Science (PGIS) at the Institute of Fundamental Science (IFS), Sri Lanka. In 2005 she was awarded a scholarship to pursue a MS in condensed matter physics at the Norwegian university of science and technology (NTNU), Norway. After the successful completion of her MS degree, she joined the department of Physics and Astronomy at Louisiana State University (LSU) in August 2008 to work on Dr. Juana Moreno's and Dr. Mark Jarrell's group. She enjoys learning new thing everyday. When she has spare minute she likes to play volleyball, cook, play with her children and listen to music.